UNIVERSIDADE DE SÃO PAULO
Escola de Engenharia de São Carlos

Acoustoelastic response in rebars of reinforced concrete structures

Resposta acustoelástica em barras de estruturas de concreto armado

Thiago Delfino Lima Vasconcelos

Ph.D. Thesis – Programa de Pós-Graduação em Engenharia Civil (Engenharia de Estruturas) da Escola de Engenharia de São Carlos, Universidade de São Paulo

EESC · USP

THIAGO DELFINO LIMA VASCONCELOS

Acoustoelastic response in rebars of reinforced concrete structures

Thesis presented to the São Carlos School of Engineering of the University of São Paulo in partial fulfillment of the requirements for the degree of Doctor of Science in Civil Engineering.

Subject area: Structures

Advisor: Prof. Vladimir Guilherme Haach

CORRECTED VERSION

SÃO CARLOS

2025

Index card prepared by User Service at “Prof. Dr. Sergio Rodrigues Fontes Library” at EESC/USP

V331a

Vasconcelos, Thiago Delfino Lima
Acoustoelastic response in rebars of reinforced concrete structures / Thiago Delfino Lima Vasconcelos; advisor Vladimir Guilherme Haach. -- São Carlos, 2025.

Doctoral (Dissertation) - Graduate Program in Civil Engineering and Research area in Structure -- São Carlos School of Engineering, at University of São Paulo, 2025.

1. Ultrasound. 2. Acoustoelasticity. 3. Reinforced concrete. 4. Guided wave. I. Título.

Prepared by Eduardo Graziosi Silva- CRB-8/8907

FOLHA DE JULGAMENTO

Candidato: Engenheiro **THIAGO DELFINO LIMA VASCONCELOS**.

Título da tese: "Resposta acustoelástica em vergalhões de estruturas de concreto armado".

Data da defesa: 26/02/2025.

Comissão Julgadora	Resultado
Prof. Associado Vladimir Guilherme Haach (Orientador) (Escola de Engenharia de São Carlos/EESC-USP)	APROVADO
Prof. Associado Ricardo Carrazedo (Escola de Engenharia de São Carlos/EESC-USP)	APROVADO
Prof. Dr. Auteliano Antunes dos Santos Júnior (Universidade Estadual de Campinas/UNICAMP)	APROVADO
Profa. Dra. Gisleiva Cristina dos Santos Ferreira (Universidade Estadual de Campinas/UNICAMP)	APROVADO
Prof. Dr. Roberto Caldas de Andrade Pinto (Universidade Federal de Santa Catarina/UFSC)	APROVADO

Coordenador do Programa de Pós-Graduação em Engenharia Civil (Engenharia de Estruturas):
Prof Associado **Ricardo Carrazedo**

Presidente da Comissão de Pós-Graduação:
Prof. Titular **Carlos De Marqui Junior**

ACKNOWLEDGMENTS

First and foremost, I would like to express my deepest gratitude to my father (in memoriam), Laércio, my greatest and most influential supporter. Without him, I would not have had the strength to complete this doctorate. I will always carry him with me, no matter where I am.

I would also like to thank my wife, Bárbara, for her unwavering support and encouragement throughout my doctoral journey. Her help has been invaluable, and I am forever grateful for her love and partnership.

To my mother, Jeane, for her wise advice and for becoming my pillar of support during the challenging days. Your presence has been a constant source of strength.

To my son, Rafael, who was born alongside this thesis. You are the one who inspires me to be the best version of myself every single day.

To all my colleagues in the doctoral program, thank you for your camaraderie, encouragement, and collaboration throughout this journey.

To my advisor, Vladimir, for his brilliant guidance and mentorship throughout the entire process. Your expertise and wisdom have been essential to my success.

To the laboratory team for the support during all the experiments.

Finally, I would like to thank CAPES and IFAL for the partial funding of this research, which made this work possible.

This study was financed in part by the Coordenação de Aperfeiçoamento de Pessoal de Nível Superior - Brasil (CAPES).

ABSTRACT

VASCONCELOS, T. D. L. **Acoustoelastic response in rebars of reinforced concrete structures**. 2025. Thesis (Doctor Science in Civil Engineering (Structural Engineering)) - São Carlos School of Engineering, University of São Paulo, São Carlos, 2025.

The monitoring of reinforced concrete structures is essential to ensure that the normative lifetime is reached, which can be achieved through both destructive and non-destructive methods. Non-destructive testing is an effective solution, as it can be applied without causing damage to the structure while providing a wealth of data in a short period. Among the non-destructive methods, ultrasound testing stands out, providing information through the analysis of wave profiles and velocities. One of the most recent research lines with ultrasound is the study of acoustoelasticity in concrete structures, related to the correlation of wave velocity variation with stress state variation in the structure, where most of the research is focused on plain concrete structures. Due to the inherent heterogeneity of concrete, results often exhibit significant variability. In this context, the reinforcement can be considered homogeneous when compared to concrete and may provide more consistent data through ultrasound waves, potentially reducing result variability. There are no studies about acoustoelasticity with guided waves in rebars of reinforced concrete structures. Therefore, the present work aims to evaluate the acoustoelastic effect in reinforced concrete structures with the application of the transducers directly on the rebars. For this, ultrasonic indirect measurements were carried out during mechanical tests on reinforced concrete prisms, in which access to the reinforcement was ensured during casting. In addition to experiments in isolated rebars under tension, compression and bending tests in prisms were conducted. Different bar diameters, from 8 to 20 mm, were used, and a central frequency of 250 kHz was chosen. Finally, the wave interferometry method was applied to obtain the velocity variation. Thus, in isolated bars under tension, the relative velocity variation was negative, and there was a linear behavior in most of them. In compression, a tendency was observed in the prisms with 8 and 10 mm rebars, whose trendline had an initial non-linear part. In prisms under bending, a tendency was observed among the negative curves, whose trendline was entirely non-linear. Therefore, the waves captured on the rebar surface of reinforced concrete presented a good sensitivity to acoustoelastic effect.

Keywords: Ultrasound. Acoustoelasticity. Reinforced concrete. Guided wave.

RESUMO

VASCONCELOS, T. D. L. **Resposta acustoelástica em barras de estruturas de concreto armado**. 2025. Tese (Doutorado em Ciências - Engenharia Civil (Engenharia de Estruturas)) – Escola de Engenharia de São Carlos, Universidade de São Paulo, São Carlos, 2025.

O monitoramento de estruturas de concreto armado é essencial para garantir que a vida útil de projeto seja atingida, o que pode ser alcançado por meio de métodos destrutivos e não destrutivos. Os não destrutivos são uma solução eficaz, pois podem ser aplicados sem causar danos à estrutura, ao mesmo tempo em que fornecem uma grande quantidade de dados em um curto período. Dentre os métodos não destrutivos, o ultrassom se destaca, fornecendo informações por meio da análise dos perfis de onda e das velocidades. Uma das linhas de pesquisa mais recentes com ultrassom é o estudo da acoustoelasticidade em estruturas de concreto, relacionando a variação da velocidade de ondas com a variação da tensão na estrutura, porém a maior parte das pesquisas está focada em estruturas de concreto simples. Devido à heterogeneidade inerente ao concreto, os resultados frequentemente apresentam variabilidade significativa. Nesse contexto, a armadura pode ser considerada homogênea quando comparada ao concreto e pode fornecer dados mais consistentes por meio do ultrassom, potencialmente reduzindo a variabilidade dos resultados. Não existe estudo sobre acustoelasticidade com ondas guiadas em barras de estruturas de concreto armado. Portanto, o presente trabalho tem como objetivo avaliar o efeito acustoelástico em estruturas de concreto armado com a aplicação de transdutores diretamente nas barras. Para isso, são realizadas medições ultrassônicas indiretas durante testes mecânicos em prismas de concreto armado, nos quais o acesso à armadura é garantido durante a concretagem. Além de ensaios de tração em barras isoladas, são realizados ensaios de compressão e flexão em prismas. Foram utilizados diferentes diâmetros de barras, de 8 a 20 mm, e escolhida uma frequência central de 250 kHz. Finalmente, o método de interferometria de ondas é aplicado para obter a variação da velocidade. Portanto, em barras isoladas sob tração, a variação relativa da velocidade é negativa, e há um comportamento linear na maior parte delas. Na compressão, uma tendência é observada nos prismas com armaduras de 8 e 10 mm, cuja linha de tendência apresenta uma parte inicial não linear. Nos prismas sob flexão, uma tendência é observada entre as curvas negativas, cujas linha de tendência é toda não linear. Portanto, as ondas capturadas na superfície das barras de estruturas de concreto armado apresentaram boa sensibilidade ao efeito acustoelástico.

Palavras-chave: Ultrassom. Acustoelasticidade. Concreto armado. Ondas guiadas.

LIST OF FIGURES

LIST OF TABLES

TABLE OF CONTENTS

1 INTRODUCTION

To ensure the durability of structures, it is necessary to monitor the elements from the design phase to in-service use. As the quality in reinforced concrete structure production is provided by technological control, the quality of the finished structure is monitored through tests, which can be destructive or non-destructive. Destructive tests cause damage to the structure, which sometimes makes analysis unfeasible because, a priori, only its superficial conservation state is known. For this reason, non-destructive testing stands out, as it allows for the collection of much more data from the structure in a significantly shorter time and with minimal or no damage. Among the main non-destructive tests is ultrasound testing, which provides information about specimens by analyzing wave velocities and the respective wave profiles.

The use of ultrasound is well known in the evaluation of the mechanical characteristics of concrete, particularly for measuring the dynamic modulus of elasticity. However, a relatively underexplored research area is the study of acoustoelasticity, which examines the correlation between wave velocity and stress variation.

Most studies in this area focus on plain concrete structures, but given the heterogeneity of concrete, the reinforcement may provide more consistent data through ultrasound waves, potentially reducing result variability.

In reinforced concrete elements, in addition to bulk waves, guided waves are also produced along the rebars. However, there is no study on the assessment of the acoustoelastic effect using guided waves in reinforced concrete. In this context, the aim of this study is to evaluate the acoustoelastic effect on rebars of reinforced concrete elements.

1.1 OBJECTIVES

The general objective of the present work is to assess the acoustoelastic effect in rebars of reinforced concrete structures.

The specific objectives are:

1. To analyze the acoustoelastic effect under both tension and compression;
2. To compare the acoustoelastic effect in tension of isolated rebars and of those embedded in concrete;
3. To assess the feasibility of obtaining acoustoelastic response with transducer application directly on rebars;
4. To define reference acoustoelastic curves for isolated rebars under tension and for embedded rebars in tension and compression.

1.2 JUSTIFICATION

The knowledge of the stress level in a real structure is one of the concerns in health monitoring. Quantifying the stress in service may result in important information, which could be used to define a more precise structural maintenance and intervention. As the stress state is initially not known, this quantification must be done with minimal disturbance to the structure. In this context, ultrasound arises as a great non-destructive method, whose wave profiles and wave arrival times are used to evaluate changes in the stress state of the medium. This may enable the acquisition of stress data in any structure simply by applying the ultrasound test, whose results are obtained in a few seconds. In this context, due to the inherent heterogeneity of concrete, which might lead to high variability in responses, it is necessary to evaluate the use of reinforcement for assessing the structure's acoustoelastic effect. Therefore, the initial hypothesis is that the surrounding concrete would not influence the acoustoelastic effect in the rebar. Finally, in addition to bulk waves, guided waves are also generated in reinforced concrete elements, and there is no study on the evaluation of the acoustoelastic effect using guided waves in reinforced concrete.

1.3 THESIS OUTLINE

Chapter 1 consists of an introduction and the objectives and justification of the present study.

Chapter 2 presents the theory of the general wave propagation, the specific theory of bulk waves, including its acoustoelasticity application, and an explanation about the wave interferometry, which is the method used in the present study to compare signals.

Chapter 3 discusses the theory of guided waves, including the acoustoelasticity formulas of lamb waves. Moreover, the guided wave propagation in reinforced concrete is presented.

Chapter 4 details the systematic review applied in this study.

Chapter 5 describes the experimental program.

Chapter 6 presents a preliminary analysis of the types of waves on the wave profiles obtained.

Chapter 7 discusses the results of acoustoelasticity in isolated rebars and in prisms under compression and tension.

Chapter 8 presents the conclusion of the present study.

2 THEORETICAL BACKGROUND

This chapter discusses the main theories relevant to the present study, with a particular focus on bulk waves, the most common waves. When these waves reach thin specimens, compared to their wavelength, guided waves are generated, as is the case in rebars of reinforced concrete. Thus, the properties of bulk waves determine those of the resulting guided waves. As the theory of guided waves is more complex than that of bulk waves, it is discussed separately in Chapter 3.

2.1 THEORY OF WAVE PROPAGATION

Mechanical waves are disturbances in a medium that transmit kinetic energy through the movement of its material points. These waves can be classified by the frequency f, measured in Hertz (Hz), which represents the periodicity at which the waveform repeats. Therefore, waves with a frequency below 20 Hz are classified as infrasound; with frequencies between 20 Hz and 20 kHz, are called sound, which are the only ones audible to humans; and waves with frequency greater than 20 kHz are called ultrasound.

Figure 2.1 illustrates a simplified wave profile, where the amplitude A is the maximum displacement of the particles in one direction; the wavelength λ is the distance between two crests or between two troughs; and the period T (see Equation (2.1)), which corresponds to the time for traveling the distance λ. Based on these parameters, wave velocity V is obtained (see Equation (2.2)).

Figure 2.1 - Simplified wave profile

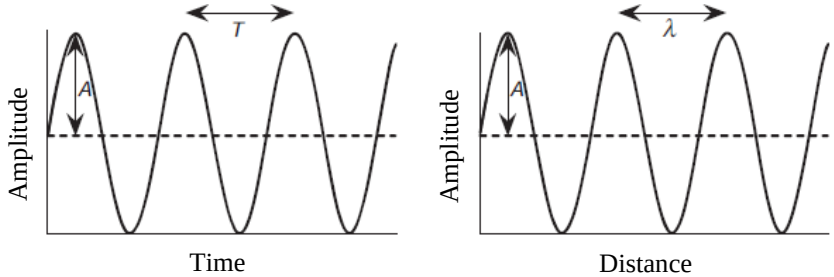

Source: adapted from Mehta and Monteiro (2008)

$$T = \frac{1}{f} \tag{2.1}$$

$$V = f\lambda \tag{2.2}$$

During propagation, the wave can reach the interface between two materials with different mechanical properties, what causes dispersion of part of the associated energy due to the difference between their acoustic impedances. Acoustic impedance is defined as the product of density and the corresponding wave velocity.

The dispersion intensity depends on the relationship between wavelength and the size of the element that causes the dispersion. As waves are commonly referenced by their frequency, and because frequency is inversely proportional to wavelength, higher frequencies result in greater dispersion and energy loss along the path. According to Malhotra and Carino (2004), waves with a frequency of 20 kHz can travel up to 10 m before losing all energy.

2.2 TYPES OF WAVES

Waves propagate through strain over time; therefore, they can be classified based on the kind of strain generated. In this regard, there are 2 main types of mechanical waves, also called bulk waves: compression waves, also known as longitudinal or P waves, and shear waves, also known as transverse or S waves.

Compression waves cause strain along the propagation direction, resulting in compressions and tensions along the path and volume changes. In contrast, shear waves cause distortions, deforming the medium in a direction perpendicular to the wave trajectory axis, called wave polarization direction, what only causes a change in medium's shape (see Figure 2.2).

Figure 2.2 - Types of bulk waves

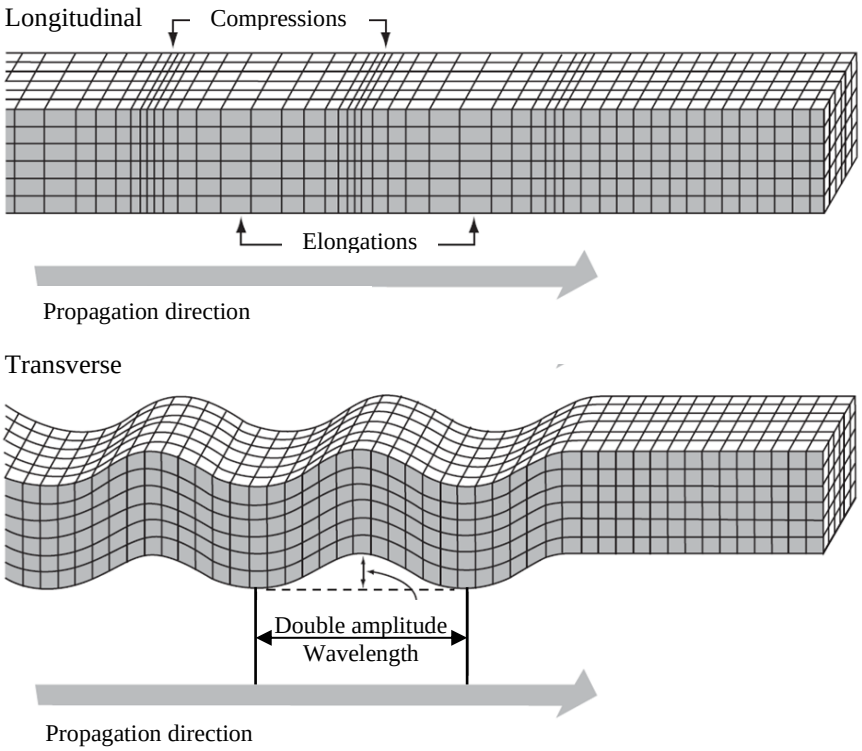

Source: adapted from Mehta and Monteiro (2008)

Longitudinal waves are faster and propagate in any medium while shear waves only propagate in solids. Longitudinal waves were initially studied by geophysicists, through observation of earthquake's effects. They were named primary waves (P waves) because they are the first to arrive at the surface, whereas shear waves are called secondary waves or S waves.

As an example, in concrete and steel, S waves have a velocity around 60% of that of P waves, according to Mehta and Monteiro (2008). Table 2.1 provides some reference velocities for P waves, V_P, and S waves, V_S. The reference velocities for concrete are not presented here, as they have great variability.

Table 2.1 - Wave velocities in different materials

Material	V_P **(m/s)**	V_S **(m/s)**
Air	330	-
Aluminum	6320	3130
Copper	4700	2260
Gold	3240	1200
Steel	5900	3230
Magnesium	5770	3050
Silver	3600	1590
Water	3600	-

Source: adapted from Krautkramer and Krautkramer (1990)

When bulk waves reach an interface, other types of waves may form, such as Rayleigh waves. These occur when bulk waves interact with a surface, and the specimen can be considered a semi-infinite medium. In this case, the particles exhibit an elliptical motion, with maximum amplitude at the surface and decreasing amplitude with depth (see Figure 2.3).

Figure 2.3 - Depiction of Rayleigh wave motion

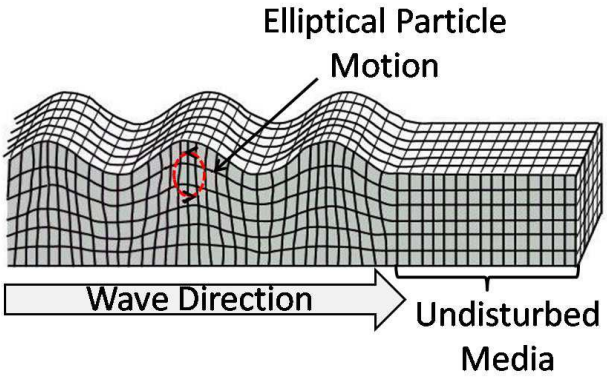

Source: Jones (2010)

On the other hand, when bulk waves reach a finite medium and their wavelength is comparable to or larger than the medium's thickness, a type of wave called guided wave forms. The energy keeps trapped between the boundaries of the specimen, whose entire body moves harmonically with the guided wave propagation (see Figure 2.4). For plate-like specimens, the wave is specifically called Lamb wave.

Figure 2.4 - Depiction of guided wave motion

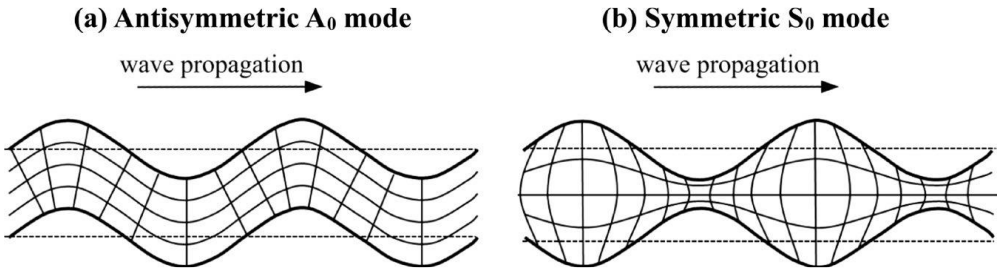

Source: Philibert *et al.* (2022)

This phenomenon takes place in rebars of reinforced concrete structures, the focus of the present work. Therefore, the wave profiles captured in the prisms of this study have contribution of bulk waves, guided waves and their respective reflections. As guided waves have a more complex theory and will be handled in Chapter 3, the following theory is related to bulk waves, whose characteristics define the other waves.

2.3 BULK WAVE VELOCITY

The governing formulations for wave velocity in a medium are presented in this section. It is considered a homogeneous and isotropic medium without stress.

As it is a dynamic problem, it is governed by the equations of motion continuity, shown in Equations (2.3), (2.4) and (2.5).

$$\frac{\partial \sigma_{xx}}{\partial x} + \frac{\partial \sigma_{yx}}{\partial y} + \frac{\partial \sigma_{zx}}{\partial z} + f_x = \rho \ddot{u} \tag{2.3}$$

$$\frac{\partial \sigma_{xy}}{\partial x} + \frac{\partial \sigma_{yy}}{\partial y} + \frac{\partial \sigma_{zy}}{\partial z} + f_y = \rho \ddot{v} \tag{2.4}$$

$$\frac{\partial \sigma_{xz}}{\partial x} + \frac{\partial \sigma_{yz}}{\partial y} + \frac{\partial \sigma_{zz}}{\partial z} + f_z = \rho \ddot{w} \tag{2.5}$$

where σ_{xx}, σ_{yy} and σ_{zz} are the normal stress components in the planes yz, xz and xy, respectively; σ_{yx}, σ_{zx} and σ_{zy} are the shear stress components in the planes xz in direction

of x axis, yx in direction of x axis and yx in direction of y, respectively; f_x is the external force in direction of x axis; ρ is the specific density of the medium; and u, v and w are the displacements components in the directions of x, y and z, respectively.

To simplify the deduction, the above equations can be simplified in index notation by Equation (2.6).

$$\sigma_{ij,i} + f_i = \rho \ddot{u}_i \tag{2.6}$$

From the Theory of Elasticity, the stress tensor for an isotropic medium is given by Equation (2.7).

$$\sigma_{ij} = 2\mu\varepsilon_{ij} + \lambda\varepsilon_{kk}\delta_{ij}. \tag{2.7}$$

δ_{ij} is the delta of Kronecker, ε_{ij} is the tensor of engineering strain, while μ, shear modulus, and λ are the Lamé constants, given by Equations (2.8), (2.9) and (2.10), respectively.

$$\varepsilon_{ij} = \frac{1}{2}\left(\frac{\partial u_i}{\partial x_j} + \frac{\partial u_j}{\partial x_i}\right) \tag{2.8}$$

$$\lambda = \frac{\nu E}{(1+\nu)(1-2\nu)} \tag{2.9}$$

$$\mu = \frac{E}{2(1+\nu)} \tag{2.10}$$

where E is the longitudinal modulus of elasticity and ν is the Poisson's ratio.

Substituting Equation (2.8) into Equation (2.7), Equation (2.11) is obtained.

$$\sigma_{ij} = \mu\left(\frac{\partial u_i}{\partial x_j} + \frac{\partial u_j}{\partial x_i}\right) + \lambda\frac{\partial u_k}{\partial x_k}\delta_{ij}. \tag{2.11}$$

Replacing Equation (2.11) in the motion equation, Equation (2.6), and considering that there are no external forces on the element, $f_i = 0$, it results in Equation (2.12).

$$\mu\left(\frac{\partial^2 u_i}{\partial x_j \partial x_i} + \frac{\partial^2 u_j}{\partial x_i \partial x_i}\right) + \lambda \frac{\partial^2 u_k}{\partial x_k \partial x_i}\delta_{ij} = \rho \frac{\partial^2 u_i}{\partial t^2} \tag{2.12}$$

As $\frac{\partial^2 u_i}{\partial x_j \partial x_i} = \frac{\partial^2 u_k}{\partial x_k \partial x_i}$, Equation (2.12) turns into Equation (2.13).

$$\mu\left(\frac{\partial^2 u_j}{\partial x_i \partial x_i}\right) + (\lambda + \mu)\frac{\partial^2 u_k}{\partial x_k \partial x_i}\delta_{ij} = \rho \frac{\partial^2 u_i}{\partial t^2} \tag{2.13}$$

For the case of transverse waves, as there is no volume variation, $\frac{\partial u_k}{\partial x_k} = 0$. Applying this in Equation (2.13), it results in $(\lambda + \mu)\frac{\partial^2 u_k}{\partial x_k \partial x_i}\delta_{ij} = 0$, and finally in Equation (2.14).

$$\mu\left(\frac{\partial^2 u_j}{\partial x_i \partial x_i}\right) = \rho \frac{\partial^2 u_i}{\partial t^2} \tag{2.14}$$

If it is considered x axis as the propagation direction, $u_2 = u_3 = 0$. Thus, Equation (2.14) becomes Equation (2.15), which represents the governing equation of transverse wave propagation.

$$\frac{\mu}{\rho}\left(\frac{\partial^2 u(x,t)}{\partial x^2}\right) = \frac{\partial^2 u(x,t)}{\partial t^2} \tag{2.15}$$

For the case of longitudinal waves, the deduction also starts from Equation (2.13). As there is no rotation in the medium of propagation, the Equation (2.16) is considered.

$$\frac{\partial u_i}{\partial x_j} = \frac{\partial u_j}{\partial x_i} \tag{2.16}$$

Deriving the above equation by the first term again, it results in Equation (2.17).

$$\frac{\partial^2 u_i}{\partial x_j^2} = \frac{\partial^2 u_j}{\partial x_j \partial x_i} \tag{2.17}$$

Regarding $\frac{\partial^2 u_j}{\partial x_i \partial x_i} = \frac{\partial^2 u_i}{\partial x_j^2}$ in Equation (2.13) and using the equation above, the Equation (2.18) is achieved.

$$\mu\left(\frac{\partial^2 u_i}{\partial x_j^2}\right) + (\lambda + \mu)\frac{\partial^2 u_i}{\partial x_j^2}\delta_{ij} = \rho\frac{\partial^2 u_i}{\partial t^2} \tag{2.18}$$

In this case, always $\delta_{ij} = 1$. Arranging Equation (2.18), Equation (2.19) is obtained.

$$(\lambda + 2\mu)\frac{\partial^2 u_i}{\partial x_j^2} = \rho\frac{\partial^2 u_i}{\partial t^2} \tag{2.19}$$

If it is considered x axis as the propagation direction, $u_2 = u_3 = 0$. Thus, Equation (2.20) is obtained, which governs the longitudinal wave propagation.

$$\frac{(\lambda + 2\mu)}{\rho}\left(\frac{\partial^2 u(x,t)}{\partial x^2}\right) = \frac{\partial^2 u(x,t)}{\partial t^2} \tag{2.20}$$

Any function $f(x \pm ct)$ is a solution to the wave equations, where c represents the wave velocity. Deriving f twice in terms of x, it is possible to obtain the Equation (2.21).

$$\frac{\partial^2 f(x \pm ct)}{\partial x^2} = \frac{\partial}{\partial x}\left(\frac{\partial f(u)}{\partial u}\frac{\partial u}{\partial x}\right) \tag{2.21}$$

As $\frac{\partial u}{\partial x} = 1$, it is achieved the Equation (2.22).

$$\frac{\partial^2 f(x \pm ct)}{\partial x^2} = \frac{\partial}{\partial x}\left(\frac{\partial f(u)}{\partial u}\right) = \frac{\partial^2 f(u)}{\partial u^2} \tag{2.22}$$

Analogously, it is obtained $\frac{\partial^2 f(x\pm ct)}{\partial t^2}$, shown in the Equation (2.23).

$$\frac{\partial^2 f(x \pm ct)}{\partial t^2} = \frac{\partial}{\partial t}\left(\frac{\partial f(u)}{\partial u}\frac{\partial u}{\partial t}\right) = \frac{\partial}{\partial t}\left(\frac{\partial f(u)}{\partial u}c\right) \tag{2.23}$$

As the wave propagates with constant velocity over time, the Equation (2.24) is obtained.

$$\frac{\partial}{\partial t}\left(\frac{\partial f(u)}{\partial u}c\right) = c\left(\frac{\partial^2 f(u)}{\partial u^2}\frac{\partial u}{\partial t}\right) = c\left(\frac{\partial^2 f(u)}{\partial u^2}c\right) = c^2\frac{\partial^2 f(u)}{\partial u^2} \tag{2.24}$$

Thus, the Equations (2.25) and (2.26) can be utilized.

$$\frac{\partial^2 f(x \pm ct)}{\partial x^2} = \frac{\partial^2 f(u)}{\partial u^2} = \frac{\partial^2 u(x,t)}{\partial x^2} \tag{2.25}$$

$$\frac{\partial^2 f(x \pm ct)}{\partial t^2} = c^2\frac{\partial^2 f(u)}{\partial u^2} = \frac{\partial^2 u(x,t)}{\partial t^2} \tag{2.26}$$

By Equation (2.25), $\frac{\partial^2 f(u)}{\partial u^2} = \frac{\partial^2 u(x,t)}{\partial x^2}$. Substituting this into Equation (2.26), it results in the Equation (2.27).

$$c^2\frac{\partial^2 u(x,t)}{\partial x^2} = \frac{\partial^2 u(x,t)}{\partial t^2} \tag{2.27}$$

Therefore, the transverse and longitudinal wave propagation velocities are calculated by the Equations (2.28) and (2.29), respectively.

$$c_S = \sqrt{\frac{\mu}{\rho}} \tag{2.28}$$

$$c_P = \sqrt{\frac{(\lambda + 2\mu)}{\rho}} \tag{2.29}$$

2.4 ACOUSTOELASTICITY THEORY

The theory of acoustoelasticity was first proposed by Hughes and Kelly (1953), whose research demonstrated the possibility of correlating the ultrasonic wave propagation velocity with the stress level in an elastic and isotropic medium. To evaluate the effect of acoustoelasticity, the theory of linear dynamic elasticity proves to be insufficient, making it necessary to incorporate non-linear elements into the linear constitutive equation of the material, Equation (2.30), as follows:

- The Green strain η_{ij} (Equation (2.31)) is used instead of the engineering strain ε_{ij} (Equation (2.8)) in the strain specific energy of material (Equation (2.32)), in which the third order term is considered.

Therefore, the constitutive equation is calculated by Equation (2.33), where S_{ij} is the second tensor of Piola-Kirchoff.

$$\sigma_{ij} = C_{ijkl}\varepsilon_{kl} \tag{2.30}$$

$$\eta_{ij} = \frac{1}{2}\left(\frac{\partial u_i}{\partial x_j^0} + \frac{\partial u_j}{\partial x_i^0} + \frac{\partial u_k}{\partial x_i^0}\frac{\partial u_k}{\partial x_j^0}\right) \tag{2.31}$$

$$\Psi(\eta_{ij}) = \Psi_0 + C_{ij}\eta_{ij} + \frac{1}{2!}C_{ijkl}\eta_{ij}\eta_{kl} + \frac{1}{3!}C_{ijklmn}\eta_{ij}\eta_{kl}\eta_{mn} \tag{2.32}$$

$$S_{ij} = \frac{\partial \Psi}{\partial \eta_{ij}} = C_{ijkl}\eta_{kl} + C_{ijklmn}\eta_{kl}\eta_{mn} \tag{2.33}$$

where $i, j, k, l, m, n = 1,2,3$; C_{ijkl} are the components of the fourth-order stiffness tensor of material properties; C_{ijklmn} is the stiffness tensor whose components are the elastic

constants of Murnaghan (1951), l, m and n; and x_i^0 and x_j^0 are the coordinates in the initial configuration of the specimen.

For the development of the acoustoelastic theory, Hughes and Kelly (1953) considered a medium with an initial finite stress, within ultrasonic waves are induced. For that, Lagrange coordinates and Murnaghan (1951) theory for finite strain were used.

The stress state change makes the material particles to assume another configuration, with final coordinates denoted as x_i, obtained by Equation (2.34).

$$x_i = A_i x_i^0 + U_i(x^0) \tag{2.34}$$

Equation (2.34) represents a superposition of a general infinitesimal strain (U_i) and a homogeneous triaxial finite strain ($A_i x_i^0$). The term $A_i x_i^0$ is related to particle displacement due to the application of an initial finite stress, where A_i was determined by Taylor series expansion truncated in first order. Keeping this stress constant and applying the ultrasonic wave, the specimen is submitted to the additional displacement $U_i(x^0)$, which represents general functions of all x^0. Thus, the final displacement of a particle is given by Equation (2.35).

$$u_i = x_i - x_i^0 = (A_i x_i^0 + U_i) - x_i^0 = (A_i - 1)x_i^0 + U_i \tag{2.35}$$

where $U_i \ll (A_i - 1)$.

Using Equation (2.35) in Equation (2.31), Equation (2.36) is obtained.

$$\eta_{ij} = \frac{1}{2}\left(\frac{\partial u_i}{\partial x_j^0} + \frac{\partial u_j}{\partial x_i^0} + \frac{\partial u_k}{\partial x_i^0}\frac{\partial u_k}{\partial x_j^0}\right) = \alpha_i \delta_{ij} + A_i A_j \varepsilon_{ij} \tag{2.36}$$

where:

$$\alpha_i = \frac{1}{2}(A_i^2 - 1) \tag{2.37}$$

and

$$\varepsilon_{ij} = \frac{1}{2}\left(\frac{\partial U_i}{\partial x_j} + \frac{\partial U_j}{\partial x_i}\right) \tag{2.38}$$

In the terms where $\varepsilon_{ij} = 0$, the first and second power of α_i are considered, otherwise only the first power is retained. So, the Equation (2.36) can be rewritten as Equation (2.39).

$$\eta_{ij} = \alpha_i \delta_{ij} + (1 + \alpha_i + \alpha_j)\varepsilon_{ij} \tag{2.39}$$

As the present theory considers isotropic body, the strain energy depends only on the strain invariants, given by Equations (2.40) – (2.42).

$$I_1 = \eta_{ii} \tag{2.40}$$

$$I_2 = \frac{1}{2}(\eta_{ii}\eta_{jj} - \eta_{ij}\eta_{ji}) \tag{2.41}$$

$$I_3 = \frac{1}{6}\epsilon_{ijk}\epsilon_{lmn}\eta_{il}\eta_{jm}\eta_{kn} \tag{2.42}$$

where ϵ_{ijk} is the Levi-Civita symbol.

The strain energy can be written in terms of these invariants in Equation (2.43).

$$\Psi = \frac{1}{2}(\lambda + 2\mu)I_1^2 - 2\mu I_2 + \frac{1}{3}(l + 2m)I_1^3 - 2mI_1I_2 + nI_3 \tag{2.43}$$

If Equation (2.43) is differentiated with respect to η_{ij}, it results in Equation (2.44), which corresponds to the Piola Kirchoff tensor.

$$S_{ij} = \frac{\partial \Psi}{\partial \eta_{ij}} = A + (B + C)\frac{\partial U_k}{\partial x_l} \tag{2.44}$$

where:

$$A = \theta\delta_{ij}\left(\lambda + \theta(l-m) + 2m\alpha_j\right) + \delta_{ij}\left(2\mu\alpha_j + m\sum_k \alpha_k^2\right) + \frac{1}{2}n\sum_{kl}\epsilon_{ikl}\epsilon_{jkl}\,\alpha_k\alpha_l \tag{2.45}$$

$$B = \delta_{kl}\delta_{ij}\left(\lambda + 2\theta(l-m) + 2m\alpha_j\right) + 2\delta_{ij}\left(\lambda\sum_m \alpha_m\,\delta_{mk}\delta_{ml} + m\sum_m \alpha_m\,\delta_{mk}\delta_{ml}\right) \tag{2.46}$$

$$C = \frac{1}{2}n\sum_p\left(\epsilon_{jpk}\epsilon_{ipl} + \epsilon_{jpl}\epsilon_{ipk}\right)\alpha_p + \left(\delta_{kj}\delta_{li} + \delta_{ki}\delta_{lj}\right)\left(\mu\left(1 + \alpha_i + \alpha_j\right) + m\theta\right) \tag{2.47}$$

where:

$$\theta = \alpha_1 + \alpha_2 + \alpha_3 \tag{2.48}$$

In the strain energy, Equation (2.43), the terms with order from 4 was neglected. For the second Piola Kirchorff tensor, the terms that ε_{ij} has order over 1, the terms of ε_{ij} whose α_i presents order over 1 and the independent terms of ε_{ij} whose α_i has order over 2 were neglected.

From the second Piola Kirchorff tensor, the Cauchy tensor is calculated, as shown in Equation (2.49).

$$\sigma_{ij} = \frac{F_{ik}S_{kl}F_{lj}}{J} \tag{2.49}$$

where F is the gradient of the configuration change function; and J is the Jacobian of the change, given by $J = \rho_0/\rho = \det(F)$, where ρ_0 and ρ are the densities in the initial and final configuration, respectively, given by Equation (2.50).

$$\rho = \rho_0/(1 + 2I_1 + 4I_2 + 8I_3) \tag{2.50}$$

Substituting Equation (2.44) in Equation (2.49), it results in Equation (2.51).

$$\sigma_{ij} = \frac{\partial \Psi}{\partial \sigma_{ij}} = D + (E + F)\frac{\partial U_k}{\partial x_l} \tag{2.51}$$

where:

$$D = \theta\delta_{ij}\left(\lambda + \theta(l - m - \lambda) + 2\alpha_j(m + \lambda - \mu)\right) + \delta_{ij}\left(2\mu\alpha_j + 4\mu\alpha_j^2 + m\sum_k \alpha_k^2\right) + \frac{1}{2}n\sum_{kl}\epsilon_{ikl}\epsilon_{jkl}\,\alpha_k\alpha_l \tag{2.52}$$

$$E = \delta_{kl}\delta_{ij}\left(\lambda + 2\theta(l - m - \lambda) + 2\alpha_j(m + \lambda - \mu)\right) + 2\delta_{ij}\left(\lambda\sum_m \alpha_m\,\delta_{mk}\delta_{ml} + m\sum_m \alpha_m\,\delta_{mk}\delta_{ml}\right) \tag{2.53}$$

$$F = \frac{1}{2}n\sum_p \left(\epsilon_{jpk}\epsilon_{ipl} + \epsilon_{jpl}\epsilon_{ipk}\right)\alpha_p + \left(\delta_{kj}\delta_{li} + \delta_{ki}\delta_{lj}\right)\left(2\mu\left(\alpha_i + \alpha_j + \alpha_l\right) + \mu + \theta(m + \lambda - \mu)\right) \tag{2.54}$$

Equation (2.51) can be rewritten as Equation (2.55).

$$\sigma_{ij} = \sigma_{ij}^0 + C_{ijkl}\frac{\partial U_k}{\partial x_l} \tag{2.55}$$

where σ_{ij}^0 is the initial stress state, given by $\sigma_{ij}^0 = D$, and $C_{ijkl}\frac{\partial U_k}{\partial x_l}$ is the increment of stress due to wave propagation, given by $C_{ijkl} = E + F$. In the case of medium initially unstrained, $\alpha = 0$, $\sigma_{ij}^0 = 0$ and C_{ijkl} becomes function only of the second order constants, μ and λ.

The motion equation becomes Equation (2.56), where no external forces on the element are considered.

$$\frac{\partial \sigma_{ij}}{\partial x_j} = \rho \frac{\partial^2 U_i}{\partial t^2} \tag{2.56}$$

As U_i represents wave displacement and considering Equation (2.55), both terms of Equation (2.56) can be rewritten as Equations (2.57) and (2.58).

$$\frac{\partial \sigma_{ij}}{\partial x_j} = C_{ijkl} \frac{\partial^2 U_k}{\partial x_j \partial x_l} \tag{2.57}$$

$$\rho \frac{\partial^2 U_i}{\partial t^2} = \rho c^2 \tag{2.58}$$

where c is the wave velocity in the direction of wave propagation.

Substituting the Equations (2.57) and (2.58) in Equation (2.56), the motion equation becomes Equation (2.59).

$$C_{ijkl} \frac{\partial^2 U_k}{\partial x_j \partial x_l} - \rho c^2 \delta_{jk} = 0 \tag{2.59}$$

In other words:

$$\det\left(C_{ijkl} \frac{\partial^2 U_k}{\partial x_j \partial x_l} - \rho c^2 \delta_{jk} \right) = 0. \tag{2.60}$$

There are 3 solutions for Equation (2.60), one results in longitudinal bulk wave velocity and two result in transverse bulk wave velocities, which one polarized in one direction. The Equations (2.61) – (2.63) presents the generalized solutions for wave propagation in each one of the three main directions of a strained solid.

$$\rho_0 c_{ii}^2 = \lambda + 2\mu + (2l + \lambda)\theta + (4m + 4\lambda + 10\mu)\alpha_i \tag{2.61}$$

$$\rho_0 c_{ij}^2 = \mu + (m+\lambda)\theta + 4\mu\alpha_i + 2\mu\alpha_j - \frac{1}{2}n\alpha_k \tag{2.62}$$

$$\rho_0 c_{ik}^2 = \mu + (m+\lambda)\theta + 4\mu\alpha_i + 2\mu\alpha_k - \frac{1}{2}n\alpha_j \tag{2.63}$$

In the equations above, c_{ij} are the velocities of waves propagating in direction i and with polarization direction j, where polarization refers to the wave vibration direction, with i and j referring to the main tension directions. Therefore, when i = j, there is a longitudinal wave, otherwise, it is a shear wave. Moreover, Hughes and Kelly (1953) considered sufficient the evaluation of α_i through the linear theory, which results in $\alpha_i = \varepsilon_i$, where ε_i are the main strains; and $\theta = \varepsilon_1 + \varepsilon_2 + \varepsilon_3$.

If an unstrained medium is considered, Equations (2.61) – (2.63) become $\rho_0 c_{ii}^2 = \lambda + 2\mu = C_{11}$ and $\rho_0 c_{ij}^2 = \mu = C_{44}$, which represent wave propagation in an isotropic medium without stress. This case was detailed in Item 2.3.

Considering the axes of main strains and those of main stresses coincident and the linear Hooke law, strains are substituted by elastic stresses and modulus. Besides, regarding a uniaxial stress σ_{11} along axis 1 direction of a homogeneous and isotropic material, Equations (2.64) – (2.68) are obtained.

$$\rho_0 c_{11}^2 = \lambda + 2\mu - \frac{\sigma_{11}}{3\lambda + 2\mu}\left[2l + \lambda + \frac{\lambda+\mu}{\mu}(4m + 4\lambda + 10\mu)\right] \tag{2.64}$$

$$\rho_0 c_{12}^2 = \rho_0 c_{13}^2 = \mu - \frac{\sigma_{11}}{3\lambda + 2\mu}\left[m + \frac{\lambda n}{4\mu} + 4\lambda + 4\mu\right] \tag{2.65}$$

$$\rho_0 c_{22}^2 = \rho_0 c_{33}^2 = \lambda + 2\mu - \frac{\sigma_{11}}{3\lambda + 2\mu}\left[2l - \frac{2\lambda}{\mu}(m + 4\lambda + 2\mu)\right] \tag{2.66}$$

$$\rho_0 c_{21}^2 = \rho_0 c_{31}^2 = \mu - \frac{\sigma_{11}}{3\lambda + 2\mu}\left[m + \frac{\lambda n}{4\mu} + \lambda + 2\mu\right] \tag{2.67}$$

$$\rho_0 c_{23}^2 = \rho_0 c_{32}^2 = \mu - \frac{\sigma_{11}}{3\lambda + 2\mu}\left[m - \frac{\lambda + \mu}{2\mu}n - 2\lambda\right] \tag{2.68}$$

According to Lillamand *et al*. (2010) and Ortega *et al*. (2011), the relationship between velocity and stress can be considered linear, what allowed to obtain Equation (2.69).

$$\frac{c_{ij}^{\sigma} - c_{ij}^{0}}{c_{ij}^{0}} = \frac{\Delta c_{ij}}{c_{ij}^{0}} = A_{ij}\sigma_{11} \tag{2.69}$$

where c_{ij}^{σ} and c_{ij}^{0} are the velocities in the medium with and without stress, respectively, and A_{ij} is called acoustoelastic constant, which depends on the mechanical properties of the material and the type of wave that propagates.

2.5 WAVE INTERFEROMETRY

To evaluate the velocity shift between signals, one can use only the wavefront arrival time, as done by Kato *et al*. (1995). This time is simply obtained through the determination of wave arrival on its profile, which is often automatically provided by the ultrasound device. The times between two profiles are compared and the corresponding velocity shift is calculated. Despite the simplicity of this method, the velocity change with stress is very small, and the definition of the wave arrival time by the device is very sensitive, what hampers the use of this parameter for quantifying acoustoelastic effect. For this reason, it is not a usual method.

To obtain this time variation, the literature indicates the analysis of a time window on the wave profiles, within which it is possible to perceive a translation and/or elongation between signals. To quantify this, the wave interferometry technique is used.

This method is based on a cross-correlation between two ultrasound signals, unperturbed and perturbed. Within this method, there is the displacement technique, in which the disturbed signal is displaced on the time axis. Thus, similarity between it and

the undisturbed signal is given by the normalized cross-correlation value, CC, given by Equation (2.70).

$$CC(\Delta t) = \frac{\int_{t_c-T}^{t_c+T} u_{np}(t)u_p(t-\Delta t)dt}{\sqrt{\int_{t_c-T}^{t_c+T} u_{np}^2(t)dt \int_{t_c-T}^{t_c+T} u_p^2(t-\Delta t)dt}} \tag{2.70}$$

A window of the undisturbed signal u_{np} of size 2T and central time t_c is shifted on the time axis for each variation Δt, resulting in a value of $CC(\Delta t)$. The procedure is repeated until a maximum value of the function is reached, corresponding to $\Delta t_{CCmáx}$, which is the time difference between the two analyzed signals. In this way, through Equation (2.71), the relative velocity variation between signals is obtained.

$$\frac{\Delta V}{V_0} = -\frac{\Delta t_{CCmáx}}{t_c} \tag{2.71}$$

Within the cross-correlation method, there is also the elongation technique, wherein the undisturbed signal is stretched or compressed from $u_{np}(t)$ to $u_{np}\big(t(1+\tau)\big)$, using a factor τ which is the velocity variation itself between both signals. The stretching technique procedure is similar to the displacement technique's, whose cross-correlation function is given by Equation (2.72).

$$CC(\tau) = \frac{\int_{t_c-T}^{t_c+T} u_{np}\big(t(1+\tau)\big)u_p(t)dt}{\sqrt{\int_{t_c-T}^{t_c+T} u_{np}^2\big(t(1+\tau)\big)dt \int_{t_c-T}^{t_c+T} u_p^2(t)dt}} \tag{2.72}$$

The main issue about the use of cross-correlation is about which window to consider on the profile. The parameters that define this window are its size and location.

In this context, most researchers consider a window within the coda wave, such as Planès and Larose (2013) Grêt, Snieder and Scales (2006), Snieder *et al*. (2002) and Resende (2018). This choice results in the so-called technique of Coda Wave Interferometry (CWI).

According to Planès and Larose (2013), the term ‘Coda’ comes from geophysics, referring to the final part of a seismogram after an earthquake. The authors justify that this region can better reflect the variation in wave profile because the waves that arrive there have already undergone several reflections, being more sensitive to changes in the medium.

The CWI method is widely used for assessing the acoustoelastic effect, such in the works of Xie *et al*. (2016) and Jiang *et al*. (2021). In this last study, for the cross-correlation, the entire wave profile was used. The authors justified this choice by the difficulty in establishing the sizes and position of the time window analyzed.

Despite CWI having good sensitivity to stress variation, there is no consensus on the window that should be considered as reference. Different analysis windows generate different results, as well as considering the entire coda wave results in practically zero variation.

For this reason, Zhong, Zhu e Morcous (2021) proposed a method called Direct P Wave Interferometry (DPWI), whose analysis occurs in the direct P wave part of the signals. In this context, DPWI is a particular case of CWI, where the window considered begins at the longitudinal wave arrival and extends until shear wave arrival, which guarantees that the results are only related to longitudinal waves.

In the present study, before the assessment of acoustoelastic effect, different time windows are analyzed along wave profile. Some locations are considered as reference: those whose beginning coincides with the wavefront arrival and those in Coda wave. For the first case, an analysis of the fastest wave is done, among bulk and guided waves.

2.6 HIGHLIGHTS OF CHAPTER 2

An abstract of the chapter is listed here:

a) Two types of waves occur in reinforced concrete structures. The emitting transducer produces bulk waves. When these waves reach a finite medium and their wavelength is comparable to or larger than the medium's

thickness, guided waves are produced. This is what happens in rebars embedded in concrete;

b) In isotropic homogeneous medium without stress, bulk wave velocities are calculated by Equations (2.28) and (2.29). The first is related to longitudinal bulk waves, the second, to transverse bulk waves.
c) In isotropic homogeneous medium under stress, the acoustoelastic effect with bulk wave is quantified by Equations (2.64) – (2.68).
d) The relationship between stress and velocity variation can be considered linear, as shown in Equation (2.69).
e) To obtain the velocity shift between two signals, the wave interferometry technique is used, where portions of profile are compared. For this, some time windows are analyzed along wave profile, from the window beginning that coincides with wavefront arrival to a window on Coda wave. For the first case, an analysis is carried out to find which wave is the fastest, bulk or guided waves.

3 GUIDED WAVES IN REBARS

Bulk waves propagate inside the bulk of solids, away from the interfaces and boundaries, which are discontinuities that cause reflection, refraction and mode transformation. In contrast, guided waves require boundaries and interfaces to exist; they travel along the surface of a material, the interface between two materials and through a thin specimen, confined between the solid contours.

Among the guided waves, there are the surface and interface wave, which are generated by a specific angle of incidence of bulk waves for all frequencies (Sadler and Maev, 2007), whose value only depends on material. It makes these waves travel near the surface. Examples of interface waves include the shear horizontal zero order, also called dispersion free SH_0, and the subsurface longitudinal, also called creeping, skimming longitudinal and critically refracted longitudinal (Ortega et al, 2011). An example of a surface wave is the Rayleigh wave.

Rayleigh waves propagate through elliptical particle movements perpendicular to the element's surface. At the surface, the displacements intensity assumes the maximum value, whereas it decreases exponentially into the sample, considered as a half-space, and finally considered negligible around the wavelength. In finite-dimension elements, such as plates, Rayleigh waves remain confined between the boundaries and are known as Lamb waves.

Theoretically, Rayleigh waves propagate only in half-space and Lamb waves propagate in thin plates. However, because it is difficult to consider a true half-space in practice, Rayleigh waves can exist in finite-dimension solids (Viktorov, 1967). Thus, when the specimen thickness is approximately the wavelength, Rayleigh waves transform into Lamb waves (Ortega *et al*., 2011; Edwards, 2002).

Guided waves are widely used to analyze long elements with a single application, as they propagate over long distances through specimens that act as a guide. Because of that, these waves are mainly used to identify flaws, given their high sensitivity to defects. Due to these characteristics, guided waves are used to evaluate buried pipes (Matuszyk, 2017; Tua, Quek and Wang, 2005; Ng *et al.*, 2022; Duan *et al.*, 2018; Yang, Polak and Cascante, 2010), steel bars in reinforced concrete, concerning to corrosion state

(Mustapha *et al.*, 2014; Majhi *et al.* 2021; Lu *et al.*, 2013; Li *et al.*, 2021) and to debonding between concrete and bar (Aseem and Ng, 2021; Mahbaz, Cascante and Dusseault, 2021; Zima and Kędra, 2021; Na, Kundu and Ehsani, 2003; Garcia *et al.*, 2017; Li *et al.*, 2017; Ke *et al.*, 2019).

3.1 RAYLEIGH WAVE FORMULATION

The first theory about wave propagation in multilayered media was published by Rayleigh (1885), who considered a free surface of a half-space. At a certain distance from the transmitter, it is possible to consider the wave movement as a two-dimensional strain. Thus, the displacements u, parallel to the propagation direction x, and w, parallel to z axis and perpendicular to x, are calculated by Equations (3.1) and (3.2).

$$u = A(re^{-qz} - 2sqe^{-sz}) \cos k(x - ct) \tag{3.1}$$

$$w = Aq(re^{-qz} - 2e^{-sz}) \sin k(x - ct) \tag{3.2}$$

where A is the amplitude, $k = 2\pi/\lambda$ is the wavenumber, λ is the wavelength,

$$q = \sqrt{1 - \left(\frac{c}{c_L}\right)^2}, s = \sqrt{1 - \left(\frac{c}{c_T}\right)^2}, r = 2 - \left(\frac{c}{c_T}\right)^2. \tag{3.3}$$

Considering $\eta = c/c_T$ and $\zeta = c_T/c_L$, where c_L is the longitudinal bulk wave velocity and c_T is the transverse bulk wave velocity, it results in Equation (3.4), which is the characteristic equation of Rayleigh waves.

$$\eta^6 - 8\eta^4 + 8\eta^2(3 - 2\zeta^2) + 16(\zeta^2 - 1) = 0 \tag{3.4}$$

Considering

$$\zeta = \frac{c_T}{c_L} = \sqrt{\frac{1-2\nu}{2(1-\nu)}}, \tag{3.5}$$

there are three roots for η^2 in function of ν. As η, and consequently c, doesn't depend on the frequency, the Rayleigh wave isn't dispersive and its velocity, c_R, is the phase velocity c.

An approximated solution is presented by Viktorov (1967), as shown in Equation (3.6).

$$\eta = \frac{0.87 + 1.12\nu}{1+\nu} \tag{3.6}$$

Therefore, the Rayleigh wave velocity is given by Equation (3.7).

$$c_R = \frac{0.87 + 1.12\nu}{1+\nu}\sqrt{\frac{G}{\rho}} \tag{3.7}$$

As ν varies from 0 to 0.5, c_R varies from $0.87c_T$ to $0.96c_T$. Besides, for $\nu = 0.2$, typical value for concrete, $c_R = 0.91c_T$ and for $\nu = 0.3$, typical value for steel, $c_R = 0.93c_T$.

3.2 LAMB WAVE THEORY

In thin-plate specimens, where the thickness is around the bulk wave wavelength, when an ultrasonic pulse reaches the opposite side, it is created a confinement of a portion of the propagated energy, which reflects continuously at the mean borders and travels parallel to the boundaries. This phenomenon generates Lamb waves, also called Plate waves.

Lamb waves are dispersive because they have different modes and velocities for each frequency/thickness combination, which differentiates them from other surface and

interface waves. These waves are divided into antisymmetric (A) and symmetric (S) modes, whose typical movements are shown in Figure 3.1.

Figure 3.1 - Lamb wave motion

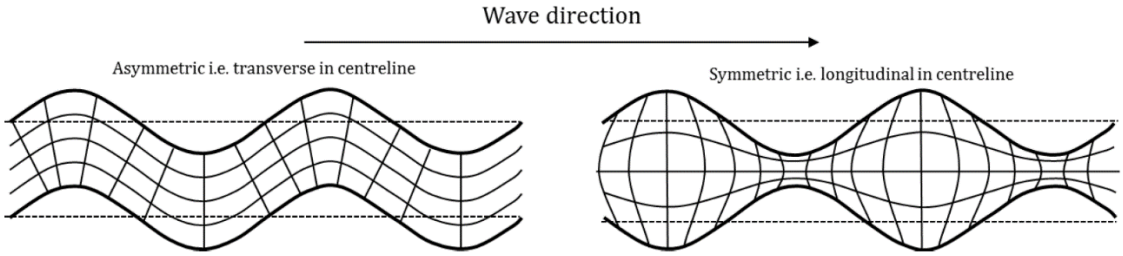

Source: Marks *et al*. (2016)

The symmetric mode, also called extensional mode, is often referred to as longitudinal mode and denoted as $L(n,m)$, where n represents the Bessel function order considered, which is 0 for this mode, and m is the wave mode order. Since m and n can assume infinite values, there are also infinite longitudinal modes (Zemanek, 1972). Thus, the first and lowest symmetric mode is designated as $L(0,1)$, as shown in Figure 3.2.

Figure 3.2 - First Lamb wave modes in a rod

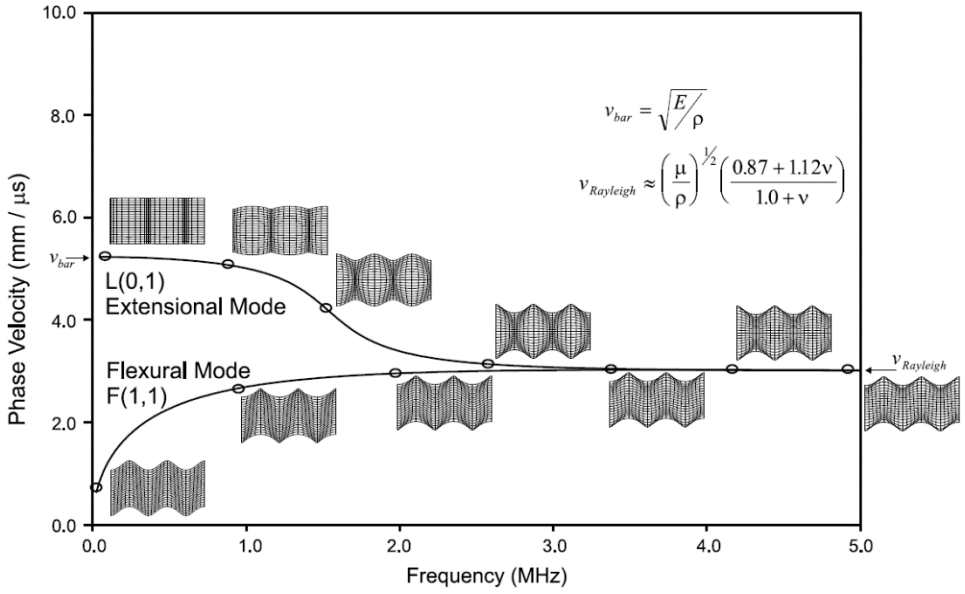

Source: Lowe and Pavlakovic, 2013

The longitudinal mode tends to a longitudinal bulk wave as the frequency approaches zero. Disregarding the Poisson effect in a rebar, the phase velocity at zero

frequency is the longitudinal bulk wave velocity, simplified as $v = \sqrt{E/\rho}$. For the specific case of steel, $v \cong 5200$ m/s.

Another symmetric mode is the Torsional, whose fundamental mode, $T(0,1)$, represents a uniform twisting of the bar and is not dispersive, with the same velocity as bulk shear waves. As it is non-dispersive and is not the fastest mode, this wave is not considered in this study.

The antisymmetric mode is usually called Flexural mode, $F(n,m)$, and the first antisymmetric mode is designated as $F(1,1)$. At zero frequency, it is similar to shear bulk wave shape, with pure bending.

As the frequency increases, all modes tend to move like a Rayleigh wave and consequently to have its velocity.

For sufficiently small frequency and thickness, only the zero order A_0, also called $F(1,1)$, and S_0, also called $L(0,1)$, can exist. As these parameters increase, higher order modes appear, and the phase velocities of the lower order modes tend to the Rayleigh wave one. In addition, as thickness increases, it becomes more challenging to distinguish between Rayleigh and Lamb waves.

In the cases of multilayered plates, due to the boundary conditions, which significantly influence their behavior, the analytical solution of Lamb waves becomes very difficult and sometimes impossible (Sadler and Maev, 2007).

One method for producing Lamb waves is to apply a normal perturbation to the plate surface, even if it is immersed. Another way to excite the plate is by varying the wedge angle of ultrasound incidence, what allows to excite the plate in any possible modes on a selective basis and, because of that, it is widely use.

3.3 LAMB WAVE FORMULATION

Lamb (1917) added another interface to the media of Rayleigh's problem and proposed a wave propagation formulation for flat solids with finite thickness and surrounded by vacuum. This work resulted in two characteristic equations, one for

symmetric modes and another for antisymmetric modes, whose roots yield the wave dispersion curves.

The following equations are based on the notation of Worden (2001) and the geometry shown in Figure 3.3, where 2d is the plate thickness, x axis is the wave propagation direction and z axis is perpendicular to the surfaces. Furthermore, the analysis is simplified in assumption of plane strain, in xz plane.

Figure 3.3 - Geometrical parameters of reference

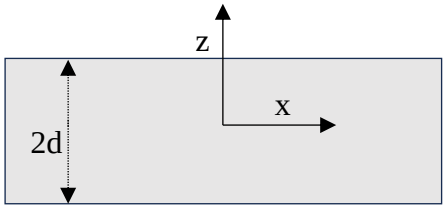

Source: Own elaboration

Both solutions for Lamb waves consider the in-plane displacement u also a function of z. In the first solution, $u(z) = u(-z)$, what is related to the symmetric modes. In the second one, $u(-z) = -u(z)$, what refers to the antisymmetric modes.

For symmetric modes, there are the Equations (3.8) and (3.9).

$$u = (ikA\cos(pz) + qB\cos(qz))e^{ik(x-ct)}. \tag{3.8}$$

$$w = (-pA\sin(pz) - ikB\sin(qz))e^{ik(x-ct)}. \tag{3.9}$$

For antisymmetric modes, there are the Equations (3.10) and (3.11).

$$u = (ikC\sin(pz) - qD\cos(qz))e^{ik(x-ct)}, \tag{3.10}$$

$$w = (pC\cos(pz) - ikD\cos(qz))e^{ik(x-ct)} \tag{3.11}$$

where:

$$p = \frac{\omega}{\sqrt{c_L^2 - c^2}}, q = \frac{\omega}{\sqrt{c_T^2 - c^2}} \tag{3.12}$$

and A, B, C and D are arbitrary constants.

For specimens in vacuum, free-stress surfaces, $\sigma_{xz} = \sigma_{zz} = 0$ on $z = \pm d$, the two characteristic equations only have nontrivial solutions. The Equation (3.13) corresponds to Symmetric modes and Equation (3.14) to antisymmetric modes.

$$\frac{\tan(qd)}{\tan(pd)} = -\frac{4k^2pq}{(q^2 - k^2)^2}. \tag{3.13}$$

$$\frac{\tan(pd)}{\tan(qd)} = -\frac{4k^2pq}{(q^2 - k^2)^2}. \tag{3.14}$$

3.4 LAMB WAVE ACOUSTOELASTICITY

The formulas developed here are based on the reference axes shown in Figure 3.4. Besides, three solid states are considered: unstrained, which is the natural frame without stress; strained, an initial reference frame with the application of the initial stress; and perturbed, during the wave propagation in the strained state.

Figure 3.4 - Reference axes

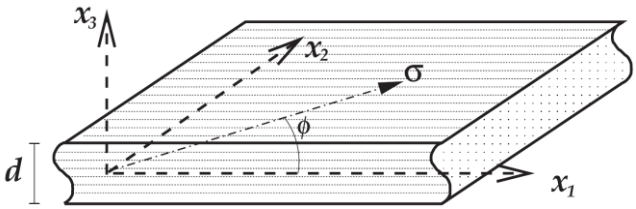

Source: Kubrusly, Braga and Weid (2016)

In this section, an anisotropic stressed medium is considered. For this case, the motion equation is presented in Equation (3.15).

$$A_{ijkl}\frac{\partial^2 u_k}{\partial x_j \partial x_l} = \rho \frac{\partial^2 u_i}{\partial t^2} \tag{3.15}$$

where u_i is the incremental displacement due to wave propagation and ρ is the density in unstrained configuration.

The incremental stress T_{ij} is calculated through the constitutive relationship for the final configuration, due to wave propagation in a prestressed medium, given by Equation (3.16).

$$T_{ij} = B_{ijkl}\frac{\partial u_k}{\partial x_l} \tag{3.16}$$

The fourth-order tensors $\boldsymbol{A}$ and $\boldsymbol{B}$ in undeformed state are obtained using Equations (3.17) and (3.18).

$$A_{\alpha\beta\gamma\delta} = s^i_{\beta\delta}\delta_{\alpha\gamma} + C_{\alpha\beta\gamma\delta} + C_{\alpha\beta\lambda\delta}\frac{\partial u^i_\gamma}{\partial \xi_\lambda} + C_{\lambda\beta\gamma\delta}\frac{\partial u^i_\alpha}{\partial \xi_\lambda} + C_{\alpha\beta\lambda\delta\zeta\eta}\varepsilon_{\zeta\eta} \tag{3.17}$$

$$B_{\alpha\beta\gamma\delta} = C_{\alpha\beta\gamma\delta} + C_{\alpha\beta\lambda\delta}\frac{\partial u^i_\gamma}{\partial \xi_\lambda} + C_{\alpha\beta\lambda\delta\zeta\eta}\varepsilon_{\zeta\eta} \tag{3.18}$$

where $s^i_{\beta\delta}$ and $\varepsilon_{\zeta\eta}$ are the initial stress and strain in the deformed state, respectively, u^i_γ is the initial displacement from undeformed to deformed state, and ξ_λ is the position in the undeformed state.

In strained stated, before wave propagation, these tensors can be written as Equations (3.19) and (3.20).

$$A_{IJKL} = s^i_{JL}\delta_{IK} + C_{IJKL}\varepsilon_{NN} + B_{IJKL} \tag{3.19}$$

$$B_{IJKL} = C_{IJKL} + C_{MJKL}\frac{\partial u_I^i}{\partial X_M} + C_{IMKL}\frac{\partial u_J^i}{\partial X_M} + C_{IJML}\frac{\partial u_K^i}{\partial X_M} + C_{IJKM}\frac{\partial u_L^i}{\partial X_M} - C_{IJKL}\varepsilon_{NN} + C_{IJKLMN}\varepsilon_{MN} \tag{3.20}$$

where X_M is the position in the strained state.

The solutions are the type presented in Equation (3.21), which represents plane waves.

$$u_m = U_m e^{i\kappa(x_1 + \alpha x_3 - ct)} \tag{3.21}$$

where κ and $\alpha\kappa$ are the wavenumber in the directions x_1 and x_3, respectively, and c is the phase velocity.

Substituting Equation (3.21) in Equation (3.15), equation of motion, it yields a form of solution known as Christoffel equation, represented in Equation (3.22).

$$K_{ik}U_k = 0 \tag{3.22}$$

The tensor K_{ik} is obtained by the second spatial and temporal derivatives of Equation (3.21) into Equation (3.15), which results in Equation (3.23).

$$K_{ik} = \rho c^2 \delta_{ik} - A_{i1k1} - \alpha(A_{i1k3} + A_{i3k1}) - \alpha^2 A_{i3k3} \tag{3.23}$$

Since $A_{ijkl} = A_{klij}$ in both strained and unstrained state, $\boldsymbol{K}$ is symmetric and, consequently, $K_{ik} = K_{ki}$. Doing $\det(\boldsymbol{K}) = 0$, for each value c, six roots of α are obtained.

In the case of isotropic medium in both unstrained and strained submitted to equi-biaxial homogeneous stress state in x_1x_2 plane, this plane remains one of the material symmetries even after deformed. Thus, $\boldsymbol{K}$ has the components in Equations (3.24) – (3.29).

$$K_{11} = \rho c^2 - A_{1111} - \alpha^2 A_{1313} \tag{3.24}$$

$$K_{22} = \rho c^2 - A_{2121} - \alpha^2 A_{2323} \tag{3.25}$$

$$K_{33} = \rho c^2 - A_{3131} - \alpha^2 A_{3333} \tag{3.26}$$

$$K_{12} = K_{21} = -A_{1121} - \alpha^2 A_{1323} \tag{3.27}$$

$$K_{13} = K_{31} = -\alpha(A_{1133} + A_{1331}) \tag{3.28}$$

$$K_{23} = K_{32} = -\alpha(A_{2133} + A_{2331}) \tag{3.29}$$

The coefficients of the odd powers of α are zero, which leads to a cubic equation in α^2, as presented in Equation (3.30).

$$P_6\alpha^6 + P_4\alpha^4 + P_2\alpha^2 + P_0 = 0 \tag{3.30}$$

where P_i are presented in Appendix D. For each value of c, there are 6 roots of α, 3 corresponding to up-going bulk waves and three down-going bulk waves.

Finally, it is necessary to satisfy the stress-free boundary conditions on the plate surfaces, where $x_3 = \pm\, d/2$. For this, displacement ratios of U_1, U_2 and U_3 are obtained for each α, as shown in Equation (3.31).

$$V_q = \frac{U_{2q}}{U_{1q}}, \qquad W_q = \frac{U_{3q}}{U_{1q}}, \qquad q = 1,2 \ldots 6 \tag{3.31}$$

Equation (3.22) enables these ratios to be written in terms of K_{mn} and the corresponding α_q. The total displacement of the resulting Lamb wave is considered a superposition of the displacements of six partial waves, and the Equation (3.32) needs to be satisfied.

$$\{u_1, u_2, u_3\} = \sum_{q=1}^{6} \{1, V_q, W_q\} U_{1q} e^{i\xi(x_1 + \alpha_q x_3 - ct)} \tag{3.32}$$

Using Equation (3.32) in Equation (3.16), Equation (3.33) is obtained.

$$\{T_{33}, T_{13}, T_{23}\} = \sum_{q=1}^{6} i\xi\{D_{1q}, D_{2q}, D_{3q}\}U_{1q}e^{i\xi(x_1+\alpha_q x_3-ct)} \tag{3.33}$$

where:

$$D_{1q} = B_{3311} + B_{3312}V_q + \alpha_q B_{3333}W_q, \tag{3.34}$$

$$D_{2q} = \alpha_q\left(B_{1313} + B_{1323}V_q\right) + B_{1331}W_q, \tag{3.35}$$

$$D_{3q} = \alpha_q\left(B_{1323} + B_{2323}V_q\right) + B_{1332}W_q. \tag{3.36}$$

To ensure stress-free boundary conditions at the surface, where $x_3 = \pm\, d/2$, T_{13}, T_{23} and T_{33} must be zero, which yields six equations in terms of six displacement amplitudes, U_{1q}, of the six partial waves, $q = 1, 2 \ldots 6$. For this, and to obtain nontrivial solutions for the displacement amplitudes:

$$\begin{vmatrix} D_{11}E_1 & D_{12}E_2 & D_{13}E_3 & D_{14}E_4 & D_{15}E_5 & D_{16}E_6 \\ D_{21}E_1 & D_{22}E_2 & D_{23}E_3 & D_{24}E_4 & D_{25}E_5 & D_{26}E_6 \\ D_{31}E_1 & D_{32}E_2 & D_{33}E_3 & D_{34}E_4 & D_{35}E_5 & D_{36}E_6 \\ D_{11}\tilde{E}_1 & D_{12}\tilde{E}_2 & D_{13}\tilde{E}_3 & D_{14}\tilde{E}_4 & D_{15}\tilde{E}_5 & D_{16}\tilde{E}_6 \\ D_{21}\tilde{E}_1 & D_{22}\tilde{E}_2 & D_{23}\tilde{E}_3 & D_{24}\tilde{E}_4 & D_{25}\tilde{E}_5 & D_{26}\tilde{E}_6 \\ D_{31}\tilde{E}_1 & D_{32}\tilde{E}_2 & D_{33}\tilde{E}_3 & D_{34}\tilde{E}_4 & D_{35}\tilde{E}_5 & D_{36}\tilde{E}_6 \end{vmatrix} = 0 \tag{3.37}$$

where $E_q = e^{i\xi\alpha_q d/2}$ and $\tilde{E}_q = e^{-i\xi\alpha_q d/2}$.

Manipulating rows and columns, Equation (3.37) is reduced into Equations (3.38) and (3.39), which correspond to the symmetric and antisymmetric Lamb wave modes, respectively.

$$f_s(\omega, c) = D_{11}G_1\cot(\gamma\alpha_1) + D_{13}G_3\cot(\gamma\alpha_3) + D_{15}G_5\cot(\gamma\alpha_5) = 0 \tag{3.38}$$

$$f_a(\omega, c) = D_{11}G_1\tan(\gamma\alpha_1) + D_{13}G_3\tan(\gamma\alpha_3) + D_{15}G_5\tan(\gamma\alpha_5) = 0 \tag{3.39}$$

where $\gamma = \xi d/2 = \omega d/(2c)$, ω is the angular frequency, and G_m are calculated by Equations (3.40) – (3.42).

$$G_1 = D_{23}D_{35} - D_{33}D_{25} \tag{3.40}$$

$$G_3 = D_{31}D_{25} - D_{21}D_{35} \tag{3.41}$$

$$G_5 = D_{21}D_{33} - D_{31}D_{23} \tag{3.42}$$

The solution of Equations (3.38) and (3.39) yields the dispersion curves of phase velocity and angular frequency for both symmetric and antisymmetric modes, respectively. These solutions require numerical methods, and one of them is proposed by Gandhi, Michaels and Lee (2012).

3.5 FORMULATION OF GUIDED WAVE IN REBARS

For the specific case of free bar, Pochhammer (1876) and Chree (1889) were the first authors to investigate and propose solutions for the guided waves. Pochhammer's displacements are given by Equations (3.43), (3.44) and (3.45), in terms of cylindrical coordinates r, θ and z.

$$u_r = U \cos\theta \, e^{i(\gamma z + pt)}. \tag{3.43}$$

$$u_\theta = V \sin\theta \, e^{i(\gamma z + pt)}. \tag{3.44}$$

$$u_z = W \cos\theta \, e^{i(\gamma z + pt)} \tag{3.45}$$

where w is the circular frequency, obtained as $w = 2\pi\Omega$, γ is the propagation constant or wavenumber, $\gamma = w/v = 2\pi/\lambda$, where v is the phase velocity and λ is the wavelength, and

$$U = A\frac{\partial J_1(hr)}{\partial r} + B\gamma\frac{\partial J_1(kr)}{\partial r} + C\frac{J_1(kr)}{r}, \tag{3.46}$$

$$V = -A\frac{J_1(hr)}{r} - B\gamma\frac{J_1(kr)}{r} - C\frac{\partial J_1(kr)}{\partial r}, \tag{3.47}$$

$$W = iA\gamma J_1(hr) - iBk^2 J_1(kr). \tag{3.48}$$

In equations above, J_1 is a Bessel's function of order unity, A, B and C are arbitrary constants and

$$h^2 = w^2/v_L^2 - \gamma^2, \tag{3.49}$$

$$k^2 = w^2/v_S^2 - \gamma^2. \tag{3.50}$$

For convenience, dimensionless wave numbers are introduced, α, β, ζ, and frequency, Ω, in terms of the radius of the cylinder, a, and the shear velocity, v_S. These considerations result in Equation (3.51).

$$\alpha = ha, \qquad \beta = ka, \qquad \zeta = \gamma a, \qquad \Omega = wa/v_S. \tag{3.51}$$

Thus, the Equations (3.49) and (3.50) become Equations (3.52) and (3.53).

$$\alpha^2 = \frac{\Omega^2}{\varphi^2} - \zeta^2, \tag{3.52}$$

$$\beta^2 = \Omega^2 - \zeta^2 \tag{3.53}$$

where

$$\varphi^2 = \frac{(\lambda + 2\mu)}{\mu} = \frac{2(1-\nu)}{(1-2\nu)}, \tag{3.54}$$

where λ and μ are Lamé's constants and ν is Poisson's ratio.

Considering stress free bar surface and eliminating the constants A, B and C, Zemanek (1972) showed that the only nontrivial solutions are obtained making the following determinant equal to zero, what is a new format of the Pochhammer's frequency equation, called here Equation (3.55).

$$\begin{vmatrix} A_{11} & A_{12} & A_{13} \\ A_{21} & A_{22} & A_{23} \\ A_{31} & A_{32} & A_{33} \end{vmatrix} = 0 \tag{3.55}$$

where:

$$A_{11} = [n^2 - 1 - (\Omega^2/2) + \zeta^2]J_n(\alpha), \tag{3.56}$$

$$A_{12} = (n^2 - 1 - \beta^2)J_n(\beta), \tag{3.57}$$

$$A_{13} = 2(n^2 - 1)[\beta J_{n-1}(\beta) - nJ_n(\beta)] - \beta^2 J_n(\beta), \tag{3.58}$$

$$A_{21} = \alpha J_{n-1}(\alpha) - (n + 1)J_n(\alpha), \tag{3.59}$$

$$A_{22} = \beta J_{n-1}(\beta) - (n + 1)J_n(\beta), \tag{3.60}$$

$$A_{23} = [2n^2 + 2n - \beta^2]J_n(\beta) - 2\beta J_{n-1}(\beta), \tag{3.61}$$

$$A_{31} = \alpha J_{n-1}(\alpha) - nJ_n(\alpha), \tag{3.62}$$

$$A_{32} = \{1 - [\Omega^2/(2\zeta^2)]\}[\beta J_{n-1}(\beta) - nJ_n(\beta)], \tag{3.63}$$

$$A_{33} = n^2 J_n(\beta). \tag{3.64}$$

The variable n represents the type of the guided wave, thus $n = 0$ is related to symmetric modes, often called longitudinal mode $L(0, m)$, and $n \geq 1$ represents the antisymmetric modes, also known as flexural mode $F(1, m)$. The variable m is the mode

branch, thus the first and lowest branch of the longitudinal mode is designated by $L(0,1)$, whereas $F(1,1)$ is the first fundamental flexural mode.

To simplify the formulation above, if $n = 0$, the determinant results into two equations for symmetric modes, Equations (3.65) and (3.66).

$$\beta J_0(\beta) - 2J_1(\beta) = 0, \tag{3.65}$$

$$[\Omega^2 - 2\zeta^2]^2 J_0(\alpha)J_1(\beta) + 4\zeta^2\alpha\beta J_0(\beta)J_1(\alpha) - 2\Omega^2\alpha J_1(\alpha)J_1(\beta) = 0. \tag{3.66}$$

The Equation (3.65) models the Torsional waves and Equation (3.66) is related to longitudinal waves. In this work, as the frequency range only produces the first torsional mode, which is not dispersive and has a constant velocity equal to the shear bulk wave velocity, the torsional modes are not considered. Therefore, from now on, the longitudinal mode is simply called symmetric mode.

On the other hand, Pao and Mindlin (1960) proposed a simplification on Pochhammer's frequency equation for the flexural modes, presented in Equation (3.67).

$$J_1(\alpha)J_1^2(\beta)\left[f_1\mathcal{J}_\beta^2 + f_2\mathcal{J}_\alpha\mathcal{J}_\beta + f_3\mathcal{J}_\beta + f_4\mathcal{J}_\alpha + f_5\right] = 0 \tag{3.67}$$

where:

$$f_1 = 2(\beta^2 - \zeta^2)^2, \tag{3.68}$$

$$f_2 = 2\beta^2(5\,\zeta^2 + \beta^2), \tag{3.69}$$

$$f_3 = \beta^6 - 10\beta^4 - 2\beta^4\,\zeta^2 + 2\beta^2\,\zeta^2 + \beta^2\,\zeta^4 - 4\,\zeta^4, \tag{3.70}$$

$$f_4 = 2\beta^2(2\beta^2\,\zeta^2 - \beta^2 - 9\,\zeta^2), \tag{3.71}$$

$$f_5 = \beta^2(-\beta^4 + 8\beta^2 - 2\beta^2\,\zeta^2 + 8\,\zeta^2 - \zeta^4). \tag{3.72}$$

And

$$\mathcal{J}_x \equiv \mathcal{J}_1(x) \equiv xJ_0(x)/J_1(x) \tag{3.73}$$

is the Onoe's function (Onoe, 1958) of the first kind and order unity.

Finally, phase and group velocities, v and v_g respectively, are given by Equation (3.74).

$$v \equiv \frac{w}{\gamma} = \frac{v_S \Omega}{\zeta};\ v_g \equiv \frac{dw}{d\gamma} = \frac{v_S d\Omega}{d\zeta}. \tag{3.74}$$

A Bessel's function of order n is defined as shown in Equation (3.75) and a Bessel's property used to model the dispersive curves is presented in Equation (3.76).

$$J_n(x) = \sum_{s=0}^{\infty} \frac{(-1)^s}{s!\,(n+s)!} \left(\frac{x}{2}\right)^{n+2s}. \tag{3.75}$$

$$J_{-n}(x) = (-1)^n J_n(x). \tag{3.76}$$

Other authors present a theoretical analysis of Pochhammer's equation (Meitzler, 1961; Gadzhibekov and Ilyashenko, 2021), some of them focused on the zero modes (Laurent et. al., 2015; Hussain, Ahmad and Ozair, 2017), some showed these equations into boundary finite element method (Gunawan; Hirose, 2005; Gravenkamp, Birk and Song, 2014) and another approach line proposed a simplified approximation (Widehammar; Gradin; Lundberg, 2001; Brizard; Jacquelin; Ronel, 2019; Brizard; Jacquelin, 2022).

3.6 GUIDED WAVES IN EMBEDDED REBARS

In the case of multilayered media with cylindrical solids, such as bars in reinforced concrete, which are also called leaky cylindrical systems, the modeling is much more difficult than in the free boundaries case. This difficulty is mainly due to the complex

Bessel's functions that need to be calculated, what is, in some cases, impossible (Lowe and Pavlakovic, 2013).

Lowe (1995) makes a review of the main matrix technique formulations on literature, while Pavlakovic and Lowe (1999) proposed an approach to model dispersion curves in multilayered media with cylinders and Pavlakovic *et. al*. (1997) developed a general program that creates dispersion curves, resulting in the software Disperse®.

Guided waves in cylinders embedded in solid are highly dispersive, and there is a great energy attenuation, where the wave can leak into the solid as Longitudinal and Shear bulk waves. The leakage mode depends on the wave phase velocity, as shown in Figure 3.5. In this figure, the two horizontal lines correspond to the bulk wave velocity in the surrounding solid. If the region considered is located below the line that defines the bulk shear velocity, there is no wave leakage to the solid (a), called non-leaky region, if it is located between longitudinal and shear velocity (b), only shear waves are leaked, and if the region is above the longitudinal velocity line (c), both shear and longitudinal waves leak into the surrounding medium. These leakages are illustrated in Figure 3.6.

Figure 3.5 - Leakage regions

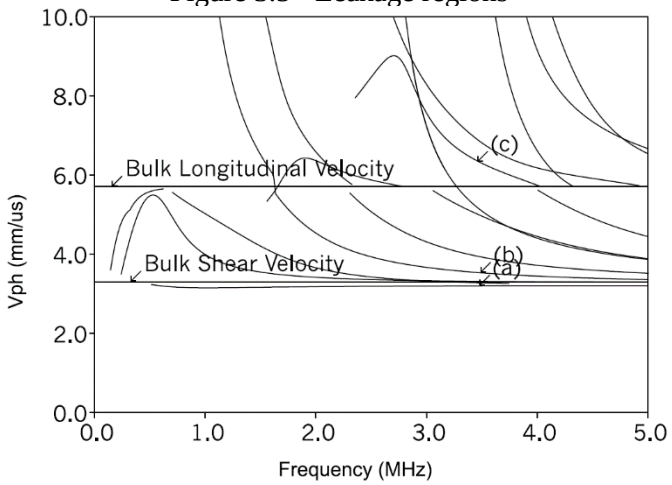

Source: Lowe and Pavlakovic (2013)

Figure 3.6 - Types of leakage

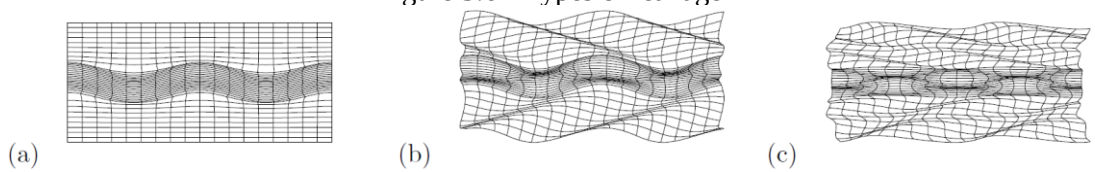

Source: Lowe and Pavlakovic (2013)

Therefore, there are two manners for considering the guided wave propagation in multilayered elements, mainly in bars embedded in concrete:

a) The propagation occurs throughout the entire element: the complete movement of the wave involves both materials, one inner and another outer, and there are no leaky waves. The wave propagates as if it was a single material. The dispersion curves are a result of a weighting of the materials.
b) The propagation occurs only in the inner material: the waves are called leaky guided waves, which means that while these waves propagate in the inner part, bulk longitudinal and/or shear waves are leaked in the surrounding material, generated from the guided wave. The dispersion curves are related to the inner material regarding its boundary conditions.

For these modelings, the following software can be used: PCDISP® (Seco *et al.*, 2002), which uses the Multiple Layer Matrix approach (Seco; Jiménez, 2012); GUIGUW®, developed by Bocchini, Marzani and Viola (2011) and based on Semi-Analytical Finite Element (SAFE) method; and the commercial software called DISPERSE® (Lowe; Pavlakovic, 2013).

Case ‘a’ can be modeled in all software, where reinforced concrete is modeled as a cylindrical sample with an inner bar surrounded by cylindrical concrete layer with thickness equal to the cover.

For modeling this scenario, some works used PCDISP® (Zima and Rucka, 2017; Zima and Rucka, 2018) and some used GUIGUW® (Zima and Kędra, 2019, Zima and Kędra, 2021). Furthermore, Aseem and Ng (2021) and Aseem and Ng (2023) justified the simplicity of the first case to model it in DISPERSE®.

Guided waves are produced only when the bulk wave wavelength is approximately equal to or greater than the guide thickness. Considering this, a simplified analysis for case ‘a’ can be done as follows:

- If a total diameter of 5 cm (steel plus concrete) is considered, with a group velocity of 4,000 m/s and using the Equation (2.2), that relates velocity to frequency, the maximum wave frequency to produce guided waves is around 80 kHz, which yields a possible frequency range of 20 – 80 kHz.

This limitation makes the modeling of case ‘a’ questionable in terms of representing the real problem.

Case ‘b’ is commonly modeled by DISPERSE®, where the reinforced concrete is modeled as a rebar embedded in an infinite concrete medium. Additionally, it is considered perfect bonding between materials, like in case ‘a’.

Remaking the previous analysis for case ‘b’:

- Considering a rebar diameter of 10 mm, the maximum wave frequency to produce guided waves is around 400 kHz, yielding a possible frequency range of 20 – 400 kHz. As this frequency range is commonly used for concrete samples, this analysis makes case ‘b’ more coherent with real conditions.

For modeling case ‘b’, most researchers used the software DISPERSE® (Sharma; Mukherjee, 2014; Sharma *et al*., 2021). In contrast, Sun and Zhu (2020) modified PCDISP to “handle multilayer structures with an infinite outer layer and calculate the dispersion curves with leakage” (Sun; Zhu, 2020, p. 2).

3.7 HIGHLIGHTS OF CHAPTER 3

An abstract of the chapter is listed here:

a) As guided waves propagate long distances through the guides, they are often used to analyze long elements with a single application. They are mainly utilized to identify flaws, given their high sensitivity to defects.
b) The Rayleigh wave velocity is given by Equation (3.7). c_R varies from $0.87c_T$ to $0.96c_T$. Besides, for $\nu = 0.2$, typical value for concrete, $c_R = 0.91c_T$ and for $\nu = 0.3$, typical value for steel, $c_R = 0.93c_T$.
c) The longitudinal mode, also called symmetric mode S_0, is denoted as $L(n,m)$, where n represents the Bessel function order considered, which is 0 for this mode, and m is the wave mode order. The first and lowest mode is $L(0,1)$.

d) For specimens in vacuum, free-stress surfaces, $\sigma_{xz} = \sigma_{zz} = 0$ on $z = \pm d$, the two characteristic equations are Equation (3.13), for Symmetric modes, and Equation (3.14), for antisymmetric modes.

e) The acoustoelastic effect for Lamb waves is quantified by Equations (3.38) and (3.39), which correspond to the symmetric and antisymmetric Lamb wave modes, respectively.

f) The characteristic equation of longitudinal guided waves and flexural guided waves in rebars are represented by Equation (3.66) and (3.67), respectively.

a) In multilayered media with cylindrical solids, the guided wave propagation occurs in a leaky cylindrical system. While these waves propagate in the guide, bulk longitudinal and/or shear waves leak in the surrounding material. The leakage mode depends on the wave phase velocity.

4 SYSTEMATIC REVIEW

In this chapter, a systematic review is carried out, where the most relevant issues about the state of art are discussed. For this, the research parameters used in each platform are presented, along with the main papers obtained and their key information.

The following research platforms were used: Periódicos CAPES, Web of science, Science direct and Scopus. In Appendix C, the papers considered for the review are presented, totaling 87, as well as the main properties of each search. Despite being listed by the platforms, the papers not strictly related to the present study and those duplicated were not considered.

4.1 RESEARCH METHODS

The objective of the searches was to answer the main questions related to the subject of the present study. For this, questions were listed in Table 4.1, along with the respective expected results.

Table 4.1 - Key questions for the searches

(continue)

Research questions	Expected results
Q1. How are Lamb waves used in plain concrete structures?	**1.** The manner how these waves are produced; **2.** For which analyzes they are used.
Q2. How is the acoustoelasticity effect analyzed in reinforced concrete structures?	**1.** Which waves are considered; **2.** If it is possible to detect this effect; **3.** Which materials are considered for the analyses.
Q3. Are guided waves used for the acoustoelastic effect analysis?	**1.** The sensitivity of these waves for acoustoelasticity; **2.** To know, among guided waves, the most used.

Table 4.1 - Key questions for the searches

(conclusion)

Research questions	Expected results
Q4. Do the researchers assess acoustoelasticity in reinforced concrete elements through guided waves?	**1.** The analysis methods; **2.** The ultrasound application procedure.
Q5. How are the dispersion curves in cylinders determined?	**1.** The main formulas and approaches and the respective plot procedure; **2.** If there are well-stablished methods.
Q6. How to solve Pochhammer equations?	**1.** Strategies for solving the characteristic equations of guided waves in rods.
Q7. How do the authors use software for obtaining dispersion curves in cylinders?	**1.** To list software for modeling guided waves in rods; **2.** Which wave velocity are obtained for rebars in reinforced concrete.

Source: Own elaboration

Based on the questions in Table 4.1 and the corresponding expected results, specific keywords were selected for searches in the scientific databases. Some words were restricted to title, abstract and paper keywords, while others could appear in any field of the paper. The use of each keyword is detailed in Appendix C for each search. Accordingly, only the keywords, without conjunctions, are listed in Table 4.2.

Table 4.2 - Search keywords

(continue)

Research questions	keywords
Q1	Lamb wave; Concrete
Q2	Acoustoelastic; Acoustoelasticity; reinforced concrete
Q3	Acoustoelastic; Acoustoelasticity; Lamb; Guided; Rayleigh

Table 4.2 - Search keywords

(conclusion)

Research questions	keywords
Q4	Acoustoelastic; Acoustoelasticity; Lamb; reinforced concrete
Q5	Lamb; dispersion curve; cylinder; steel bar; ultrasound; ultrasonic
Q6	Pochhammer; dispersion; dispersion curve; cylinder; rod; guided wave
Q7	Disperse; software; concrete; guided wave; reinforced concrete

Source: Own elaboration

After obtaining the papers for each search, some exclusion criteria were applied. The purpose of this step is to filter only the most relevant papers that could address the concerns. These criteria were defined for each question based on its expected key information. The exclusion criteria are:

a) No answer is provided by the title, as primary exclusion, and by the abstract, as secondary exclusion;
b) Not related to engineering or physics;
c) No use of ultrasonic waves;
d) Papers focused on thermal analysis without the acoustoelastic theory explanation.

This systematic review method yields the papers presented in Appendix C, and their key information is summarized and discussed in the following sections.

4.2 NOMENCLATURE OF GUIDED WAVES

In thin specimens where the thickness is around the wavelength of bulk waves, when an ultrasonic pulse reaches the opposite side, a portion of energy leaks into the surrounding material and another portion remains confined between the boundaries, reflecting continuously at mean boundaries and traveling parallel to them, using the entire

specimen thickness for the complete movement. This last phenomenon generates the guided waves, and when the guide specimen is a plate, the waves are known as Lamb waves or Plate waves.

In most papers, when the guide has a circular cross section, the authors only use the designation “guided waves”, and Lamb waves exclusively for plates; despite being related to the same phenomenon. Gunawan and Hirose (2005) showed asymptotic behavior between dispersion curves of guided waves in bars with arbitrary cross-section and Lamb waves in 2D plates. A similar conclusion was presented by Zhang *et al*. (2018), who stated that for long wavelengths in low frequency, the rod-like model is similar to a plate-like model in uniform medium. It strengthens that guided waves in rods and Lamb waves in plates are related to the same phenomenon, what makes both waves a particular case of the general guided wave. For this reason, in this work the term “guided waves” is used.

4.3 CHRONOLOGY OF RESEARCH DEVELOPMENT

Figure 4.1 shows the distribution of the papers by year.

Figure 4.1 - Papers by year

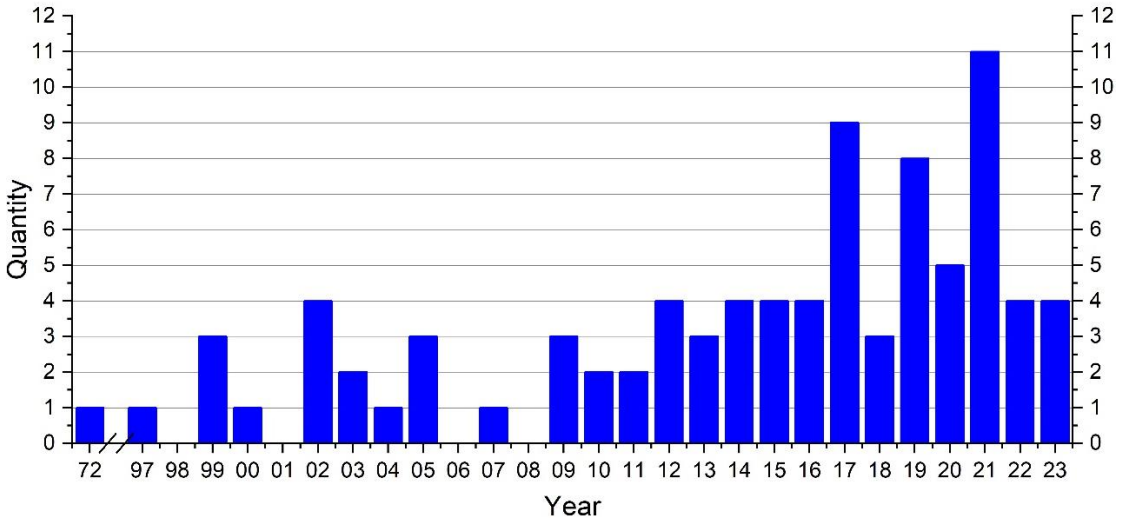

Source: Own elaboration

Despite the first publications on guided waves in free bars being old (Pochhammer, 1876; Chree, 1889), the formulations were challenging to handle and

solve. These formulas were better addressed by Zemanek (1972), which, in addition to improved computers, enabled a greater number of publications at the end of the twentieth century.

The main works began to show up around 1999, when the first study about acoustoelasticity using Lamb waves was published (Delsanto *et al*., 1999). In the same year, one of the pioneer studies about dispersion curves of two-layered cylinders was published (Kley *et al*., 1999). The efforts for solving the dispersion curves resulted in the first software for guided waves, such as DISPERSE®, PCDISP and later, GUIGUW.

From 1999 to 2008, the number of studies was not constant, with an average of 1.5 paper per year and no publications in 2001, 2006 and 2008. The subject gained momentum from 2009, mostly because of the commercial and more stable versions of the above software and the alternative numerical and analytical solutions for the dispersion curves, like the proposition of Honarvar, Enjilela and Sinclair (2009).

Some works proposed approximations and alternative methods and solutions for Pochhammer equations (Brizard; Jacquelin; Ronel, 2019; Kari, 2002, Elmaimouni *et al*., 2005, Honarvar; Enjilela; Sinclair, 2009; Höhne; Prager; Gravenkamp, 2015).

Most of the papers, 51%, were published in the last 6 years, with a peak in 2021, with 11 works.

4.4 TYPE OF MATERIAL STUDIED

Figure 4.2 shows the distribution of works according to the specimen analyzed.

Figure 4.2 - Distribution of papers by material studied

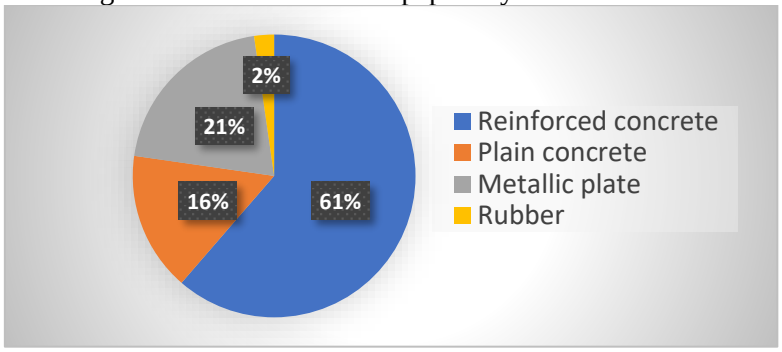

Source: Own elaboration

As expected, most studies use reinforced concrete as the specimen, but there are many of them with plain concrete and metallic plate. Plain concrete is mainly utilized with bulk waves for detecting heterogeneities and acoustoelastic effect. Conversely, metallic plate represents the oldest and most consolidated research branch, related to Lamb waves for detecting stress state and defects. It explains the higher number of metallic plate, 21%, compared to plain concrete, 16%. Finally, there is only one paper using rubber as the main material.

Among these papers, there are 3 reviews. Gorgin, Luo and Wu (2020) provide a review about structural health monitoring systems using Lamb waves, while the works of Ohtsu (2016) and Li *et al*. (2021) focus on health monitoring of concrete through guided waves.

4.5 DEBONDING

The first study on the behavior of elastic waves in reinforced concrete was conducted by Yamakawa and Murakami (1997). They presented numerical results on the influence of longitudinal bars on the generation of guided waves and concluded that the influence of stirrups was negligible, mainly because of their volume relative to the longitudinal rebars.

In the last 3 years, 37% of the works were related to debonding. Jung *et al*. (2000) used guided waves to analyze defects caused by debonding between concrete and rebar. The authors indicated that the debonding shifts the dispersion curves slightly towards the right. Following this line of research, many works were developed in the subsequent years and even nowadays, as Aseem and Ng (2023) and Liao and Qiao (2023). It is an important research branch, representing 25% of all papers.

In a few studies, debonding was induced by corrosion (Farhidzadeh; Salamone, 2015; Sharma *et al*., 2021). The works in this line not only focus on debonding detection but also on its extent and location. Finally, a few papers, representing 10% of the total, focused on defects detection in other materials and specimens.

4.6 ACOUSTOELASTIC EFFECT WITH GUIDED WAVES

The use of guided waves for analyzing acoustoelastic effect has been studied since the 80s. Hirao, Fukuoka and Hori (1981) were the first to study this effect experimentally using Rayleigh waves. As is the case with bulk waves, the results showed non dispersion behavior and a linearity between stress and velocity changes.

The mathematical analysis conducted by Husson (1985) was in good agreement with the above-mentioned author. Furthermore, he showed a good sensitivity of Lamb waves to changes in the medium's stress, also resulting in a linear behavior for acoustoelastic effect. Later, one of the first works on acoustoelasticity with Lamb waves was developed by Delsanto *et al*. (1999).

Most research on acoustoelasticity with guided waves was carried out in the last decade, and the majority used aluminum plate. Besides, only 26% of all papers were about acoustoelasticity.

Figure 4.3 shows the material utilized in papers that studied acoustoelasticity with guided waves.

Figure 4.3 - Materials used in acoustoelasticity with guided waves

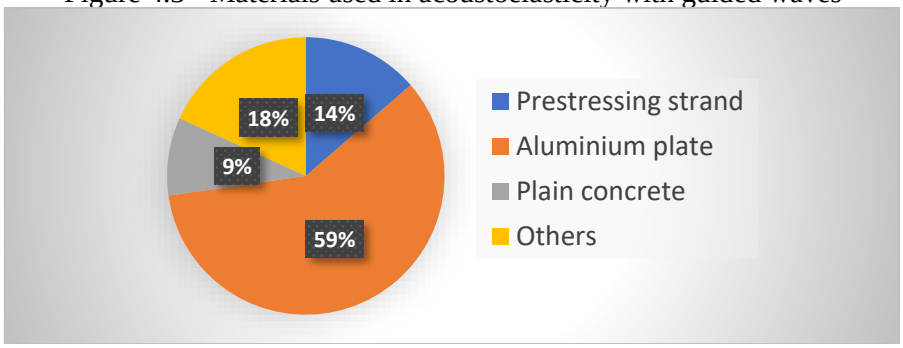

Source: Own elaboration

Most papers, 59%, analyzed Lamb waves in aluminum plates, mainly under tension. In only one case with aluminum (Hughes *et al*., 2018), Rayleigh waves were used.

Although there is a well-known theory about acoustoelasticity with Lamb waves in aluminum, as shown by Gandhi, Michaels and Lee (2012), Dodson and Inman (2014) and Kubrusly, Braga and Weid (2016), there is a great variability in the literature results.

For example, with central frequency around 2 MHz, the maximum velocity variation presented values from 1% to 10%. Nonetheless, in all cases, this variation is linear and negative under tension.

Moreover, Gandhi, Michaels and Lee (2012) demonstrated that the acoustoelastic effect with Lamb waves depends on the frequency and propagation angle, exhibiting a linear behavior.

In contrast, in prestressed strand, Rizzo and Lanza (2002) observed an anomalous response at low tension stress, with an increase of velocity. It might be justified by the settlement of wires at this stress level, which influences the wave propagation due to Lamb wave sensitivity.

In the same line, in rails, Chen and Wilcox (2007) demonstrated that at low frequency-thickness values, the change in phase velocity of guided waves with applied strain is non-linear. While over a frequency-thickness around 1 Hzm, this relation becomes approximately linear. Additionally, these authors also demonstrated that the measurements during loading and unloading produce the same results.

In Figure 4.3, the slice “Others”, 18%, corresponds to 4 papers with different specimens: silicone rubber, steel plate, hollow cross section of aluminum and fiber reinforced composite lamina.

Only one paper, published by Dodson and Inman (2014), investigates the acoustoelastic effect induced thermally.

The best approaches to reinforced concrete as material are the works with prestressing strand and plain concrete, corresponding to 14% and 9%, respectively. The studies with prestressing strand carried out tests in plain strands without the influence of concrete. Those in plain concrete did not use rebars and, consequently, only analyzed bulk waves. Thus, there are no studies about acoustoelasticity with guided waves in rebars of reinforced concrete structures, which is the main objective of the present work.

4.7 SENSITIVITY OF THE GUIDED WAVE MODES TO ACOUSTOELASTIC EFFECT

Considering aluminum as analyzed material, according to Pei and Bond (2016b), the mode S_1 is about ten times more sensitive to acoustoelastic effect than bulk waves, while Pei and Bond (2016a) showed that it occurs with A_1.

Among guided wave modes, there is no agreement on which one has the highest sensitivity. This is due to the dispersive characteristic, which causes the acoustoelastic effect to vary significantly with the considered frequency (Pei and Bond, 2015, 2016a, 2017a). Therefore, there is a specific frequency/thickness combination that results in the highest acoustoelastic constant. Table 4.3 summarizes the conclusion of some authors about the most sensitive mode.

Table 4.3 – Comparison between mode's sensitivity

Authors	Material	Most sensitive mode	Compared to
Shi *et al*. (2023)	Aluminum	S_0	A_0
Li and Shi (2022)	Not defined		
Pei and Bond (2015)	Aluminum	A_0 when the stress' direction is normal to wave propagation S_1 in the other cases	All
Pei and Bond (2016a)		A_1	S_0, S_1 and A_0
Pei and Bond (2017b)	Aluminum	S_1	A_0, A_1 and S_0
Hong-Ye *et al*. (2020)	Fiber reinforced composite lamina	A_0	All

Source: Own elaboration

Thus, although there is no consensus on the most sensitive mode, all the authors agree that the first modes are the most effective for detecting the acoustoelastic effect.

4.8 GUIDED WAVE VELOCITY IN STEEL REBARS

The studies can be classified based on the type of analyses performed. Figure 4.4 exhibits their distribution between numerical (N) and experimental (E) analysis.

Figure 4.4 - Paper distribution by analysis type

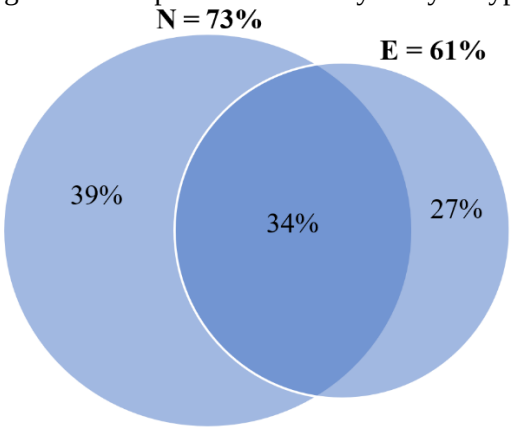

Source: Own elaboration

Most of the authors did numerical analyses, accounting for 73%, while 61% did experimental tests and 34% conducted both. Moreover, the majority conducted only numerical analyses, representing 39%.

An in-depth analysis is conducted on the data of the numerical studies, which yields Figure 4.5.

Figure 4.5 - Characteristics of the numerical studies

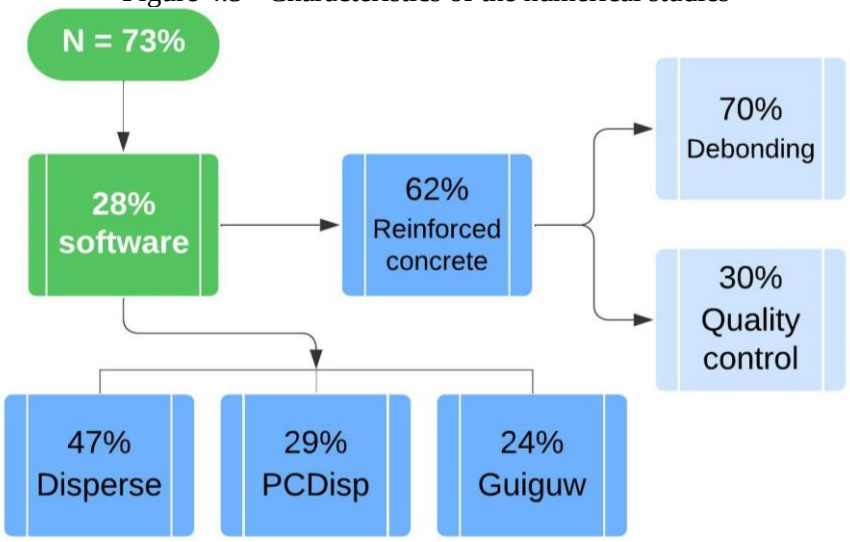

Source: Own elaboration

Among the numerical studies, 28% used software to obtain the dispersion curves and identify the waves by their velocities. 47% of these studies utilized Disperse®, 31% used PCDisp® and 25% used GuiGuw®. Furthermore, 62% of the authors used these software to model reinforced concrete structures, among which 70% analyzed debonding, while the others focused on quality control. Therefore, less than 13% of all papers utilized software to obtain the dispersion curves of rebars embedded in concrete, and none used these curves to analyze acoustoelasticity.

Table 4.4 presents the maximum velocities of guided waves found in the reinforced concrete models. Due to modeling limitations and simplifications, all the authors modeled plain bars.

Table 4.4 - Maximum velocities of guided waves

Authors	**Bar diameter (mm)**	**Frequencies used (kHz)**	**Group velocity (m/s)**	
			Isolated bar	**Embedded bar**
Aseem and Ng (2021)	10	80, 160	5100, 4500	3200
Zima and Kędra (2019)	10	50	5087	3800 (max in the analyzed range), 2500
Zima and Rucka (2018)	10	60	5072	2132
Zima and Rucka (2017)	20	30, 110	5150, 4700	4100, 3000
Zima (2019)	20	40, 50, 60	5030, 4974, 4897	3332, 2852, 2760
Aseem and Ng (2023)	24	0 – 170 (range)	-	3000
Sharma and Mukherjee (2014)	25	54	-	3200

Source: Own elaboration

In the case of embedded rebars, regarding the works with 10 mm bars, a small variation in the frequency applied was sufficient to cause a significant variation in velocity. The frequencies ranged between 50 and 160 kHz, resulting in velocities from 2132 m/s to 3200 m/s. The studies with 20 mm bars utilized frequencies between 30 and 110 kHz, yielding velocities between 2760 m/s and 4100 m/s. For 24 mm and 25 mm, within the range of 0 – 170 kHz, the velocity was approximately 3000 m/s. This variability and the complex relationship between diameter, frequency and velocity reflect the strong dispersion nature of guided waves.

The velocities in isolated bars presented less variability than those in embedded bars, with values around 5100 m/s. This occurs because, for the same frequency range, there are much more modes and consequently velocity possibilities in the embedded case, as shown in Figure 4.6. The curves in blue, labeled with the subscript “b”, are related to isolated bars. All curves correspond to bars with a diameter of 10 mm and depict longitudinal modes.

Figure 4.6 - Group velocity in rebars of 10 mm

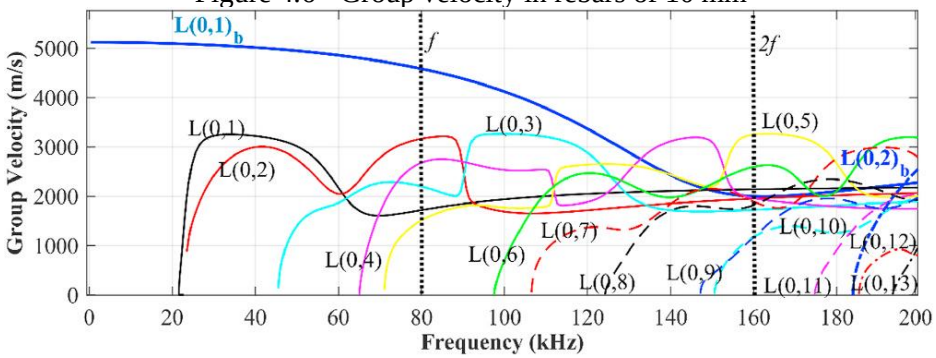

Source: Aseem and Ng (2021)

Within the range considered above, 0 – 170 kHz, basically there is only the $L(0,1)_b$ mode for isolated bar, which exhibits minimal variation with frequency. At low frequencies, up to approximately 60 kHz, the velocity is almost constant, around 5000 m/s. Conversely, there are 10 modes for the embedded case with much higher variability. This behavior is similar for bars with other diameters.

4.9 ADVANTAGES OF LONGITUDINAL GUIDED WAVES FOR STRUCTURAL ANALYSIS

The analyses with software focus on longitudinal guided waves, 76% of them, due to their advantages compared to flexural and torsional modes. According to Zima and Rucka (2018), longitudinal waves have high sensitivity to damage detection, such as debonding, and to discontinuities in stress and displacements at the interface between concrete and rebar. Farhidzadeh and Salamone (2015) and Sharma *et al*. (2021) primarily justified their use because of the low attenuation exhibited during propagation.

Sharma and Mukherjee (2014) demonstrated that compared to higher modes, the fundamental mode L(0,1) at 1 MHz is more sensitive to changes at concrete-steel interface. While Sun and Zhu (2020) emphasized that the high order longitudinal mode L(0,8) has the lowest attenuation and highest energy velocity at high frequency, over 1.3 MHz.

A different conclusion was obtained by Aseem and Ng (2023), whose study showed that torsional modes outperformed longitudinal modes for debonding detection, attributed to their larger amplitude.

4.10 HIGHLIGHTS OF CHAPTER 4

An abstract of the chapter is listed here:

a) In most papers, when the guide has a circular cross section, the authors only use the designation “guided waves”, and Lamb waves exclusively for plates;
b) Yamakawa and Murakami (1997) concluded that the influence of stirrups was negligible on the behavior of elastic waves in reinforced concrete, mainly because of their volume relative to the longitudinal rebars;
c) When guided waves were used in a finite medium, the acoustoelastic effect presented dispersion and linear behavior. Besides, with Lamb waves in aluminum plate, the curve is negative under tension.

d) In prestressed strand, Rizzo and Lanza (2002) observed an anomalous response at low tension stress, with an increase of velocity. It might be justified by the settlement of wires at this stress level;
e) In rails, Chen and Wilcox (2007) demonstrated that at low frequency-thickness values, the acoustoelastic curve is non-linear;
f) There are no studies about acoustoelasticity with guided waves in rebars of reinforced concrete structures;
g) Considering aluminum as analyzed material, the modes S_1 and A_1 are about ten times more sensitive to acoustoelastic effect than bulk waves. Among guided wave modes, although there is no consensus on the most sensitive one, all the authors agree that the first modes are the most sensitive.
h) In embedded rebars, a small variation in the applied frequency was sufficient to cause a significant variation in velocity. With frequencies within the range of 0 – 170 kHz, the velocities varied from 2132 m/s to 4100 m/s, while in isolated bars, there was less variability, with values around 5100 m/s.
i) According to most authors, among guided waves, the longitudinal modes have the highest sensitivity to damage detection and to discontinuities in stress and displacements, low attenuation and the highest velocity.

5 EXPERIMENTAL PROGRAM

Experiments were performed on isolated bars under tension and on reinforced concrete prisms under compression and bending. All prisms were initially tested under compression and subsequently under bending. Furthermore, the analyses in prisms under bending were restricted to the rebars under tension.

During the experiments, for each load step, 3 ultrasound indirect measurements were taken directly on the rebars. Figure 5.1 illustrates the ultrasound application directly on a rebar of a prism, which was possible by openings on the prisms' surface ensured during casting.

Figure 5.1 - Draft of ultrasound application

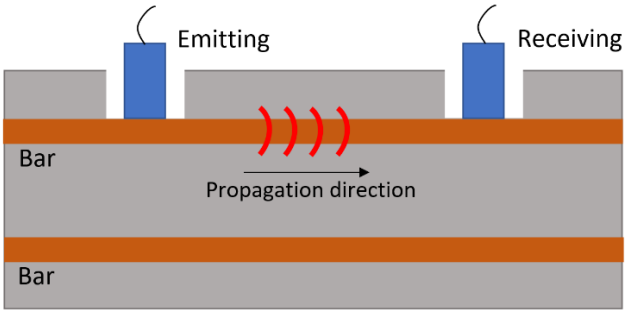

Source: Own elaboration

Moreover, pilot experiments were conducted with rebar diameter of 20 mm, while final experiments used diameters of 8, 10, 12.5 and 16 mm.

5.1 MATERIALS

Table 5.1 presents the concrete mix designs for the pilot test specimens (20 mm), designated as Mixture 1, and for the specimens with other bar diameters, designated as Mixture 2. In Mixture 2, a water-reducing additive, Adva Cast 585, was used, with its dosage expressed as a percentage of the cement mass.

Table 5.1 - Concrete mixtures

	Mixture 1	**Mixture 2**
Portland cement (kg/m^3)	403.6	408.5
Fine sand (kg/m^3)	313.2	317.0
Medium-size sand (kg/m^3)	469.8	475.5
Coarse aggregate (kg/m^3)	1053.4	1066.3
Water (kg/m^3)	189.7	179.8
Water/Cement	0.47	0.44
Additive (%)	0	0.3
Slump test (cm)	5	18
f_{cm} (MPa)	35.1	43.8
f_{ck} (MPa)	28.5	37.2

Source: Own elaboration

The Slump test was performed based on the standard ABNT NBR 16889:2020. The parameter f_{ck} is the normative compression strength measured 28 days after casting, obtained by the average of the compression strength f_{cm}, and calculated according to ABNT NBR 12655:2022, considering a standard deviation of 4 MPa. For Mixture 1, 5 cylindrical specimens were cast with a height of 20 cm and a diameter of 10 cm; for Mixture 2, 6 samples were cast.

The Portland cement used was CPII Z 32, which contains addition of pozzolanic material, between 6% and 14%, and has a strength class of 32 MPa, as specified in ABNT NBR 16697:2018. Both sands used were quartz sands, whose only difference lies in particle diameter. The coarse aggregate was basaltic. Table 5.2 shows the specific mass of the materials.

Table 5.2 - Specific mass of materials

	Specific mass (kg/dm^3)
Portland cement	3.05
Fine sand	2.59
Medium-size sand	2.56
Coarse aggregate	2.82

Source: Own elaboration

The aggregates were submitted to characterization tests in accordance with ABNT NBR 7211:2022, whose sieve test results are presented in Appendix B. Figure 5.2 shows

the grain size distribution: the sands on the left and the coarse aggregates on the right. Table 5.3 presents the corresponding characterization parameters.

Figure 5.2 - Aggregates size distribution: sand (a) and coarse aggregates (b)

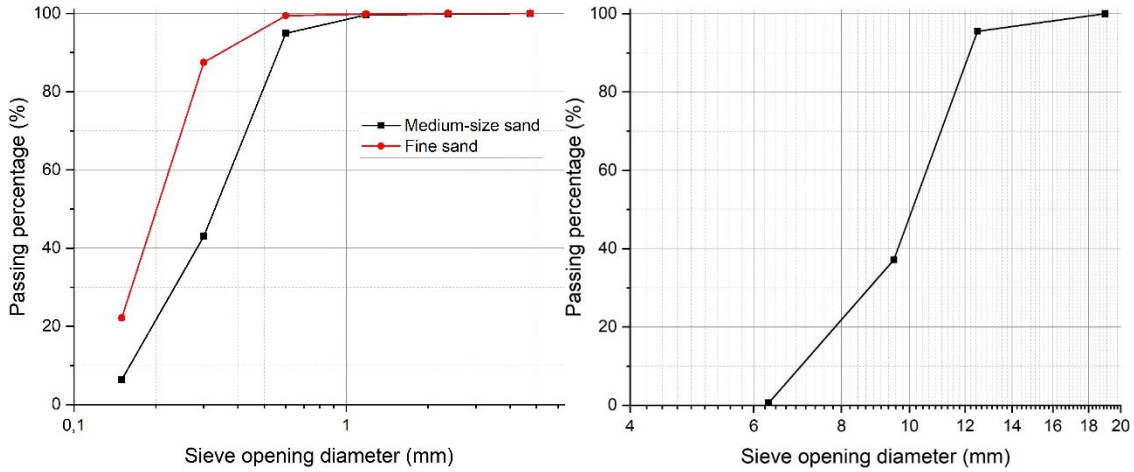

Source: Own elaboration

Table 5.3 - Aggregates characterization parameters

Aggregate	Maximum grain size (mm)	Fineness modulus
Fine sand	0.6	0.9
Medium-size sand	0.6	1.6
Coarse aggregate	12.5	6.6

Source: Own elaboration

The flexural reinforcements consisted of steel CA-50, specified by ABNT NBR 7480:2024, and the stirrups consisted of 5 mm CA-60. The 20 mm rebars were submitted to 3 tension tests for characterization, whose results are shown in Figure 5.3. The corresponding curve of Bar 1 is under the curve of Bar 2. Thus, the average value for Young modulus is $E = 192{,}02$ GPa, with coefficient of variation of 3.2%. This modulus, considered for all diameters, and the strain gauge values were used to obtain the acoustoelastic curves.

Figure 5.3 - Stress Strain curves of 20 mm rebar

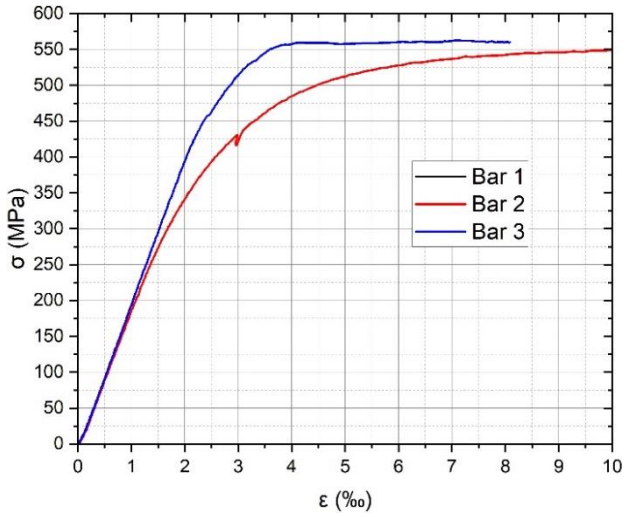

Source: Own elaboration

5.2 ULTRASOUND EQUIPMENT

For the tests, the Pundit Lab+ model ultrasound device, produced by Proceq® (see Figure 5.4) and the Pundlink® software version 2.4, specific for this equipment, were used.

Figure 5.4 - Ultrasound equipment

Source: Own elaboration

In this software, there are two main input data, “Amplitude” and “Rx probe gain”. The first is related to a voltage that determines the emitting wave energy, while the second parameter is the signal gain, a signal amplifier provided by the receiving transducer, given as a multiplier. After calibrating these parameters, as recommended by Vasconcelos (2022) and Vasconcelos and Haach (2024), it was achieved 250V and 10x, respectively.

In all tests, 250 kHz longitudinal transducers with flat contact surface were used. Before carrying out any test, the device is calibrated by applying these transducers to the ends of a cylindrical prism whose wave travel time is known, 25.4 μs (see Figure 5.5).

Figure 5.5 - Transducers and calibration sample

Source: Own elaboration

For the contact between transducers and prism, a water-base gel was used. As recommended by Vasconcelos and Haach (2024), to ensure good contact and, consequently, a higher velocity, it is necessary to wait for complete saturation of the surface pores before performing measurements. This was achieved by applying pressure and waiting for some time, approximately 1 minute, before conducting the ultrasound tests.

5.3 PRISMS DESIGN

15 Prisms with dimensions of 15x15x50 cm^3 were produced, each one reinforced with 4 bars and concrete cover of 2.5 cm. Furthermore, 2 plain concrete prisms were produced with Mixture 2, solely to obtain the longitudinal bulk wave velocity in concrete. The characteristics of the prisms are presented in Table 5.4.

Table 5.4 - Prisms' features

Prism	Bar diameter (mm)	Number of Stirrups	Distance between Stirrups (cm)	Concrete Mix
1	8	8	7	2
2				
3				
4	10			
5				
6				
7	12.5	8	7	
8		4	15	
9		8	7	
10	16	8	7	
11		4	15	
12		8	7	
13	20	2	45	1
14				
15				

Source: Own elaboration

The stirrups were designed based on ABNT NBR 6118:2024 considering the prisms both as column and beam. The stirrup spacing was limited to 7 cm due to the diameter of the openings on prism surface, for free access to longitudinal reinforcement by the transducers. An exception was made for prisms 8 and 11, where half the number of stirrups was used to analyze their influence on the results. Nevertheless, no influence of the stirrup variation was observed, and therefore, its analysis is not presented in the results. A further exception was made for prisms 13 to 15, where stirrups were placed only at both ends.

To guarantee direct access to longitudinal bar surface after casting, cylindrical polystyrene was used, with 30 cm between their axes on the same bar, as shown in Figure 5.6. From left to right, it shows the positioning of the polystyrene, the openings after casting and a detail of one opening with part of a bar surface exposed, which is necessary for better signal quality. The openings were not perfectly symmetrical on the surface, as their location depended on the stirrup distribution.

Figure 5.6 - Prisms' opening configuration

Source: Own elaboration

In all prisms, 1 strain gauge was fixed by a black vinyl electrical tape centered on each longitudinal bar. The gauges, produced by Excel®, are the type PA-06-250BA-120-L, lot 220718, with a factor F.S. of 2.8. Figure 5.7 shows the positioning of the strain gauges.

Figure 5.7 - Strain gauge positioning

Source: Own elaboration

For the strain gauges, it was used the data acquisition system DiDaq-B2, version 2.6.24.10.05.2022.NC.

5.4 TEST SETUP

The ultrasound tests were performed during compression, flexural, and tension tests. These tests were conducted in load steps, and for each step, 3 continuous indirect

ultrasound measurements were performed. To ensure a 30 cm distance between the transducer axes and approximately constant pressure, they were fixed with rubber bands.

The experimental setup for the prisms was based on the initial hypothesis that the surrounding concrete would not influence the acoustoelastic effect in the bar.

5.4.1 Tension in isolated rebars

For the tension tests on isolated rebars, 4 specimens of each diameter were used, and these rebars were distinct from those used in the prisms. Due to the high number of curves of isolated rebars, solely to improve the clarity of the graphs in the Results section, the specimens were separated into Test 1 and Test 2, with the exception of the 20 mm diameter.

The samples were fixed at the ends, and the transducers were attached to their center. Moreover, an Instron machine was used, where the bars were subjected to their respective yield strength, but before yielding. Due to the machine's limitations, the samples measured 1.2 m in length (see Figure 5.8). No preloading cycle was applied in this case.

Figure 5.8 - Tension test

Source: Own elaboration

5.4.2 Compression in prisms

In compression, 20 preloading cycles were applied only once to each prism using a centered force. Because only one pair of transducers was used, each prism was subjected to a complete experiment for each rebar, following the sequence of the rebar numbering (see Figure 5.9).

Figure 5.9 – Sequence of compression application

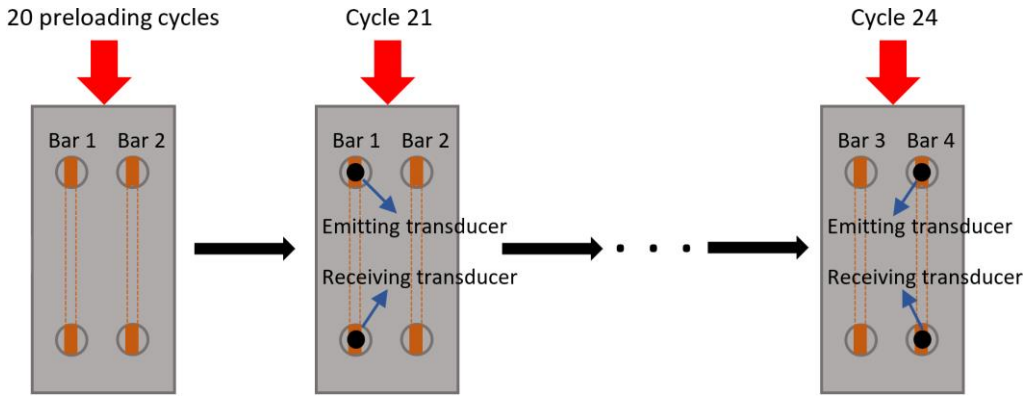

Source: Own elaboration

The tests were performed in a steel frame, where a manual hydraulic jack was attached. To uniform the stress on the prisms' top face, a steel plate with 5 cm in thickness was utilized (see Figure 5.10), while the other end was simply supported on the ground. Furthermore, small eccentricities were imposed on the load application to ensure higher stress in the analyzed rebar. This decision was based on the initial hypothesis that it would be possible to isolate the acoustoelastic effect in the bar from the influence of the surrounding concrete.

Figure 5.10 - Compression test

Source: Own elaboration

5.4.3 Bending in prisms

After being subjected to the compression tests, the same prisms were used for the flexural tests. Before the flexural testing, 20 preloading cycles were applied. The sequence of the experimental procedure is shown in Figure 5.11.

Figure 5.11 - Bending test sequence

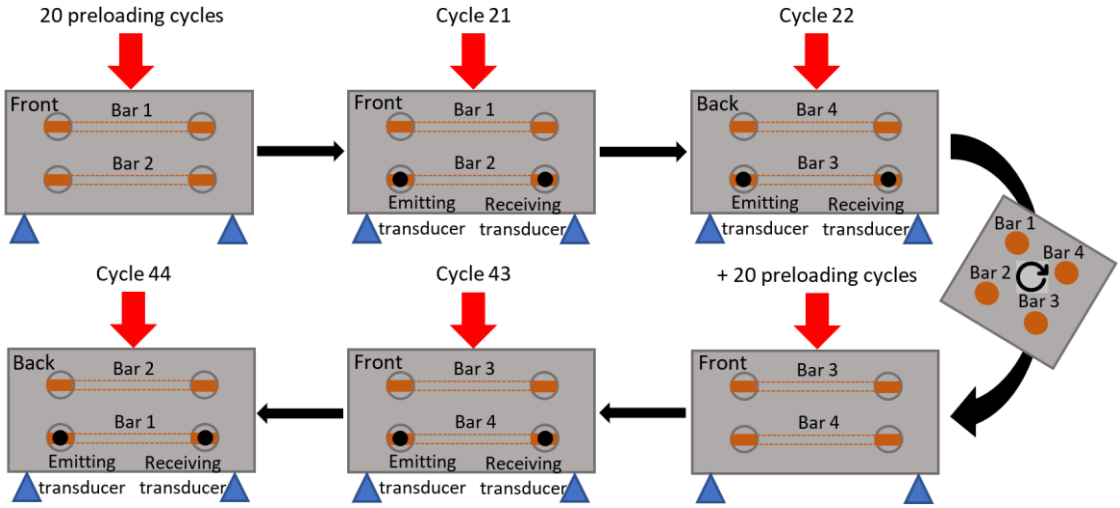

Source: Own elaboration

A three-point support was used, in the same load application structure shown previously, as presented in Figure 5.12. In addition, the load was applied at the middle of span, which was 45 cm, and all supports could be considered hinges.

Figure 5.12. Bending test

Source: Own elaboration

5.4.4 Loading in the experiments

Table 5.5 presents the loads applied, including the Ultimate Test Load, UTL, which is the maximum value applied during the test, and its comparison with the Ultimate Load, which is related to the design load. Before testing, the preloading cycles had UTL as maximum load, to simulate the in-service conditions. During loading, if the strain in any bar reached 1.2‰, which is 60% of ε_{yd}, the experiment cycle ended.

Table 5.5 - Load characteristics

Specimen	Test	Bar diameter (mm)	UTL (kN)	UTL/UL (%)	Increment load (kN)	Number of steps
Isolated bars	Tension	8	25	100	1.25	20
		10	40	100	2	
		12.5	60	100	3	
		16	100	100	5	
		20	150	96	7.5	
Prisms 1 to 15	Compression	8	480	58	24	21
		10	500	58	25	
		12.5	520	58	26	
		16	560	58	28	
		20	620	59	31	
Prisms 1 to 12	Flexural	8	40	91	2	
		10	60	90	3	
		12.5	80	82	4	
		16	100	70	5	

Source: Own elaboration

The UL for isolated rebars was considered to be the yield load. As a result, all samples reached yield.

In compression, UL was obtained by considering a uniform compression stress on a compound cross section, disregarding the openings and eccentricities. For this, ABNT NBR 6118:2024 was used with the compression strength of Mixture 1, shown in Table

5.1. Due to the eccentricity of the applied force, the ratio UTL/UL around 60% ensured the strain in the bar around 60% of ε_{yd}.

In bending, UL is related to the resisting bending moment obtained by the design of a beam based on ABNT NBR 6118:2024, using Mixture 1 of Table 5.1. In some cases, the flexural tests stopped when the cracks became visible, which generally occurred before UTL. An exception was made for prisms 13, 14, and 15, as they were not initially designed for bending. Their flexural load steps did not follow a standard procedure, and the stopping criterion was strictly based on the cracking evolution observed by the operator. This is the reason why there is no information on their flexural tests in Table 5.5.

Finally, UTL/UL for 16 mm was 70% due to the loading capacity of the flexural supports. Moreover, some prisms with 16 mm and all prisms with 20 mm failed during preloading. As a result, their results are not included in this study. This failure probably occurred due to the insufficient anchoring length of the longitudinal bars, which must be much bigger than the available space after the supports.

6 PRELIMINARY RESULTS: TYPES OF WAVES ON WAVE PROFILE

In general, studies on concrete structures focus on bulk waves. In this context, these waves can be easily identified on the generated profiles, where the arrival of longitudinal and shear waves are determined, as well as coda waves. Figure 6.1 exhibits a typical profile in a mortar sample.

Figure 6.1 - Identification of waves on profile

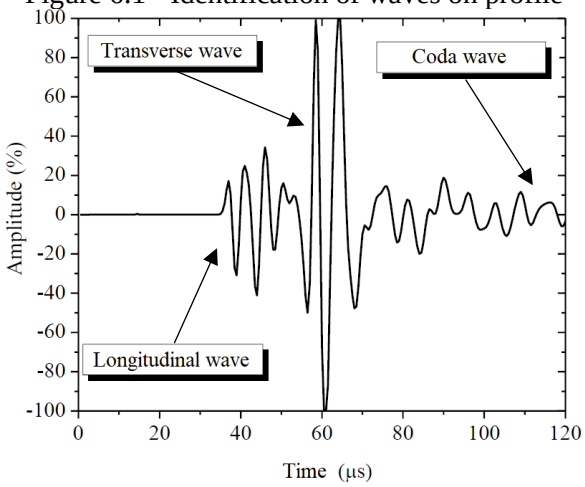

Source: adapted from Fernandes Neto (2023)

In reinforced concrete structures, beyond bulk waves, the ultrasonic pulse generates guided waves in the rebars. Due to the dispersive characteristic of guided waves, their velocity, and consequently arrival times, are initially not known. Thus, before the acoustoelastic analysis, the arrival times of the different waves produced in the analyzed prisms and isolated rebars are determined, both in a stress-free state.

6.1 THE FASTEST WAVE IN ISOLATED REBARS

The first analysis was conducted with isolated bars subjected to tension. A typical wave profile is shown in Figure 6.2.

Figure 6.2 - Typical wave profile in isolated bars

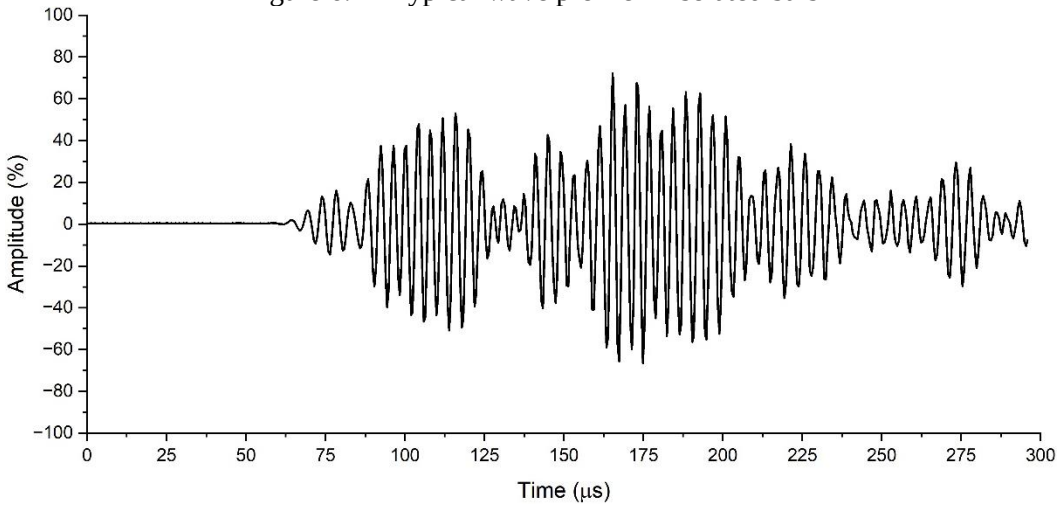

Source: Own elaboration

Table 6.1 shows the wavefront velocities for each diameter. The specimens with 20 mm are not analyzed because, in almost all profiles, the fastest guided waves could not be detected by the receiver transducer. The tests were conducted in two instants, named Test 1 and Test 2.

Table 6.1 - Wavefront velocity in isolated rebars

		Test 1	Test 2
	Bar	**v (m/s)**	
8 mm	**1**	4700	4700
	2	4623	4700
10 mm	**1**	4780	4700
	2	4623	4476
12,5 mm	**1**	5036	4862
	2	4862	4700
16 mm	**1**	4700	4700
	2	4947	4548
	Average	**4784**	**4673**
	Standard deviation (m/s)	**142**	**108**
	CV (%)	**3.0**	**2.3**
	Global average	**4729**	
	Global standard deviation (m/s)	**138**	
	CV (%)	**2.9**	

Source: Own elaboration

The average wave velocity is 4729 m/s, with a standard deviation of 138 m/s. The maximum value occurred with 12,5 mm, 5036 m/s, and the lowest one occurred with 10 mm, 4476 m/s. This variation can be justified by the little movement of the transducers during the testing, which occurred due to the difficulty in fixing them; the inaccuracy of their placement on the bar surface; and the different contact point due to the bar surface deformation.

The results present CV smaller than 3%, which might indicate low variability, what, for a first analysis, could indicate a non-dispersive wave. As explained in previous chapters, this velocity is much lower than that of longitudinal bulk wave, which is around 5900 m/s.

Disregarding the Poisson effect and considering Young modulus of 210 GPa, the velocity is 5200 m/s, which is much higher than all values in Table 6.1 and even 10% higher than the average. As it is a simplification, the real longitudinal bulk wave velocity is between 5200 m/s and 5900 m/s; the bigger the diameter, the closer the velocity to the

second value. Thus, the fastest wave detected is not a longitudinal bulk wave and has a lower velocity.

Table 6.2 shows the main frequency in the analysis window for each diameter, which begins with the wavefront arrival. This frequency is obtained through Fourier transform of the signal. Figure 6.3 presents the frequency spectrum of an 8 mm rebar.

Table 6.2 - Central frequency in time window

Diameter (mm)	**Frequency (kHz)**
8	243.90
10	195.12
12.5	146.34
16	97.56

Source: Own elaboration

Figure 6.3 - Frequency spectrum of 8 mm rebar

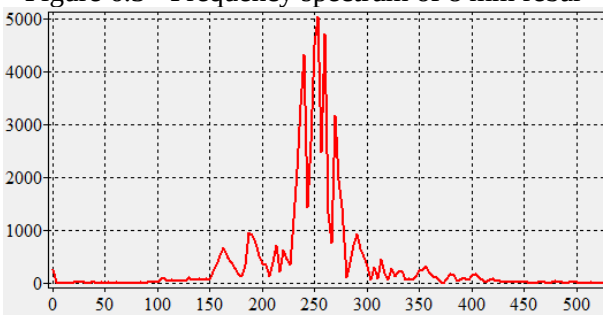

Source: Own elaboration

Therefore, the higher the diameter the lower the central frequency, which indicates a dispersive behavior, such as in Lamb waves.

The guided wave software were used to obtain the highest velocity for each diameter. The input parameters are shown in Table 6.3.

Table 6.3 - Input parameter for guided wave software

Longitudinal velocity (m/s)	5200
Shear velocity (m/s)	3190
Density (kg/m^3)	7850
Poisson	0.29

Source: Own elaboration

At first, it is analyzed the dispersion curves using the software GUIGUW®. Figure 6.4 presents the dispersion curves for phase and group velocity for all bar diameters.

Figure 6.4 - Dispersion curves of isolated rebars

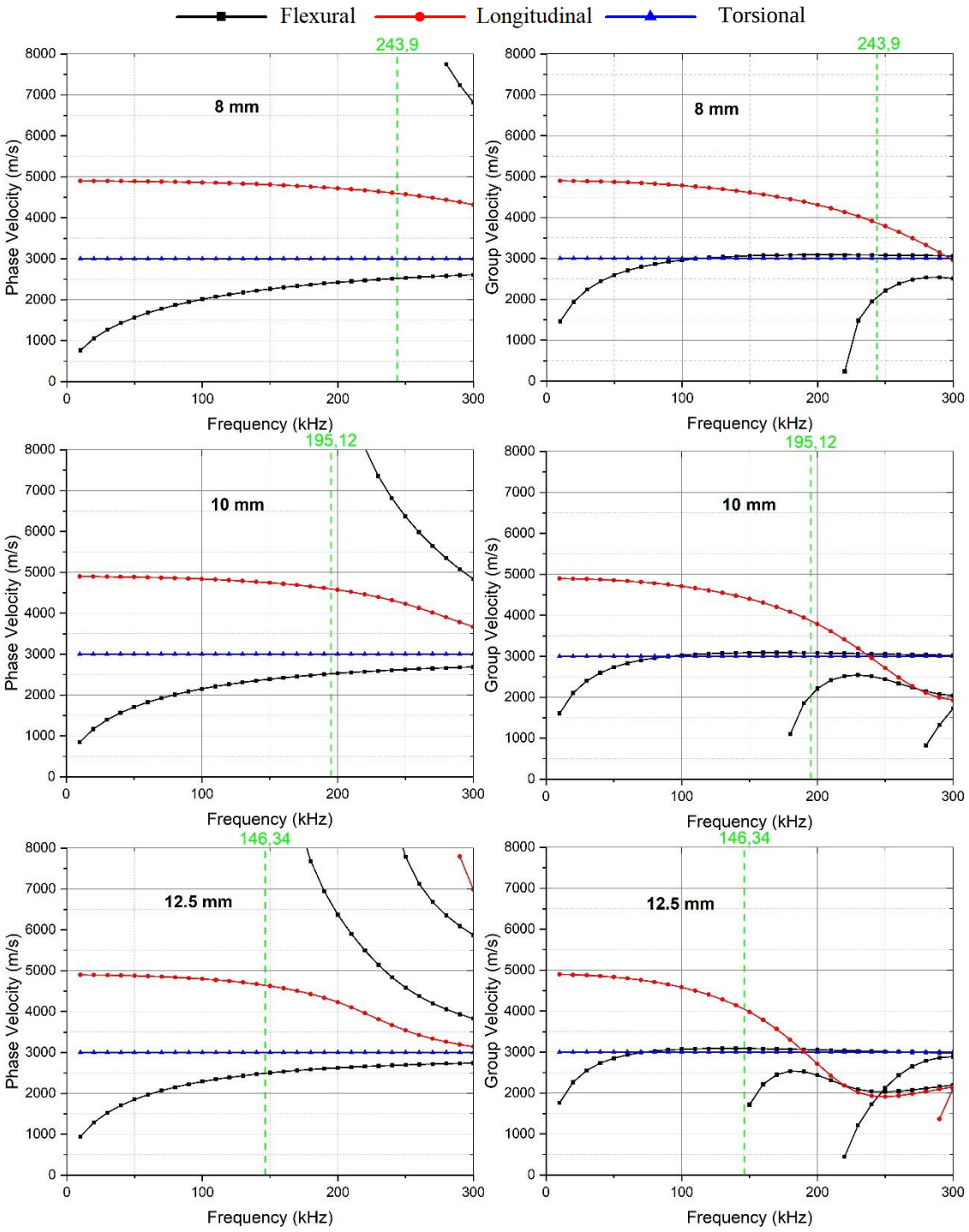

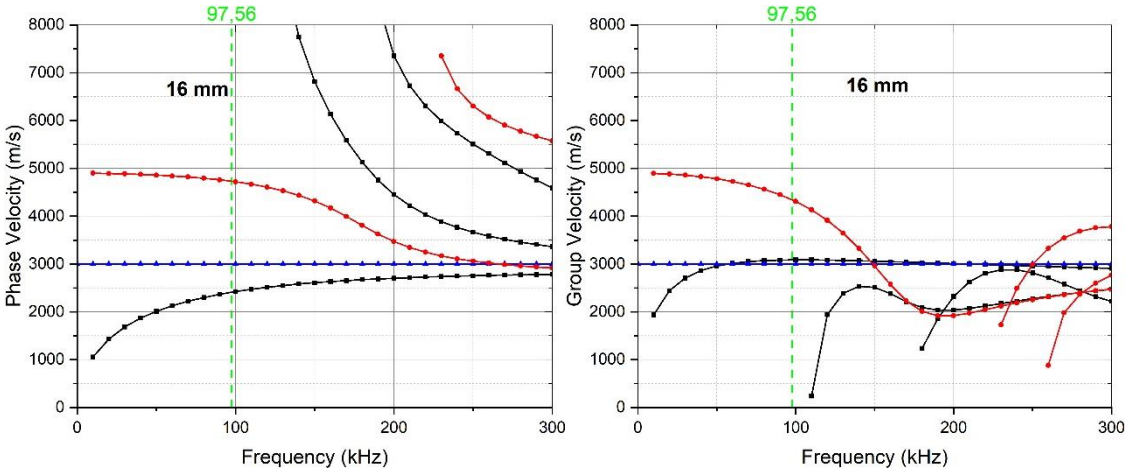

Source: Own elaboration

Only the first modes of each kind of wave are captured in the respective frequency, which are L(0,1), longitudinal, F(1,1), flexural, and T(0,1), torsional. Additionally, the higher the frequency analyzed or the bar diameter, the more wave modes appear in the same frequency range.

Since the maximum velocity is related to the first longitudinal mode for both phase and group velocities, the analyses below just consider group velocity and L(0,1) mode.

Figure 6.5 shows the dispersion curves of L(0,1) obtained by the software GUIGUW®, the MATLAB code called PCDisp® and the code developed in Python in the present work based on Zemanek (1972).

Figure 6.5 - Dispersion curves of L(0,1)

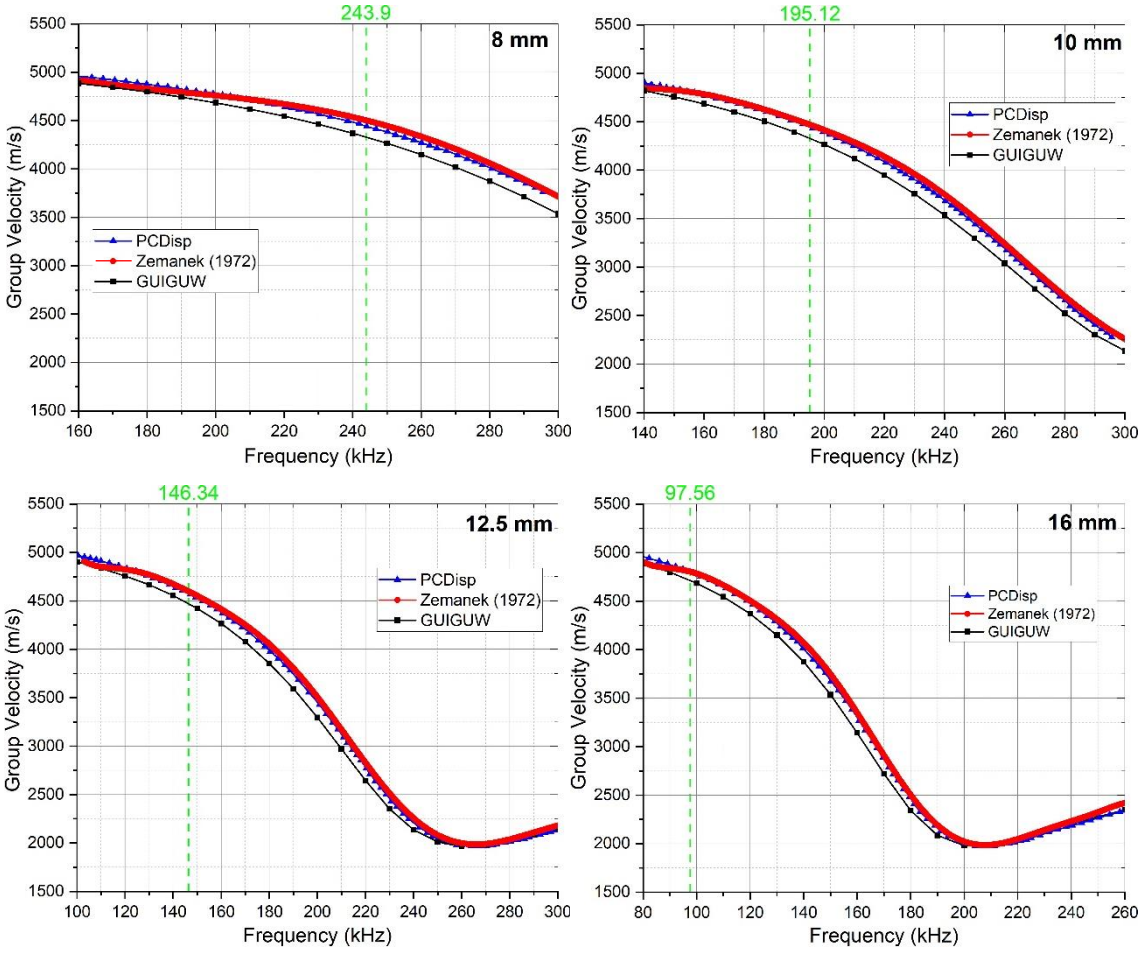

Source: Own elaboration

All curves present close results, mainly PCDisp and Zemanek (1972), which are almost overlapped. The curves by GUIGUW® present the lowest value for all diameters, despite the minimal difference.

Table 6.4 presents the velocity values at the respective frequency of each case above.

Table 6.4 - Wavefront velocity by each software

Software	8 mm	10 mm	12.5 mm	16 mm	CV (%)
GUIGUW	4334	4334	4471	4712	**3.5**
PCDisp	4440	4446	4576	4803	**3.2**
Zemanek (1972)	4504	4475	4605	4807	**2.8**
Average	**4426**	**4418**	**4551**	**4774**	
CV	**1.6**	**1.4**	**1.3**	**0.9**	

Source: Own elaboration

As consequence of the similar behavior between the curves in Figure 6.5, the obtained velocities in Table 6.4 have close values, with CVs smaller than 2%.

Figure 6.4 shows that as the diameter increases, the curves tend to the left, which reduces the velocity considering the same frequency. Although, Table 6.2 shows that the central frequency decreases as the diameter increases, which, according to Figure 6.4, yields velocity increase. Thus, these opposite phenomena in terms of velocity variation yield low variability in Table 6.4 considering the same software, with CVs lower than 4%.

It can also be visualized when the dispersion curves are plotted in terms of the product frequency x diameter (FD), as exhibited in Figure 6.6, where there are the results using PCDisp.

Figure 6.6 - Dispersion curves for frequency x diameter

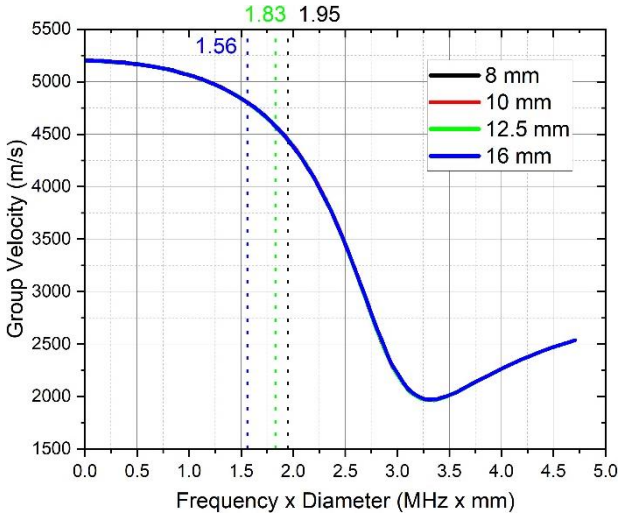

Source: Own elaboration

All the acoustoelastic curves coincide. Thus, for the same material, there is only one dispersion curve, and the guided wave velocity depends solely on the product of frequency and thickness.

For the case of 8 mm and 10 mm rebars, the FDs are the same. As the FD for 12.5 mm is close to the above, the corresponding velocity is also close. Conversely, the FD for 16 mm decreases more significantly compared to 8 mm and 10 mm, resulting in the highest velocity. These conclusions are confirmed in Table 6.4.

Finally, considering the values of Zemanek (1972), minimum of 4475 m/s and maximum of 4807 m/s, the difference between these values and the experimental average velocity on Table 6.1, 4729 m/s, is 5% and 2%, respectively. This difference may be due to the deformation on the bar's surface, as the models and formulations are related to perfect rod bars with smooth surface.

Therefore, as it is observed a dispersion behavior in terms of wave frequency and the experimental wave velocity is very close to that of the first mode of the longitudinal guided wave, it is concluded that the fastest wave in the present work is the fundamental mode of longitudinal guided wave. From now on, in isolated rebars, the first experimental wave captured by the transducer is considered to be L(0,1).

6.2 THE FASTEST WAVE IN PRISMS

A typical wave profile in prisms is exhibited in Figure 6.7.

Figure 6.7 - Typical wave profile in prisms

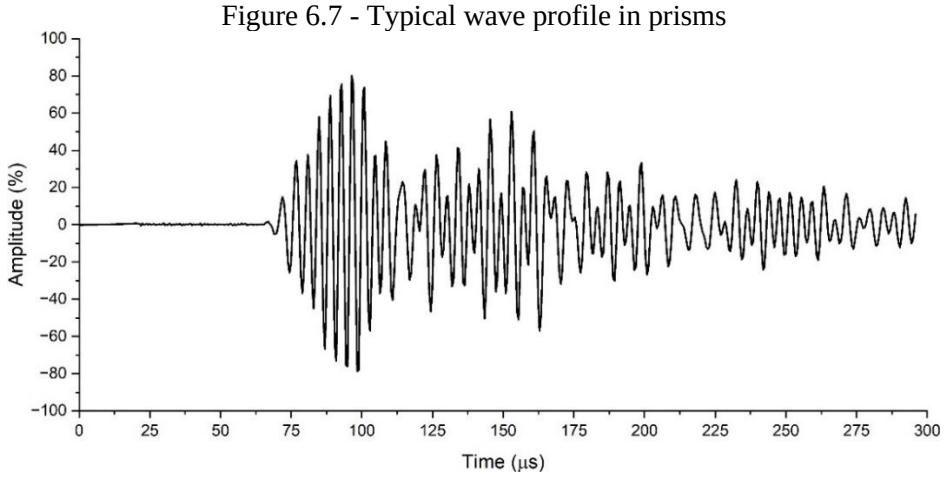

Source: Own elaboration

In Appendix A, the wave velocities in the prisms are shown. In this appendix, the velocities not presented are due to failure of the respective prism before the experiment finishes. Based on these values, Table 6.5 presents the respective averages.

Table 6.5 - Statistical parameters of wave propagation by diameter

Diameter (mm)	Average (m/s)	Variance	Standard deviation (m/s)
Compression			
8	4552	17483	132
10	4469	21889	148
12.5	4207	71902	268
16	3973	107172	327
Bending			
8	4534	4972	71
10	4551	25734	160
12.5	4476	21655	147

Source: Own elaboration

The velocity tends to decrease as the bar diameter increases. As it will be shown later, larger diameters make it more challenging for the receiving transducer to detect the fastest guided wave. As the diameter increases, the rebar stiffness also increases, requiring more energy to move the rebar for detection by the receiving transducer. Thus, the first detected wave arrives later on wave profile.

Conversely, the smaller the diameter, the lower the variance, what makes the results with 8 mm to present the smallest standard deviation and with 16 mm, the highest one. It might be explained by the random nature of the cracking phenomenon, which is more prevalent in 16 mm rebars. Considering the results with the lowest standard deviation, the wave velocity tends to a value around 4500 m/s, which will be used as a reference for the experimental results.

To obtain a reference longitudinal bulk wave velocity for the concrete, some experiments were carried out on plain concrete prisms, shown in Table 6.6. This concrete has the same mixture as the other reinforced concrete prisms. In total, 9 results were obtained by direct measurements in the direction of the largest dimension, 50 cm. Thus,

the average velocity is 4549 m/s, which is very close to the results in reinforced concrete and is around their upper limit.

Table 6.6 - Velocities in plain concrete prisms

Measurement	**Velocity (m/s)**
1	4544
2	4563
3	4578
4	4494
5	4528
6	4540
7	4525
8	4586
9	4581
Average (m/s)	**4549**
Variance	**842**
Standard deviation (m/s)	**29**

Source: Own elaboration

In the previous analysis, the software PCDisp and the Zemanek (1972) code presented the best agreement with the experimental results. Between them, it is only possible to model reinforced concrete with PCDisp, thus this software is used to obtain the dispersion curves. Besides, as the longitudinal modes present the highest group velocities, what also occurs in bars embedded in concrete, the following analyses are limited to the dispersion curves of this mode.

The wave frequency for both bending and compression testing is presented in Table 6.7. Unlike the isolated bar case, the frequencies vary in a range among prisms.

Table 6.7 - Frequency range for each diameter

Diameter (mm)	Frequency range (kHz)
8	243.90 – 195.12
10	
12.5	195.12 – 146.34
16	

Source: Own elaboration

For the modeling in PCDisp, the materials parameters presented in Table 6.8 are considered. In this case, the inner radius is always the bar diameter, and the outer radius is that value plus the concrete cover.

Table 6.8 - Materials parameters

	Steel	Concrete
Longitudinal bulk wave velocity (m/s)	5200	4549
Density (kg/m^3)	7850	2400
Poisson	0.29	0.2

Source: Own elaboration

Figure 6.8 shows the graphs generated by PCDisp for the 8 mm rebar. These are typical longitudinal wave dispersion curves of a bar surrounded by a 3 cm concrete cover. The velocity tends to the upper limit as the frequency approaches zero, assuming the value of the longitudinal bulk wave velocity in concrete, which is 4549 m/s in this case. This value always occurs in L(0,1) mode, while the other modes have their local maximum value, slightly smaller than that.

Figure 6.8 - Dispersion curves of group velocity of 8 mm

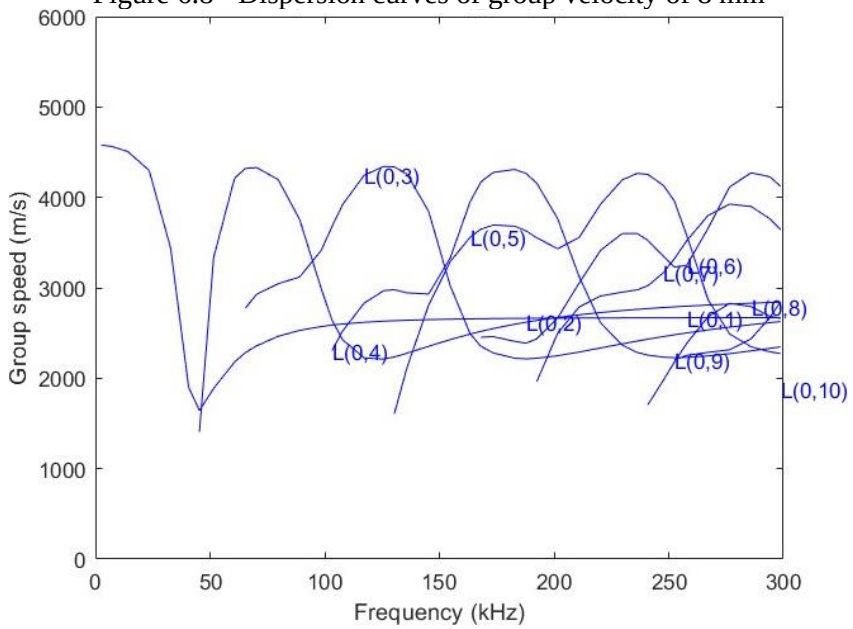

Source: Own elaboration

For each diameter, the maximum local velocity is obtained in the respective frequency range shown in Table 6.7. Figure 6.9 shows the fastest waves.

Figure 6.9 - Maximum wave velocity in prisms

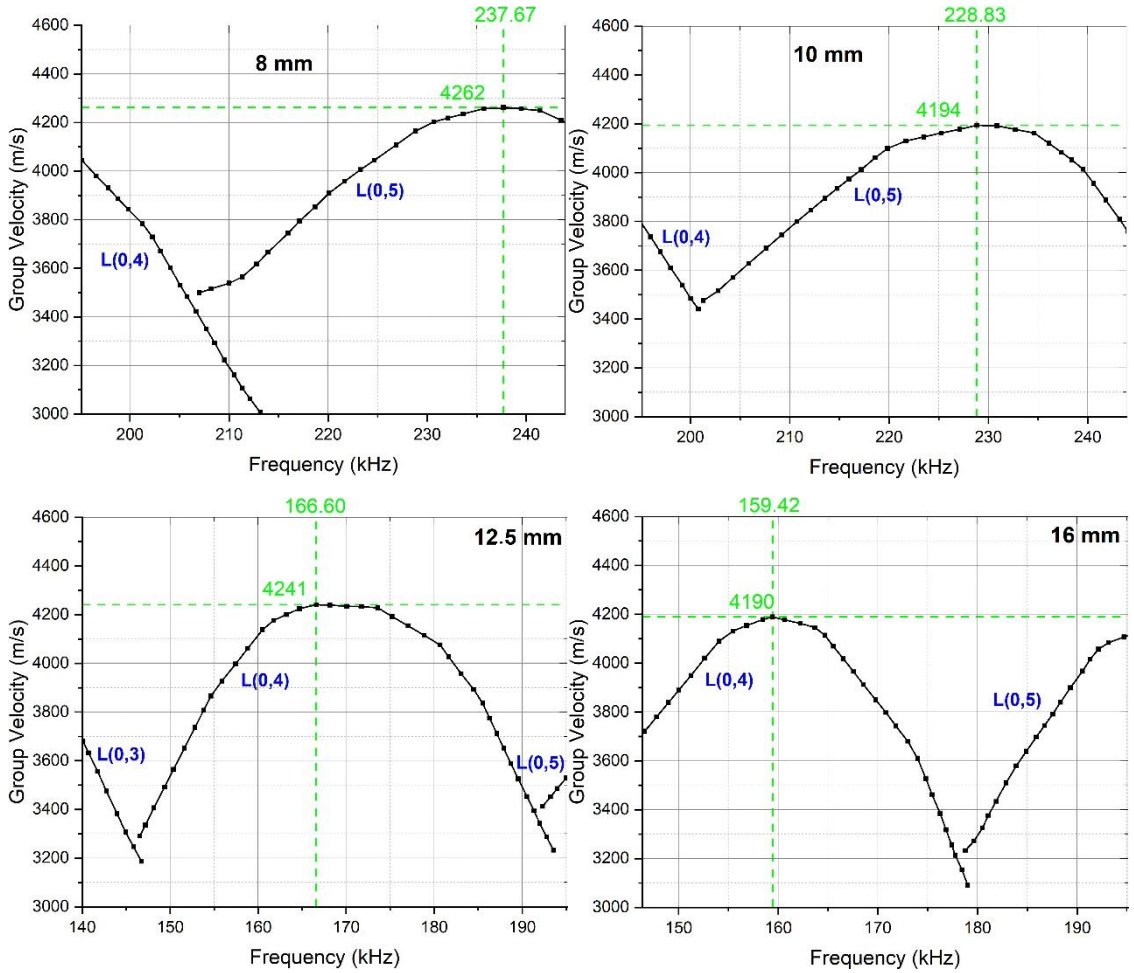

Source: Own elaboration

All velocities are very close to each other, indicating a constant behavior, with a minimum of 4190 m/s for 16 mm and a maximum of 4262 m/s for 8 mm. The maximum values occurs in L(0,5) for 8 mm and 10 mm, and L(0,4) for 12.5 mm and 16 mm.

Therefore, the theoretical average maximum velocity is 4222 m/s, which is 6 % smaller than the experimental velocity, considered 4500 m/s. In the case of reinforced concrete prims, it is also possible to consider longitudinal guided waves as the first wave detected in the receiving transducer. From now on, only this kind of wave will be considered in the analyses.

Some considerations and simplifications may justify the differences between theoretical and experimental values:

1. PCDisp models the reinforced concrete as a bar surrounded by a circular concrete cover. In this case, it is considered a composite bar, and the

guided wave movement occurs in the entire specimen. In practice, they are leaky guided waves.

2. It is considered 3 cm of concrete cover, but it is variable around the bar and there are bigger covers in the direction of the inner part of the prism. For example, considering 4 cm cover around 8 mm rebar, the velocity increases from 4262 m/s to 4314 m/s, 1.2% of increment.
3. The wave velocity in concrete is considered that one in a plain concrete prism, but it should be that of the concrete around the rebar, what it is practically impossible to measure correctly; and
4. The modeling does not consider the rebar surface deformation.

6.3 BULK WAVES ARRIVAL

The ultrasonic pulse is emitted in 3D space, propagating in all directions. Due to the dissipation phenomenon, the farther the emitted pulse travels, the smaller its energy. In this context, the closer to the perpendicular axis of the transducer, the stronger the wave energy. Figure 6.10 presents a draft of the energy intensity relative to the wave location.

Figure 6.10 - Wave energy intensity

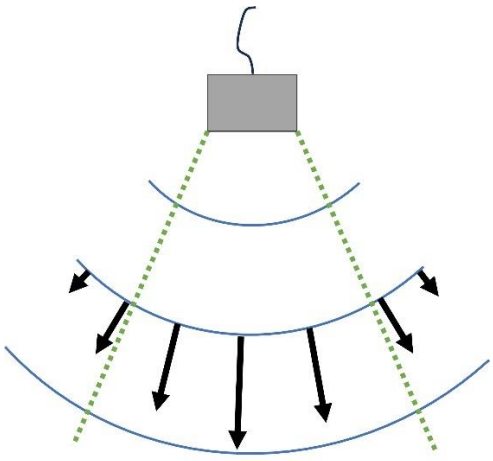

Source: Own elaboration

Thus, there is an ultrasonic beam wherein the energy can be detected by the receiving transducer, while outside this region, the energy can be neglected. It is confirmed by Andreucci (2018) and Malhotra and Carino (2004).

In this context, the first bulk waves arrive at the transducer through reflections, following, in a simplified way, paths 1 and 2 in Figure 6.11.

Figure 6.11 - Paths of first bulk wave reflections

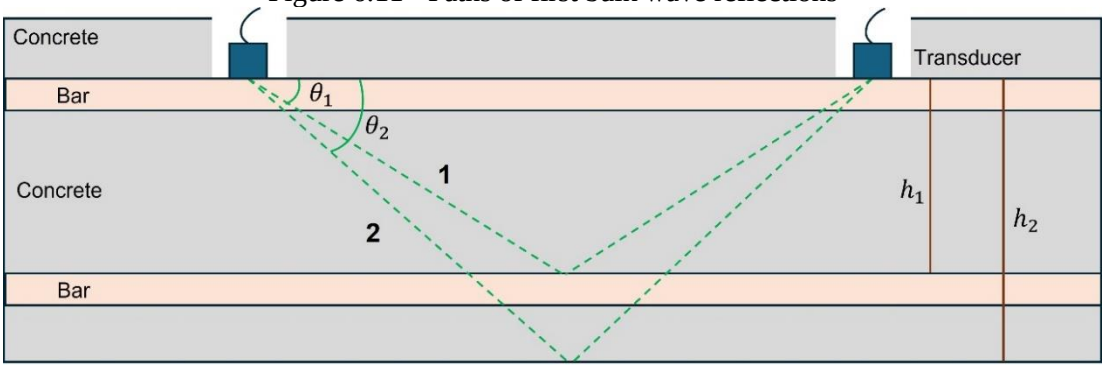

Source: Own elaboration

For path 1, the total distance l_1 is calculated by Equation (6.2).

$$h_1 = H - 2c - \phi \tag{6.1}$$

$$l_1 = 2\sqrt{{h_1}^2 + \left(\frac{d}{2}\right)^2}. \tag{6.2}$$

Where H is the smallest dimension of the prism, c is the concrete cover, ϕ is the bar diameter and d is the distance between transducer's axes.

The angle θ_1 is obtained by Equation (6.3).

$$\theta_1 = \text{atan}\left(\frac{h_1}{l_1/2}\right). \tag{6.3}$$

The portion of l_1 in steel is obtained from Equation (6.4), while that in concrete is $l_{1c} = l_1 - l_{1s}$.

$$l_{1s} = 2\frac{\phi}{\sin(\theta_1)}. \tag{6.4}$$

Therefore, the time to travel in path 1 results from Equation (6.5).

$$t_1 = \frac{l_{1s}}{V_s} + \frac{l_{1c}}{V_c}. \quad (6.5)$$

Where V_s and V_c are the bulk wave velocities in steel and concrete, respectively.

Similarly, the Equations (6.6) – (6.10) are used and the time for path 2 is calculated by Equation (6.11).

$$h_2 = H - c. \quad (6.6)$$

$$l_2 = 2\sqrt{{h_2}^2 + \left(\frac{d}{2}\right)^2}. \quad (6.7)$$

$$\theta_2 = \operatorname{atan}\left(\frac{h_2}{l_2/2}\right). \quad (6.8)$$

$$l_{2s} = 4\frac{\phi}{\sin(\theta_2)}. \quad (6.9)$$

$$l_{2c} = l_2 - l_{2s}. \quad (6.10)$$

$$t_2 = \frac{l_{2s}}{V_s} + \frac{l_{2c}}{V_c}. \quad (6.11)$$

For using the Equations above, Table 6.9 presents the parameters considered in the present work.

Table 6.9 - Parameters for calculating bulk wave arrival time

H (cm)	c (cm)	d (cm)	V_s (m/s)	V_c (m/s)
15	2.5	30	5900	4549

Source: Own elaboration

Based on these values, the times for each diameter are calculated and shown in Table 6.10.

Table 6.10 - Arrival time of Bulk waves reflection

Time (μs)	8 mm	10 mm	12.5 mm	16 mm
t_1	75.6	74.7	73.6	71.9
t_2	82.9	82.1	81.2	79.9

Source: Own elaboration

On the other hand, the first guided wave reflection, at rebar end, is detected by the transducer at the times shown in Table 6.11. In this table, the fastest longitudinal mode velocities for each diameter, obtained previously, are also presented.

Table 6.11 - Arrival time of first guided wave reflection

	8 mm	10 mm	12.5 mm	16 mm
V (m/s)	4262	4194	4241	4190
t (μs)	117	119	118	119

Source: Own elaboration

Therefore, the first wave captured by the transducers is the longitudinal guided wave, which arrives at around 60 μs, a time that corresponds to the wavefront velocity in prisms obtained in Section 6.2, while the bulk waves arrive later, at approximately 74 and 82 μs. Finally, the first reflection of guided waves arrives at around 118 μs. These results are important for analyzing the time window to be selected for the acoustoelastic assessment.

6.4 HIGHLIGHTS OF CHAPTER 6

The key information of the chapter is listed here:

a) In isolated rebars, only the first modes of each kind of guided wave are captured, which are L(0,1), longitudinal, F(1,1), flexural, and T(0,1), torsional. Moreover, the maximum velocity, and consequently the wavefront of all profiles, is related to the first longitudinal mode;
b) The dispersion curve is a material property, whose velocity only depends on the product frequency x thickness.

c) In prisms, the fastest waves are also the longitudinal guided waves, L(0,5) for 8 mm and 10 mm and L(0,4) for 12.5 mm and 16 mm;
d) The approximated arrival times are presented in Table 6.10, which corresponds to the fastest guided wave (GW), first bulk wave reflection (FR), second bulk wave reflection (SR) and first guided wave reflection (GR).

Table 6.12 – Waves Arrival times (μs)

Case	**GW**	**FR**	**SR**	**GR**
Prisms	60	74	82	118
Isolated rebars		-	-	-

Source: Own elaboration

7 RESULTS

This chapter is ordered according to the experiments sequence. Before the main acoustoelastic analysis, from Section 7.2, a parametric analysis was carried out to define the time window which yields the most sensitivity to acoustoelastic effect. Therefore, the results are presented as follows:

a) Section 7.1 presents a time window parametric analysis;
b) Section 7.2 presents the results of the isolated rebars under tension;
c) Section 7.3 presents the results of the prisms under compression; and
d) Section 7.4 presents the results of the prisms under bending.

In all cases, for the cross-correlation, the parameters considered are presented in Table 7.1. The maximum value of intercorrelation function is over 80%, mostly above 90%. The very specific cases under this value are explicitly mentioned in the text.

Table 7.1 - Parameters for cross correlation

Technique	Displacement
Range of displacement (μs)	-2 to 2
Number of increments	500
Time window size (μs)	20
Window beginning (μs)	60

Source: Own elaboration

7.1 PARAMETRIC ANALYSIS OF THE TIME WINDOW

For a better choice of the time window to proceed with the acoustoelastic study, a parametric analysis was performed. For this, the time window size (WS) and its initial time (t_0) were varied. WS assumed the values of 20, 40 and 60 μs, while t_0 assumed the values of 60, 80, 120, 180 and 240 μs. Profiles of one prism and one isolated rebar are used as reference.

7.1.1 Prism

For the analysis of prisms, the profile of Bar 4/P1/8 mm under compression was chosen. Its profile with the considered time windows of WS = 20 μs is shown in Figure 7.1.

Figure 7.1 - Wave profile of Bar 4/P1/8 mm with time windows

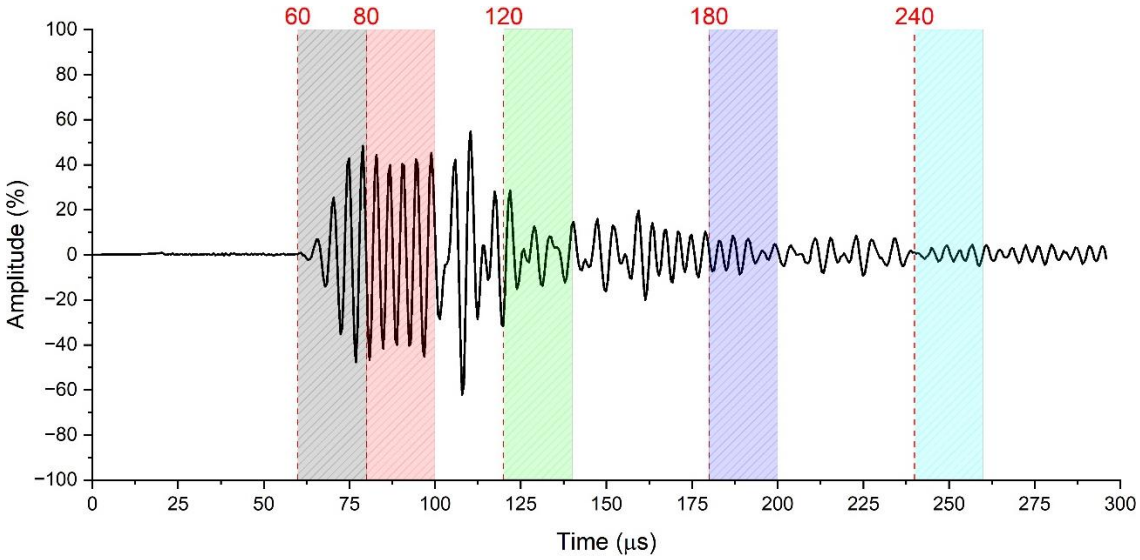

Source: Own elaboration

Figure 7.2 presents the acoustoelastic curves for different initial times with constant time window size.

Figure 7.2 - Parametric analysis – Acoustoelastic curves varying t_0 and with WS constant

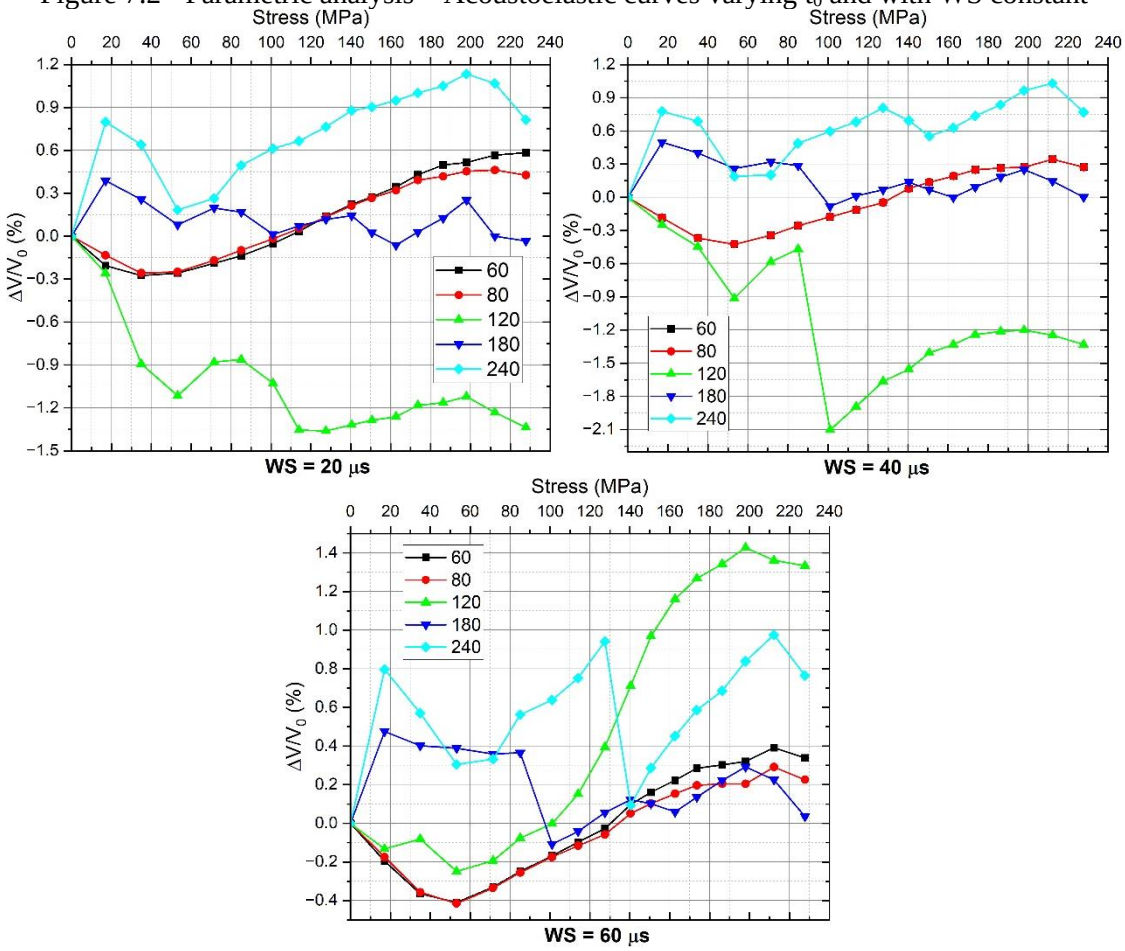

Source: Own elaboration

The curves corresponding to t_0 = 60 and 80 μs exhibit the lowest variability between adjacent measurements. Among them, the result with 60 μs presents slightly higher sensitivity for the acoustoelastic effect. Moreover, they have a well-defined and similar behavior with all window sizes. In addition to them, the curve with t_0 = 120 μs and WS = 60 μs also had a well-defined behavior from 70 MPa.

Another necessary analysis is related to the maximum value of the cross-correlation function ($CC_{máx}$), shown in Figure 7.3, whose values are related to the corresponding curves in Figure 7.2. It is important to guarantee the maximum similarity among the compared waves.

Figure 7.3 - Parametric analysis – Maximum value of the cross-correlation function

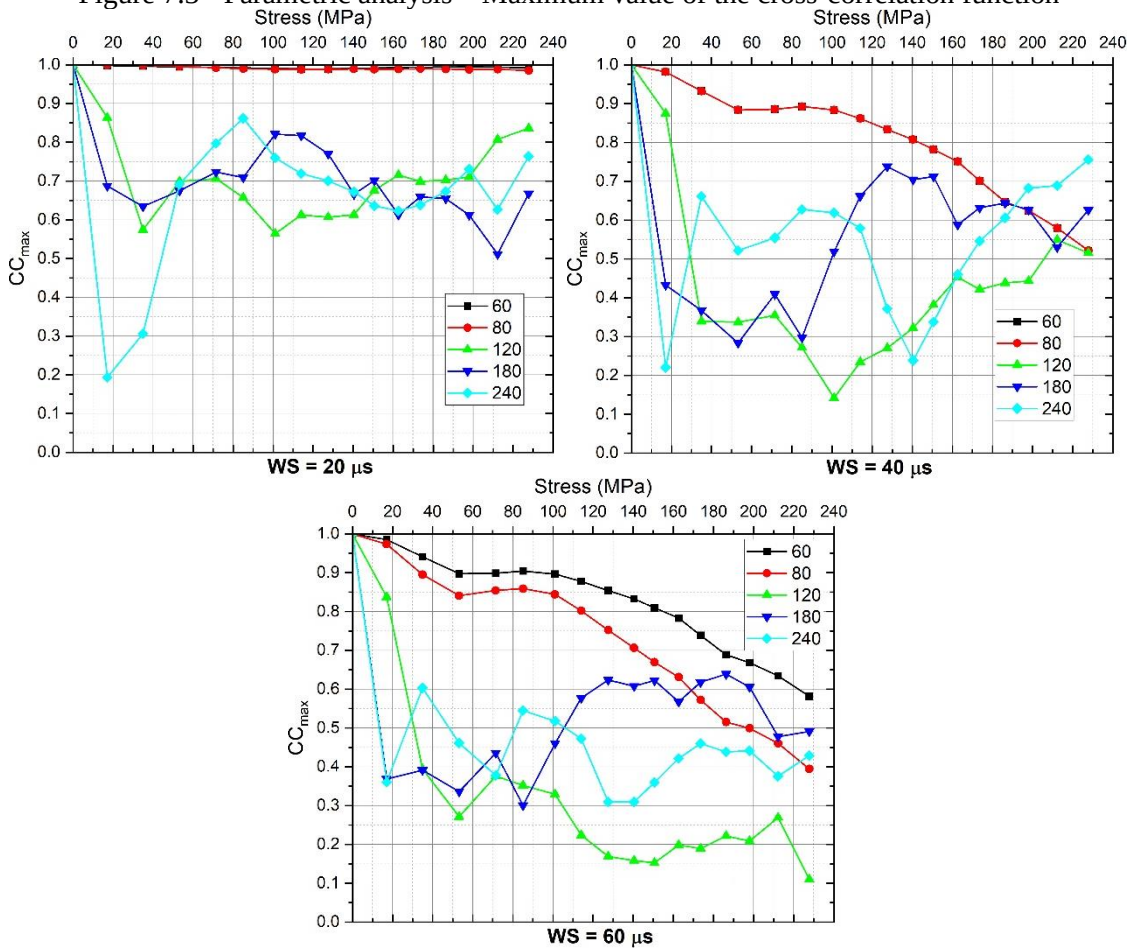

Source: Own elaboration

$CC_{máx}$ with t_0 from 120 μs presents high variability and small values, reaching values around 0.3 in all curves. Conversely, the best results were obtained with t_0 = 60 μs, slightly better than t_0 = 80 μs.

As the results with t_0 = 60 μs are the best in all cases, a specific analysis is carried out varying only the window size. Figure 7.4 shows the acoustoelastic curves and the corresponding maximum values of $CC_{máx}$.

Figure 7.4 - Parametric analysis – Acoustoelastic curves (a) and $CC_{máx}$ (b) varying WS for t_0 = 60 μs

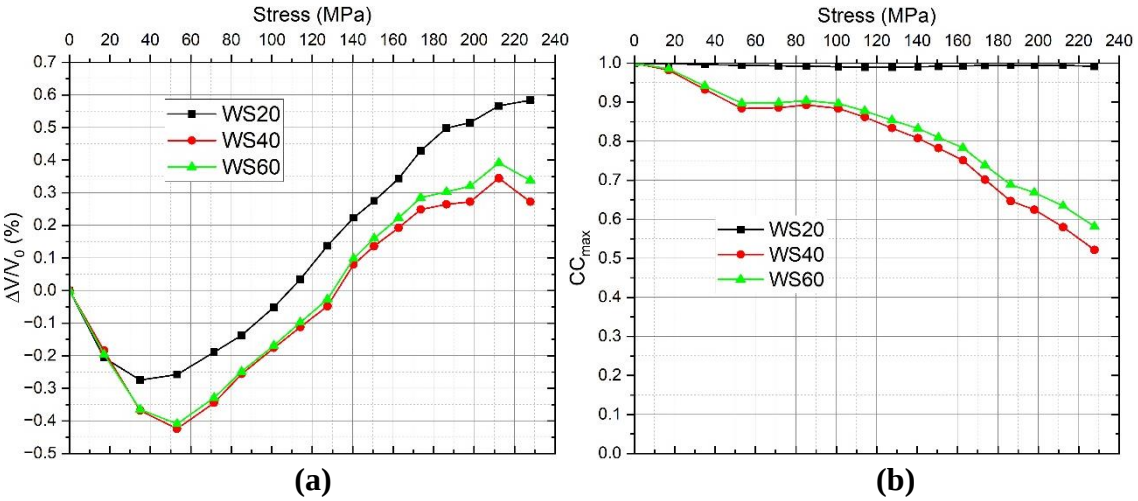

(a) **(b)**

Source: Own elaboration

In terms of window size, there is a tendency of result enhancement the smaller it is, which yields best results of WS = 20 μs. With this size, there is a better sensitivity to acoustoelasticity and all $CC_{máx}$ are practically 1, while with other sizes they decrease gradually, reaching 0.5.

Thus, the best time window for the acoustoelastic analysis in prisms has t_0 = 60 μs and WS = 20 μs.

7.1.2 Isolated rebar

For the analysis of isolated rebars, the profile of 10 mm rebar was chosen instead. Its profile with the considered time windows of WS = 20 μs is shown in Figure 7.5.

Figure 7.5 - Wave profile of 10 mm with time windows

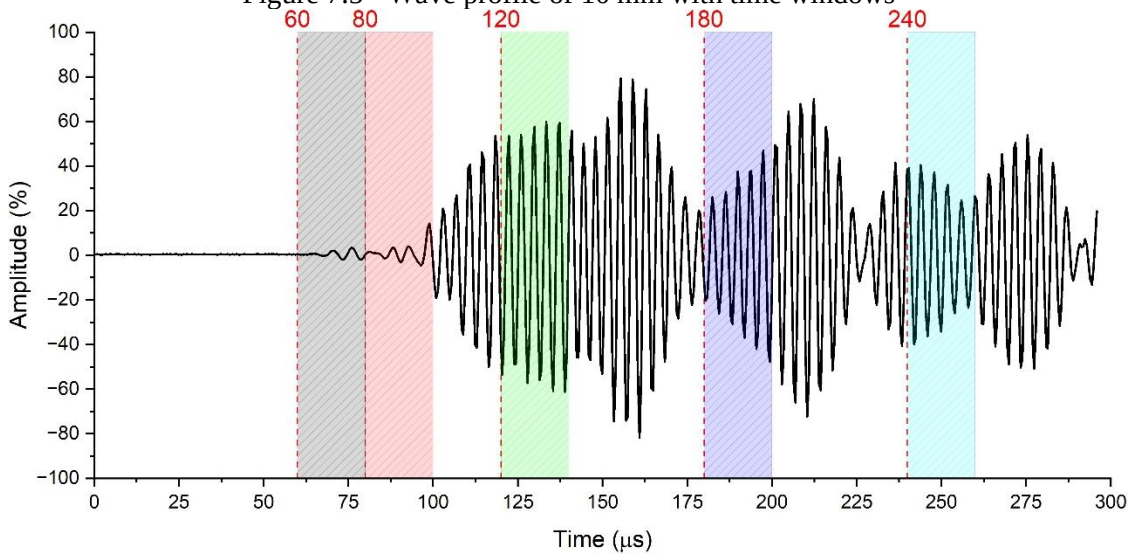

Source: Own elaboration

Figure 7.6 presents the acoustoelastic curves for different initial times with constant time window size.

Figure 7.6 - Parametric analysis – Acoustoelastic curves varying t0 and with WS constant

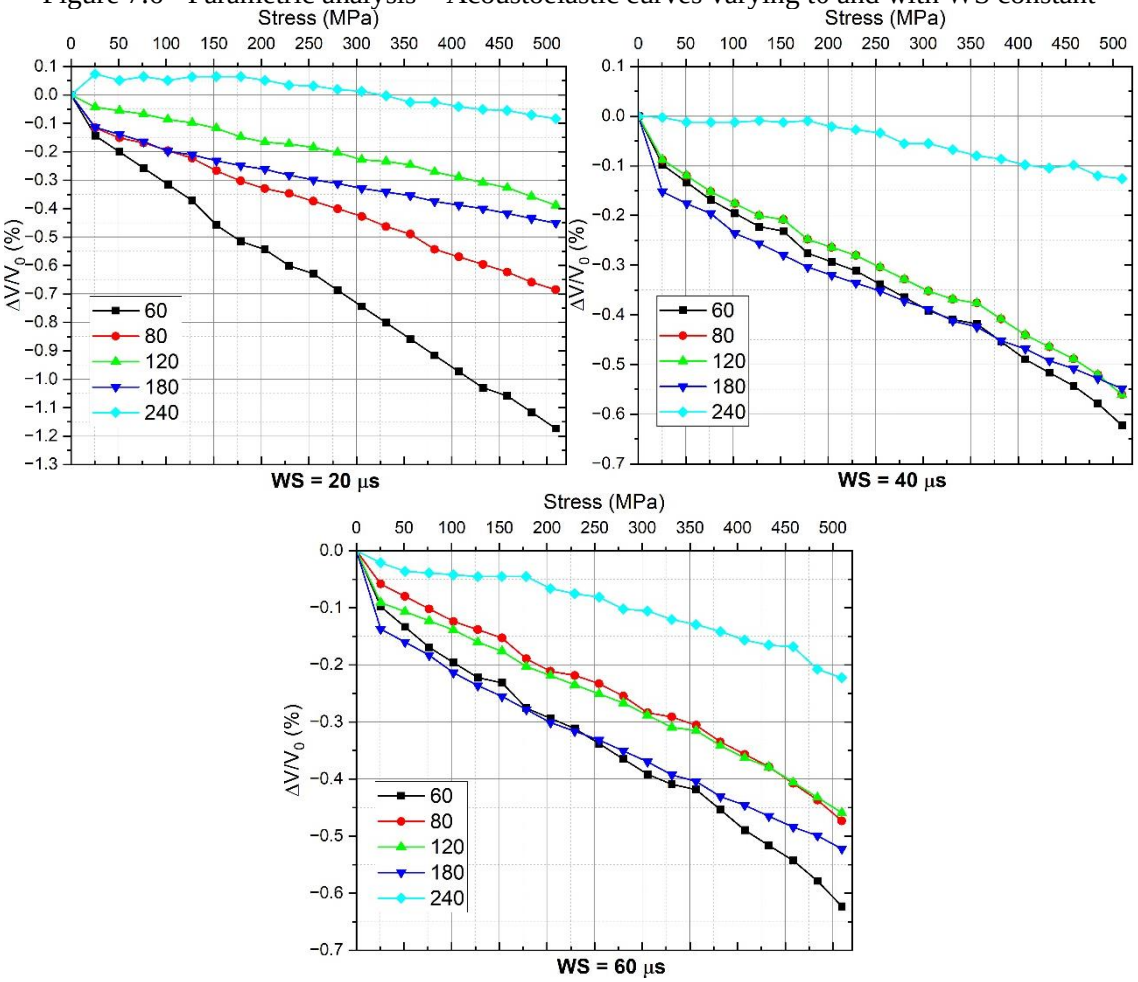

Source: Own elaboration

Different from prisms, the variability in isolated rebars is minimal, and all acoustoelastic curves can be considered linear. Therefore, the main differences among curves are the slope and the relative velocity variation between the first and the second measurements.

The difference in slope is more remarkable with WS = 20 μs, where there is a tendency of the slope to decrease the higher t0 is. Thus, the best sensitivity is obtained with t_0 = 60 μs. With other WS, all curves present similar slopes, with exception of t_0 = 240 μs, whose velocity variation was the smallest among curves. Besides, in all cases, t_0 = 60 μs exhibits the highest variation, which indicates a good sensitivity to acoustoelasticity.

To assess the similarity between profiles, Figure 7.7 presents the values of $CC_{máx}$ of the corresponding curves in Figure 7.6.

Figure 7.7 - Parametric analysis – Maximum value of the cross-correlation function

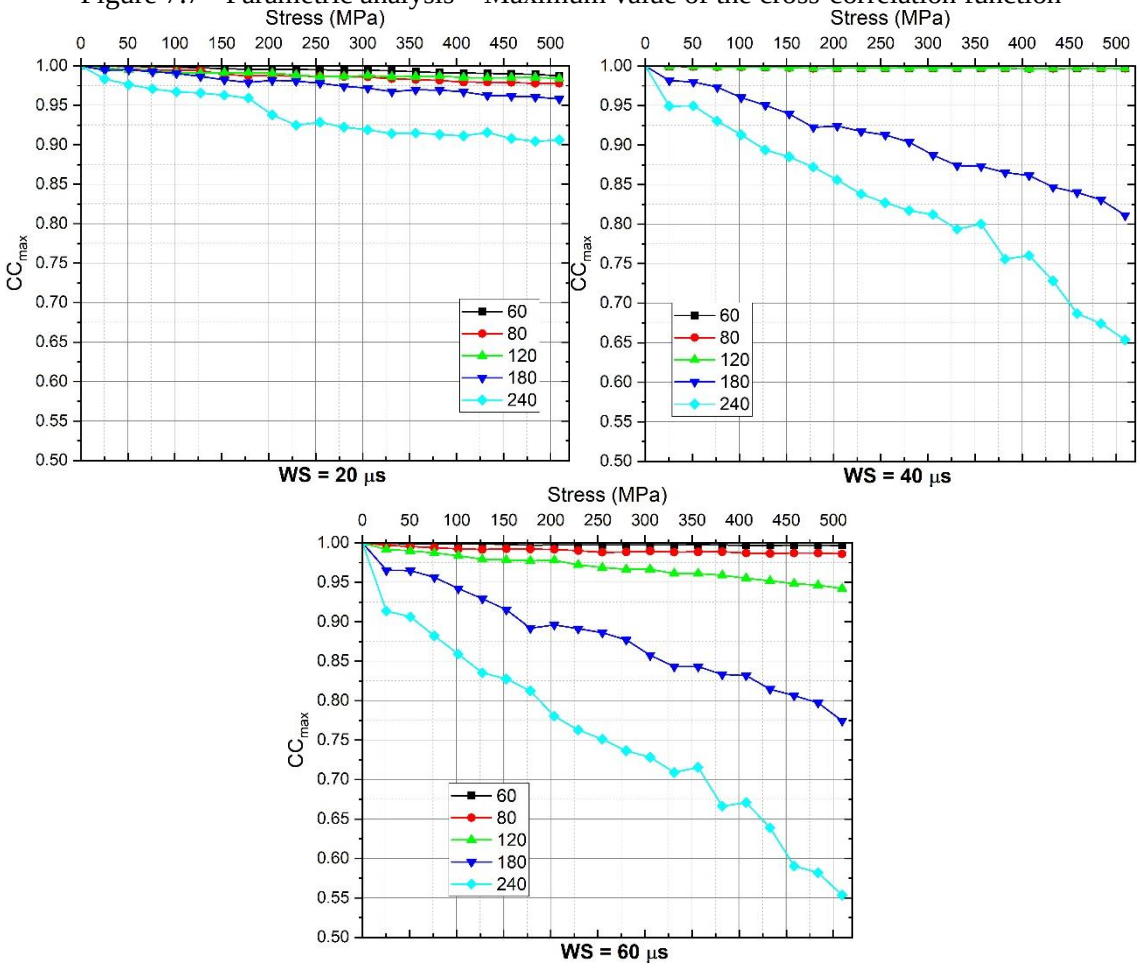

Source: Own elaboration

When compared to prism, $CC_{máx}$ is much bigger in the isolated rebar and there is much less variability. This is because in isolated rebars, only guided waves are generated, and the damage is minimal with the stress increase. In prisms, cracking changes with the load, which makes the rebar boundary conditions to be different in each load step.

The smallest values of $CC_{máx}$ corresponds to the analysis on Coda waves, with t_0 = 180, 240 μs. The other times present a very good $CC_{máx}$ in all cases, over 0.95. Moreover, the highest values correspond to t_0 = 60 μs.

As the results with t_0 = 60 μs are the best in all cases, a specific analysis is carried out varying only the window size. Figure 7.8 shows the acoustoelastic curves and the corresponding maximum values of $CC_{máx}$.

Figure 7.8 - Parametric analysis – Acoustoelastic curves (a) and $CC_{máx}$ (b) varying WS for t_0 = 60 µs

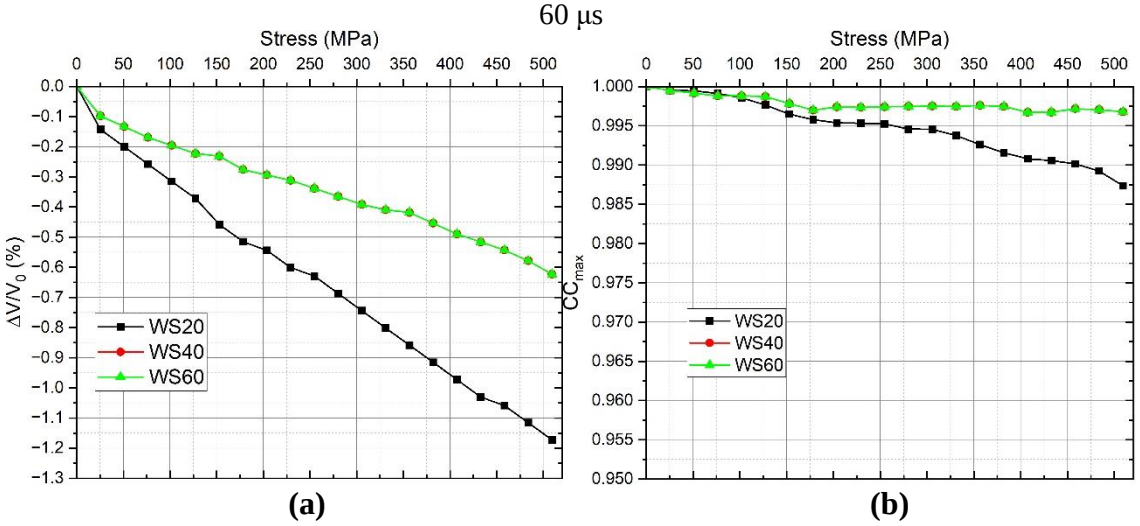

Source: Own elaboration

In terms of acoustoelastic sensitivity, WS = 20 μs stands out, presenting the highest slope, while WS = 40, 60 μs have identical values. In contrast, despite WS = 20 μs to have the smallest $CC_{máx}$, they are still big values, over 0.98.

Therefore, the worst results for analyzing acoustoelasticity were related to time window on Coda wave, mainly due to the low similarity between signals, which may indicate different waves. For this reason and considering the sensitivity for acoustoelastic effect and the highest $CC_{máx}$, in the present study, the analyzed time window has WS = 20 μs and t_0 = 60 μs. The main contribution in this time window is attributed to longitudinal guided waves, as shown in Chapter 6. Moreover, as shown in Section 4.7,

the literature shows that these waves are much more sensitive to acoustoelastic effect than bulk waves.

Considering this time window, the first bulk wave reflection, which arrives around 70 μs, contributes to the final wave profile, whereas the second reflection, that arrives around 80 μs, does not contribute to it. This conclusion is detailed in Section 6.3

7.2 ISOLATED REBARS UNDER TENSION

Isolated rebars were submitted to tension tests. One pilot test was conducted in rebars of 20 mm, then the main experiments with the diameters of 8, 10, 12.5 and 16 mm were carried out in two instants. Due to the high number of curves of isolated rebars, solely to improve the clarity of the graphs, the results of the main experiments are separated into Test 1 and Test 2.

7.2.1 Pilot test in specimens with 20 mm

Figure 7.9 presents the results obtained with 20 mm.

Figure 7.9 – Isolated rebars – 20 mm – Acoustoelastic curves

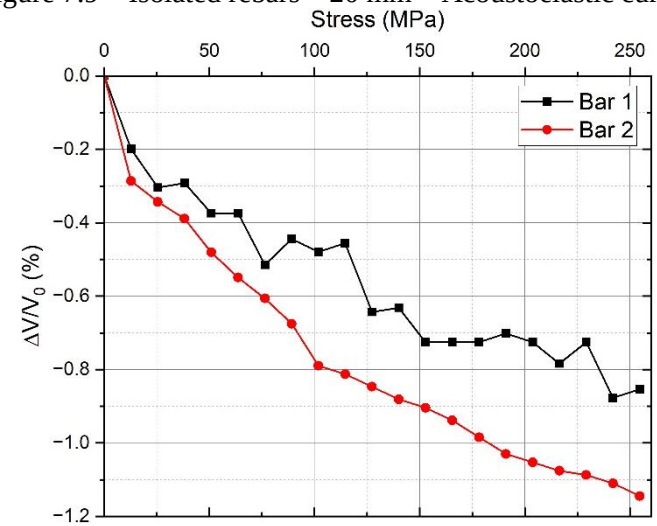

Source: Own elaboration

Both acoustoelastic curves present a behavior approximately linear, with the maximum relative velocity variation of -0.9 % for Bar 1 and -1.1 % for Bar 2. Considering

a linear variation, the acoustoelastic coefficients are K = -2.8 x 10^{-2} GPa^{-1} and K = -3.9 x 10^{-2} GPa^{-1}, respectively. For the obtention of each K, $R^2 > 0.9$.

There is a significant slope from the first to the second measurement. It might be due to an initial accommodation of the transducers on the bar and of the loading equipment. If the second measurement is considered as reference, the above parameters turn into -0.7% and K = -2.6 x 10^{-2} GPa^{-1} for Bar 1 and -0.9% and K = -3.6 x 10^{-2} GPa^{-1} for Bar 2. For the obtention of each K, $R^2 > 0.92$.

The curve of Bar 1 presents more variability than Bar 2, what can be explained by slight displacements of the transducers on the bar during loading. Despite the rubber support used to fix the transducers to the rebar, the irregular, small, circular shape of the surface and the slippery contact gel make it difficult to keep the transducers stable, what may cause displacements.

7.2.2 Experiments with diameters from 8 to 16 mm

In Test 1, two samples of each diameter were submitted to tension tests until the yield limit, but before yielding. Figure 7.10 presents the Ultimate Variation (UV), the acoustoelastic coefficient (K) and the respective R^2.due to the i

Figure 7.10 – Isolated rebars – Test 1 – Acoustoelastic curves

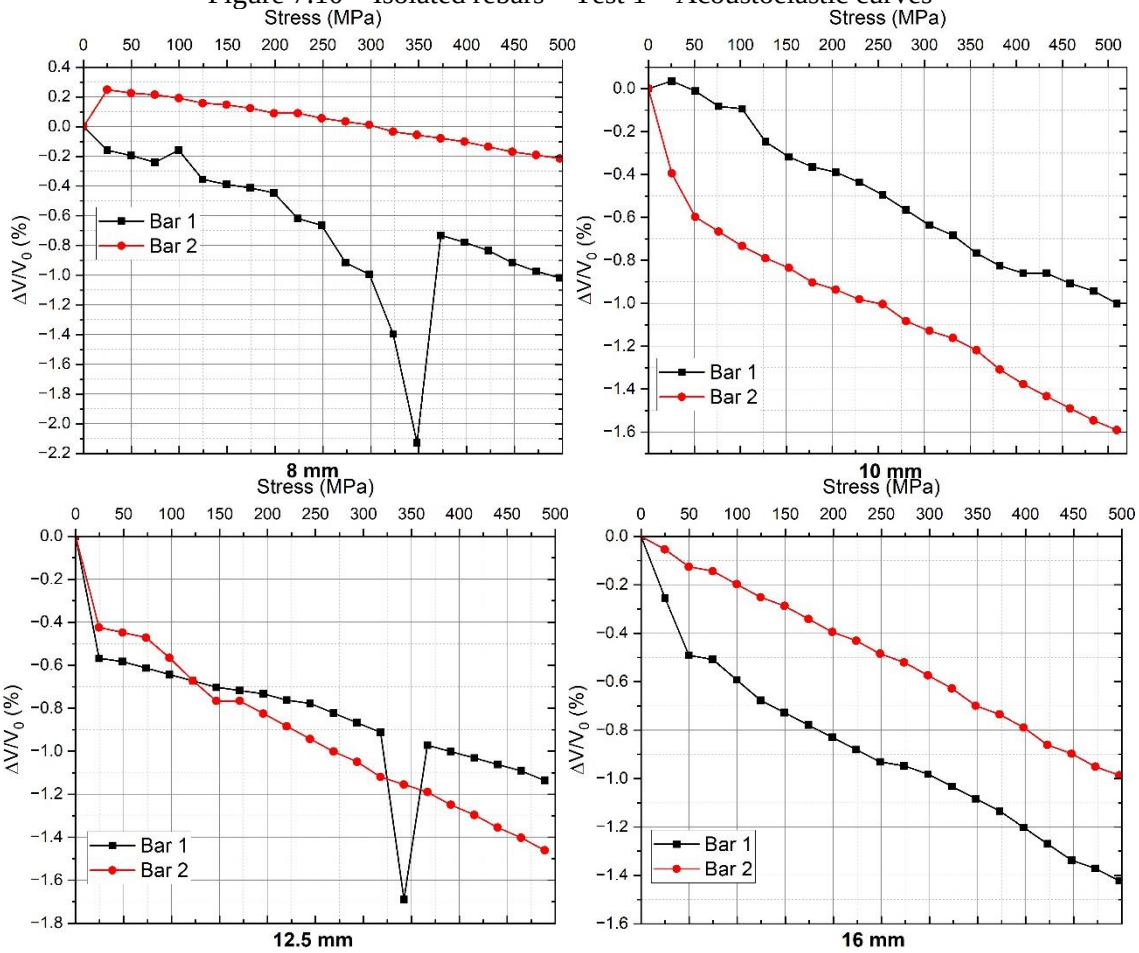

Source: Own elaboration

Table 7.2 summarizes the main characteristics of the curves.

Table 7.2 – Isolated rebars – Test 1 – Acoustoelastic curves features

Diameter (mm)	UV (%)		K (x 10^{-2} GPa^{-1})		R^2	
	Bar 1	Bar 2	Bar 1	Bar 2	Bar 1	Bar 2
8	-1.0	-0.2	-2.3	-0.8	0.51	0.82
10	-1.0	-1.6	-2.2	-2.4	0.99	0.93
12.5	-1.1	-1.5	-1.7	-2.5	0.61	0.95
16	-1.4	-1.0	-2.3	-2.0	0.94	1.00

Source: Own elaboration

In all cases, the relative velocity variation is negative and there is a linear behavior in most of them. The curves present acoustoelastic constants very close, around K = -2.3 x 10^{-2} GPa^{-1}, with exception of 8 mm/Bar 2 and 12.5 mm/Bar 1. The ultimate variations ranged from -0.2% to -1.6%., with 50% around -1% and 37%, around -1.5%.

The biggest variabilities occur in specific parts of the curves: at the beginning, with a big slope, and around 350 MPa in the cases of Bar 1 of 8 mm and 12.5 mm. Moreover, the initial part of Bar 2 of 8 mm is different from the others, with the only positive initial variation.

These abnormal behaviors can be analyzed by the corresponding wave profiles. Figure 7.11 shows the acoustoelastic curves of 8 mm/Bar 2 and 12.5 mm/Bar 1 and their respective time window on the right. For both cases, the wave profile in red corresponds to the unloaded state, the reference profile. While in the second case, 12.5 mm, the wave profile in blue corresponds to stress $\sigma = 342$ MPa, where there is an abnormal behavior on the curve.

Figure 7.11 - Wave profile of 8 mm/ Bar 2 and 12.5 mm/Bar 1

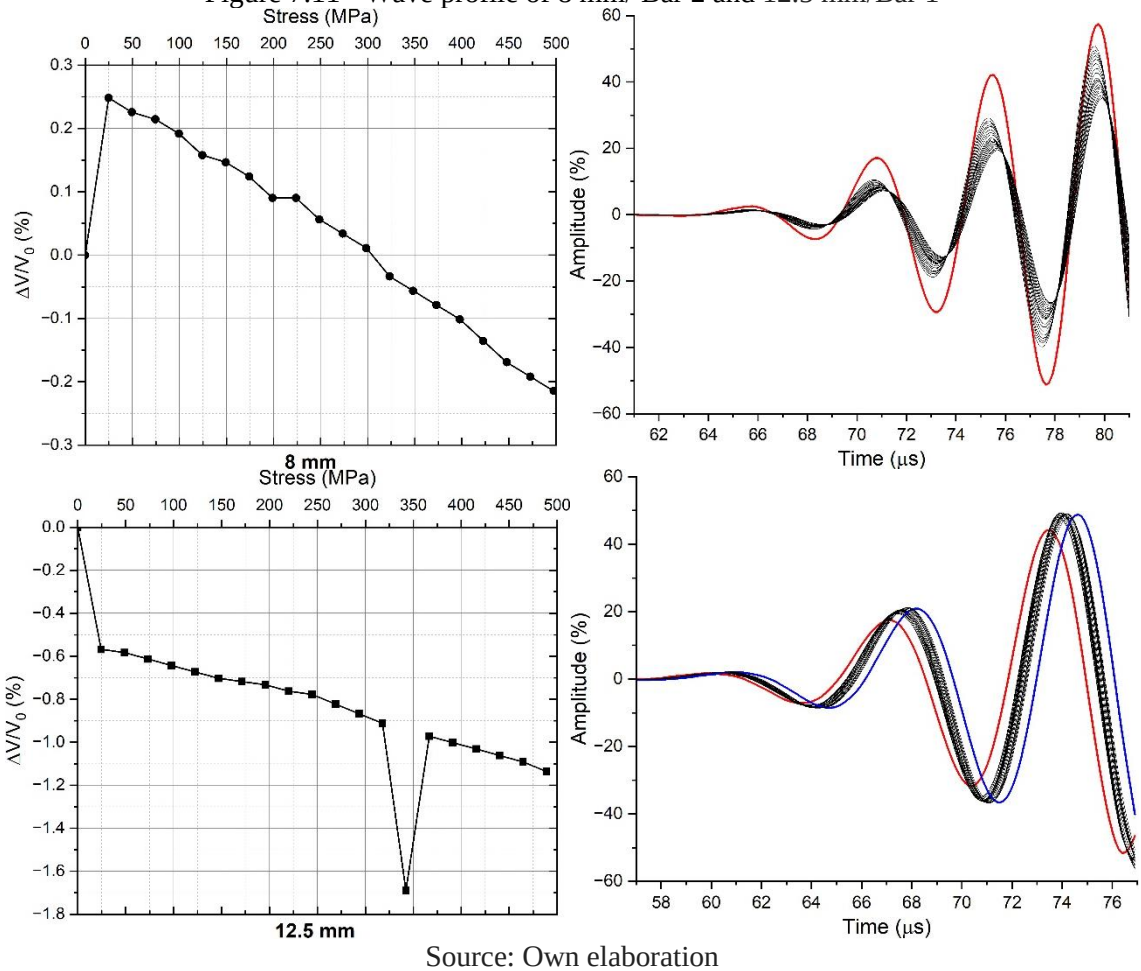

Source: Own elaboration

In the case of 8 mm, the energy of the refence wave is greater than the others, which makes the correlation analysis difficult, because the relative time variation might be confused with profile distortion. It may justify the initial positive variation in the

acoustoelastic curve, as the first measurement is very different from the rest, whose variation is negative and linear.

The greater amplitude of the reference signal, unstressed state, is attributed to the fact that the rebar ends were not tightly fixed as they were during loading application. Consequently, as the guided wave propagates through the entire specimen, the surface displacement is larger compared to cases with applied stress. This results in more energy being received by the transducer.

In the case of 12.5 mm, different from the previous case, there is a clear displacement of both profiles on the time axis. The first measurement, red profile, is possibly a result of an initial accommodation of the transducers due to the operation start of the experiment system. This accommodation might be influenced by the slippery contact surface and the difficulty in fixing the transducers on the bar, what can also justify the measurement of the blue profile.

Because of that, it is important to disregard these specific measurements and consider the third one as reference for each acoustoelastic curve, which correspond to $\sigma = 50$ MPa, as shown in Figure 7.12.

Figure 7.12 - Isolated rebars – Test 1 – Curves with the third measurement as reference

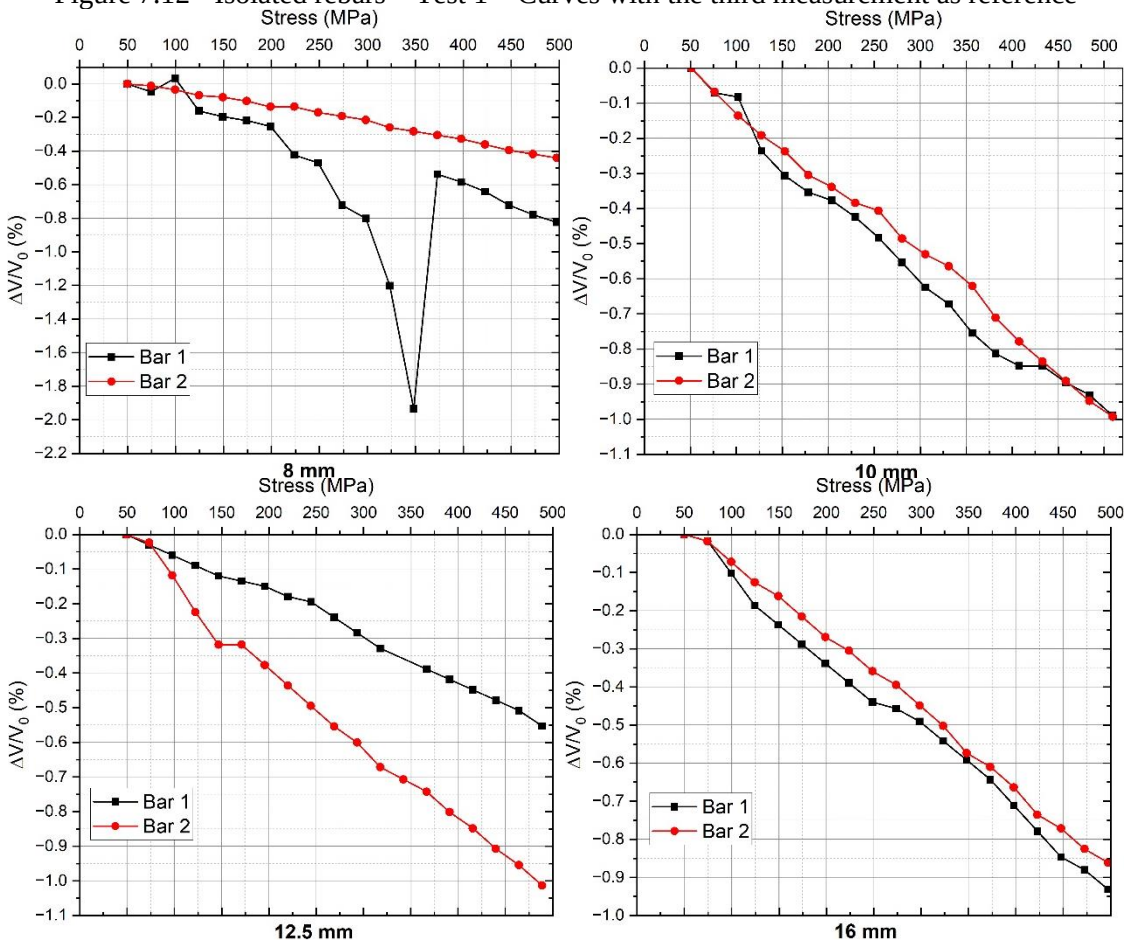

Source: Own elaboration

Table 7.3 summarizes the main characteristics of the curves.

Table 7.3 – Isolated rebars – Test 1 – Acoustoelastic curves feature with third measurement as reference

Diameter (mm)	UV (%)		K (x 10^{-2} GPa^{-1})		R^2	
	Bar 1	Bar 2	Bar 1	Bar 2	Bar 1	Bar 2
8	-0.8	-0.4	-2.2	-1.0	0.40	0.99
10	-1.0	-1.0	-2.2	-2.1	0.98	1.00
12.5	-0.6	-1.0	-1.2	-2.3	0.99	0.99
16	-0.9	-0.9	-2.0	-2.0	0.99	1.00

Source: Own elaboration

Therefore, when the third measurement is considered as the reference, the curves become entirely linear, as indicated by $R^2 \geq 0.98$. An exception to this is the curve for 8 mm/Bar 1, which exhibits anomalous behavior that could not be explained.

In 12.5 mm, despite the linearity of both curves, the acoustoelastic coefficients are very different, K = -1.2 x 10^{-2} GPa^{-1} and K = -2.3 x 10^{-2} GPa^{-1} for Bar 1 and 2,

respectively. The ultimate relative velocity variations are 0.6% and -1%, respectively. In contrast, for 10 mm and 16 mm, both curves have great similarity, with K around -2.2 x 10^{-2} GPa^{-1} and a maximum variation around -1%.

When all results are put together, Figure 7.13 is obtained. In this figure, the outliers of 8 mm/Bar 1 are excluded and interpolation is done. Besides, a trendline is plotted disregarding 8 mm/Bar 2 and 12.5 mm/Bar 1.

Figure 7.13 - Isolated rebars – Test 1 – Acoustoelastic curves of all diameters

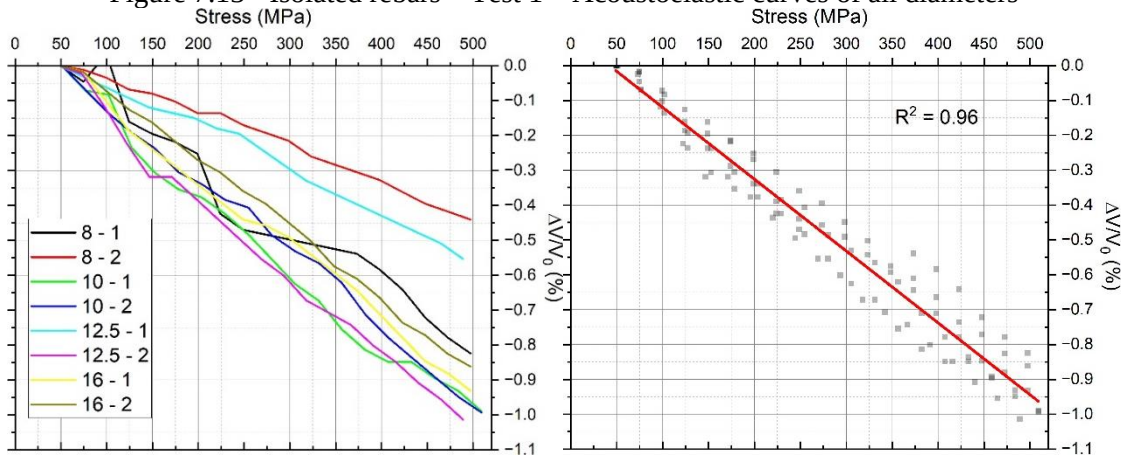

Source: Own elaboration

When $\sigma \approx 50$ MPa is taken as reference, the ultimate relative velocity variation of most curves varies in the range -0.85/-1%. Considering the trendline, the acoustoelastic coefficient is K = -2 x 10^{-2} GPa^{-1}.

The only exceptions to this are 8 mm/Bar 2 and 12.5 mm/Bar 1, whose acoustoelastic coefficient is around -1.0 x 10^{-2} GPa^{-1}, reaching around -0.5% of ultimate variation.

In Test 2, the two other samples with diameters of 8, 10, 12.5 and 16 mm were subjected to tension, whose results are shown in Figure 7.14.

Figure 7.14 - Isolated rebars – Test 2 – Acoustoelastic curves

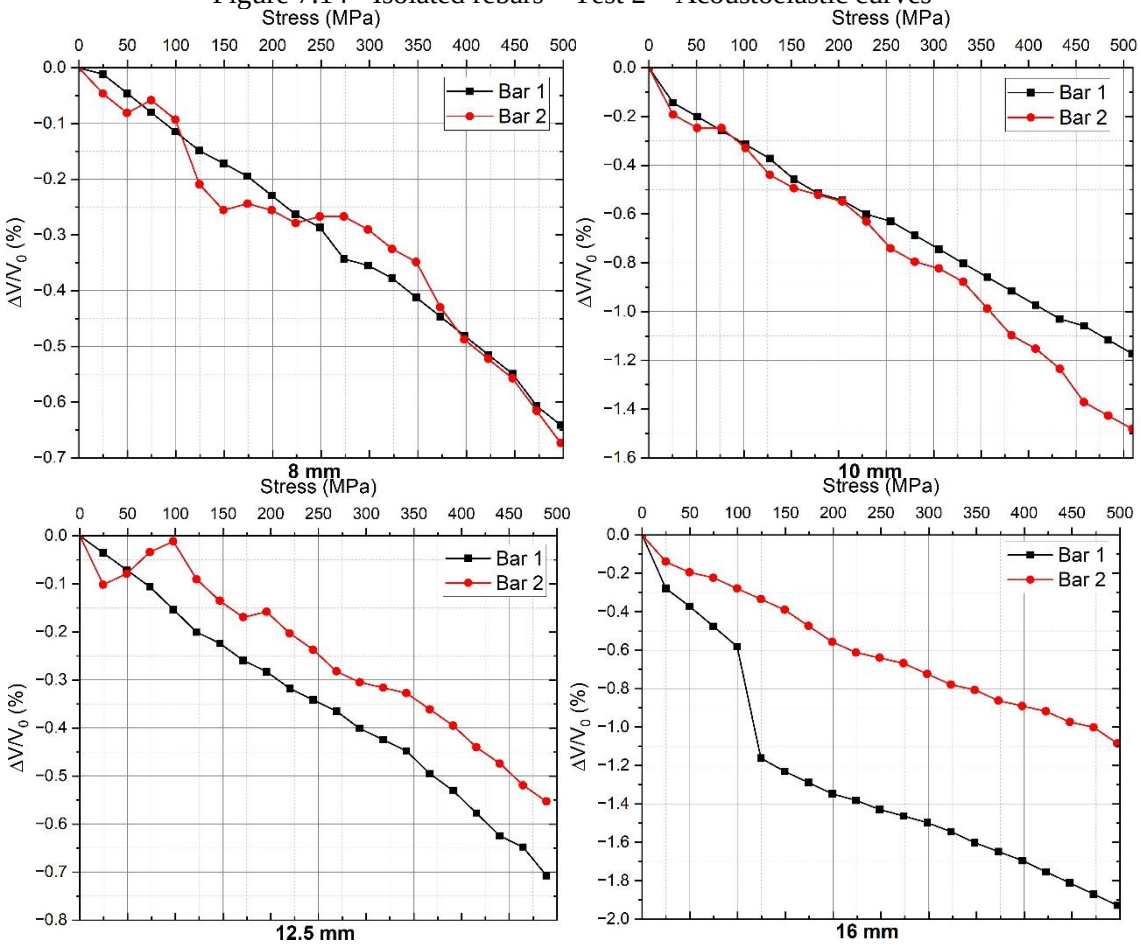

Source: Own elaboration

Table 7.4 summarizes the main characteristics of the curves.

Table 7.4 – Isolated rebars – Test 2 – Acoustoelastic curves feature

Diameter (mm)	**UV (%)**		**K (x 10^{-2} GPa^{-1})**		**R^2**	
	Bar 1	**Bar 2**	**Bar 1**	**Bar 2**	**Bar 1**	**Bar 2**
8	-0.6	-0.7	-1.3	-1.2	1.00	0.97
10	-1.2	-1.4	-2.2	-2.7	1.00	0.99
12.5	-0.6	-0.7	-1.4	-1.1	0.99	0.96
16	-2.0	-1.0	-3.4	-2.0	0.86	0.98

Source: Own elaboration

In the case of 8 mm, both curves have similar behavior, with K around -1.3 x 10^{-2} GPa^{-1}. With respect to 10 mm, the curves are similar up to 325 MPa, from where the slope of Bar 2 becomes steeper.

Regarding 12.5 mm, Bar 1 is entirely linear, with K around -1.4 x 10^{-2} GPa^{-1} and maximum variation of -0.7%, while Bar 2 presents an unusual positive variation at the beginning, with K = -1.1 x 10^{-2} GPa^{-1} and final variation of -0.6%. This positive part might be justified by small displacements of the transducers.

The cases of 16 mm present high variability between curves, mostly because of the unrealistic increase in slope of Bar 1, around 100 MPa. This phenomenon is the same as in 12.5 mm/Bar 1 of Tests 1 (see Figure 7.11), which is related to transducer displacement. But in this case, after transducers' movement, their relative position did not return to the original one.

Considering the third measurement as reference and eliminating the gap in Bar 1 of 16 mm, Figure 7.15 is obtained. In this figure, all positive results are disregarded.

Figure 7.15 - Isolated rebars – Test 2 – Acoustoelastic curves of all diameters and trendlines

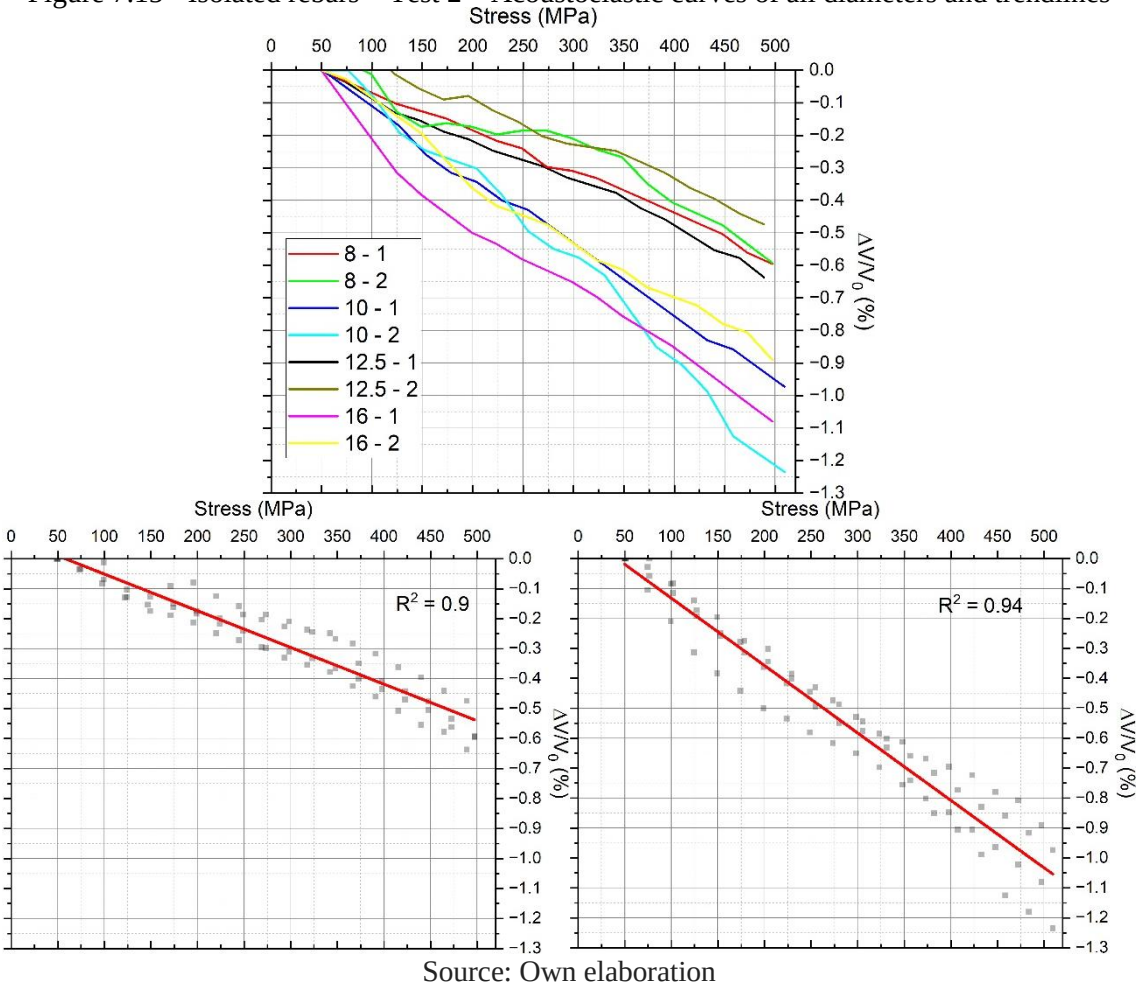

Source: Own elaboration

There are clearly 2 groups of curves:

1. Those related to diameters of 8 and 12.5 mm, whose trendline has K = -1.2 x 10^{-2} GPa^{-1} and ultimate variation of -0.6%; and
2. The group constituted by diameters 10 and 16 mm, whose trendline has K = -2.2 x 10^{-2} GPa^{-1} and ultimate variation of -1.1%.

7.2.3 Summarized results of the main experiments – Test 1 and Test 2

The results in isolated bars are summarized in Figure 7.16 and Figure 7.17, with the acoustoelastic curves and the respective trendlines. For this figure, only rebar 20 mm were not considered.

Figure 7.16 - Results of Test 1 and Test 2 – 8 and 10 mm

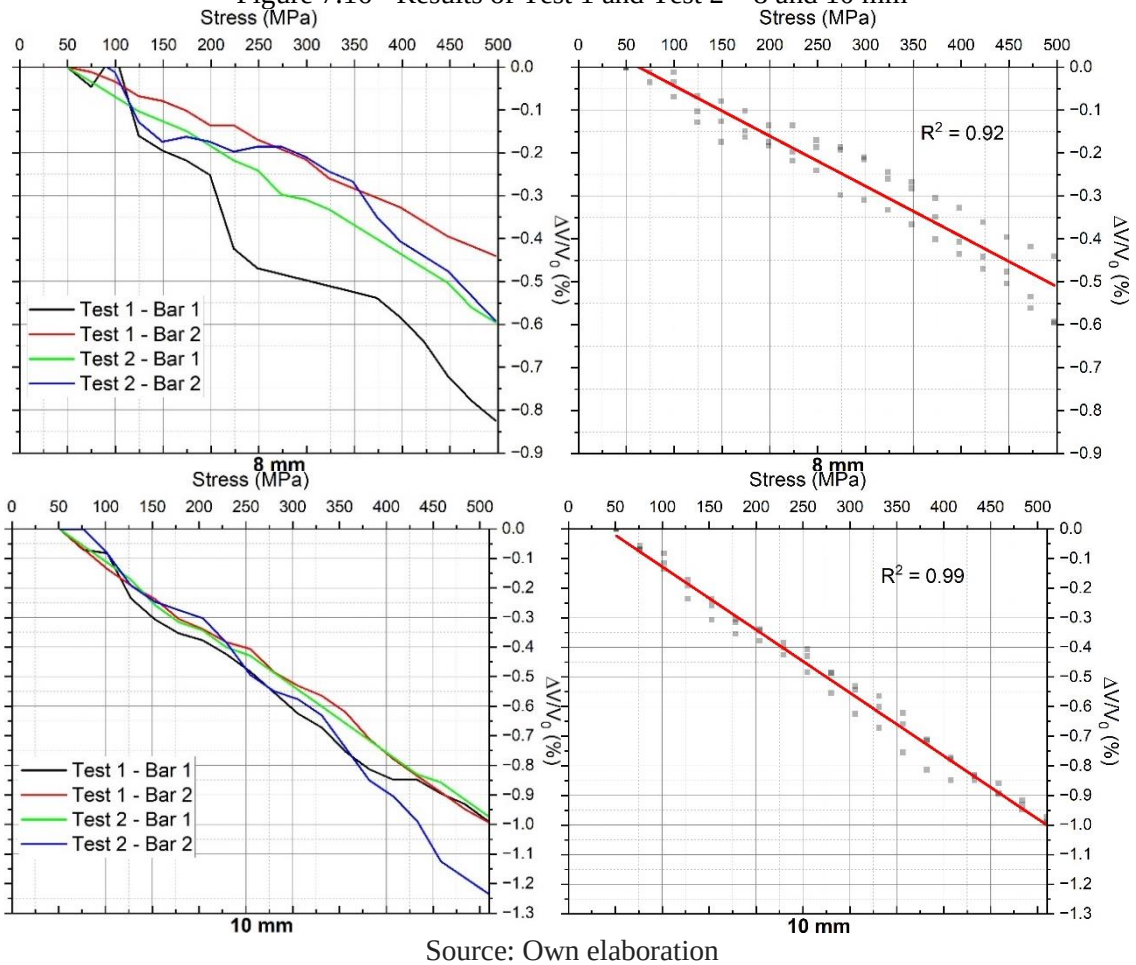

Source: Own elaboration

Figure 7.17 - Results of Test 1 and Test 2 – 12.5 and 16 mm

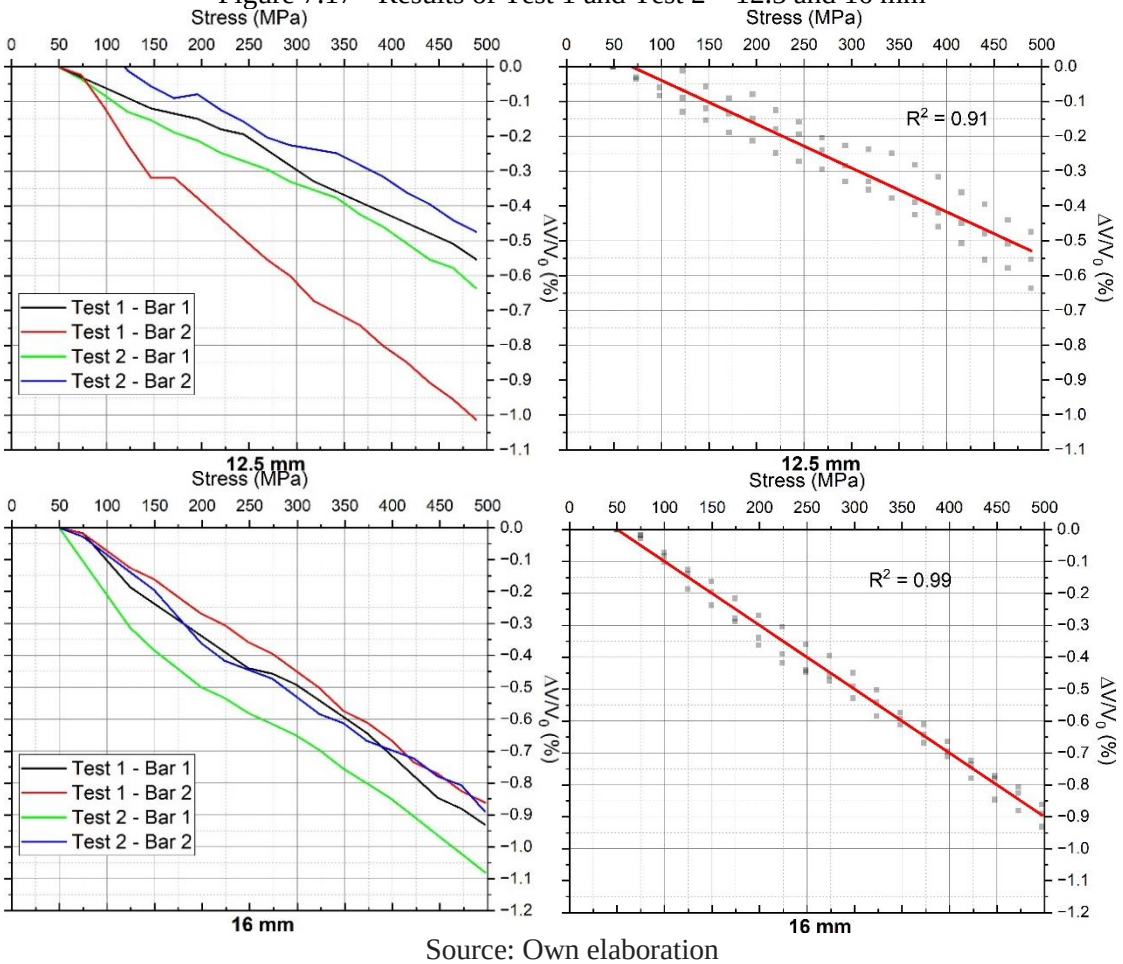

Source: Own elaboration

For each diameter, there is one curve that deviates significantly from the trend observed in the others. The trendlines were plotted disregarding these outliers. Table 7.5 presents the disregarded curves. In this context, the diameter of 8 mm has the highest variability among all rebars, mostly because it is the smallest diameter, which becomes the most difficult surface to fix the transducers.

Table 7.5 - Disregarded curves

Diameter (mm)	**Bar**
8	Test 1 – Bar 1
10	Test 2 – Bar 2
12.5	Test 1 – Bar 2
16	Test 2 – Bar 1

Source: Own elaboration

Based on the trendlines, the ultimate relative velocity variation for each diameter and the respective acoustoelastic coefficient are obtained, as shown in Table 7.6.

Table 7.6 - Ultimate variation and acoustoelastic coefficient

Diameter (mm)	**Ultimate variation (%)**	**K (10^{-2} GPa^{-1})**
8	-0.50	-1.17
10	-1.00	-2.13
12.5	-0.55	-1.26
16	-0.90	-2.00

Source: Own elaboration

Therefore, the acoustoelastic coefficient for isolated bars under tension are approximately K = -1.2 x 10^{-2} GPa^{-1} for the diameters 8 and 12.5 mm, and K = -2.1x 10^{-2} GPa^{-1} for the diameters 10 and 16 mm. Furthermore, all curves are negative and approximately linear.

7.3 PRISMS UNDER COMPRESSION

In this section, the results in prisms under compression are discussed. One pilot test was conducted in specimens with rebars of 20 mm, then the main experiments with diameters of 8, 10, 12.5 and 16 mm were carried out. Additionally, despite the strain variation along the rebars, only the strain at the midpoint is considered in the analyses due to the positioning of the strain gauges.

7.3.1 Pilot test in specimens with 20 mm

After prism casting, the surface of the openings presented a very thin cement layer over the bar, tangentially to it. In P13, after obtaining the first results, this layer was removed and the bar surface was exposed, so that the transducers could be in contact only with the bar. Figure 7.18 shows the wave profiles for both cases in the same bar. The left profile is related to the case with the cement layer, obtained with a voltage of 500 V and a signal gain of 1,000x, and the right one is related to the case after its removal, obtained with 250 V and 50x.

Figure 7.18 – Compression – 20 mm – P13 – Profile before (a) and after (b) cement layer removal

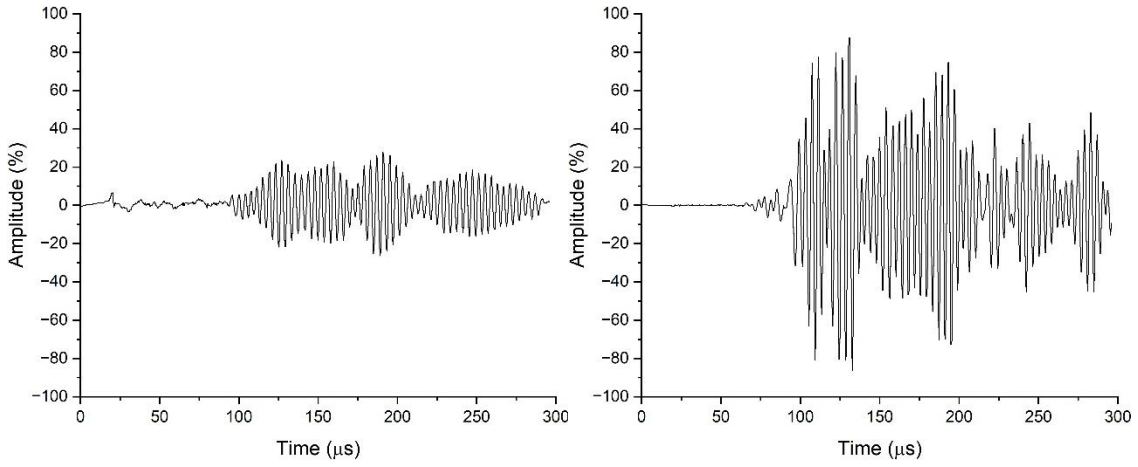

Source: Own elaboration

Despite the much higher voltage and signal gain in the first case, the amplitude did not exceed 30%, while in the second case, it reached 90%. This occurs because with the cement layer, the pulse energy dissipates partially in the concrete before propagating into the bar, while in the other case, all the energy goes into the bar before dissipating.

Due to the high signal gain in the first case, it is not possible to determine the wavefront arrival, which is confused with signal noise. In contrast, in the second case, this arrival can be easily determined. Therefore, during the prisms casting, it is guaranteed that the bar surface is slightly exposed, and during ultrasonic tests, the signal gain of 50x is used as the upper limit.

Figure 7.19 presents the acoustoelastic curves of the cases above.

Figure 7.19 – Compression – 20 mm – P13 – Acoustoelastic curves with contact variation

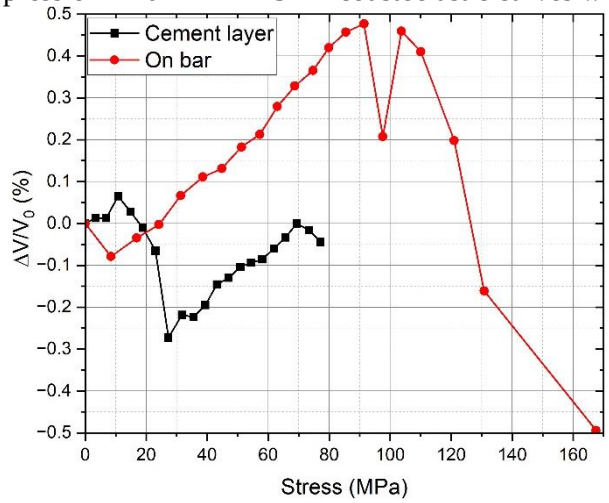

Source: Own elaboration

Due to the low energy in the first case, with cement layer, it was not possible to detect the wavefront arrival at $t_0 = 60\ \mu s$. For this reason, a time window with $t_0 = 144\ \mu s$ was considered. No tendency is observed in the curve.

In the other case, On bar, it was possible to capture the longitudinal wave arrival. On the curve, after an initial negative variation, there is a linear positive variation between 10 and 90 MPa. This linear part results in a maximum relative velocity variation of 0.5%, which corresponds to K = 6.7 x 10^{-2} GPa^{-1}.

Nevertheless, these rebars were submitted to low stress, smaller than 15% of the yield stress for the first case and 34% for the second one. These values are even smaller than those considered in ABNT NBR 6118:2024 for structures in service conditions. Thus, it is necessary to assess the rebars under higher stress.

In prism P14, the influence of preloads on the acoustoelastic curves is analyzed. In this case, only Bar 2 was not assessed due to problems in the corresponding strain gauge. Furthermore, only on wave profile of Bar 1, it was possible to identify the longitudinal mode arrival. Because of that, in Bars 3 and 4, the wavefront arrival, which is a mix of many types of waves and reflections, are $t_0 = 96\ \mu s$ and $t_0 = 99\ \mu s$, respectively.

The prism was submitted to 0, 10, 20 and 30 cycles of preloading, wherein the maximum load was the same as the test's. The acoustoelastic curves are presented in

Figure 7.20 for Bars 3 and 4. For each bar, there is the full curve on the left and on the right, the first measurement is disregarded, and the second one is considered as reference.

Figure 7.20 – Compression – 20 mm – P14 – Effect of preloading on the curves – Full curves (a and c) and the corresponding curves with the first measurement disregarded (b and d)

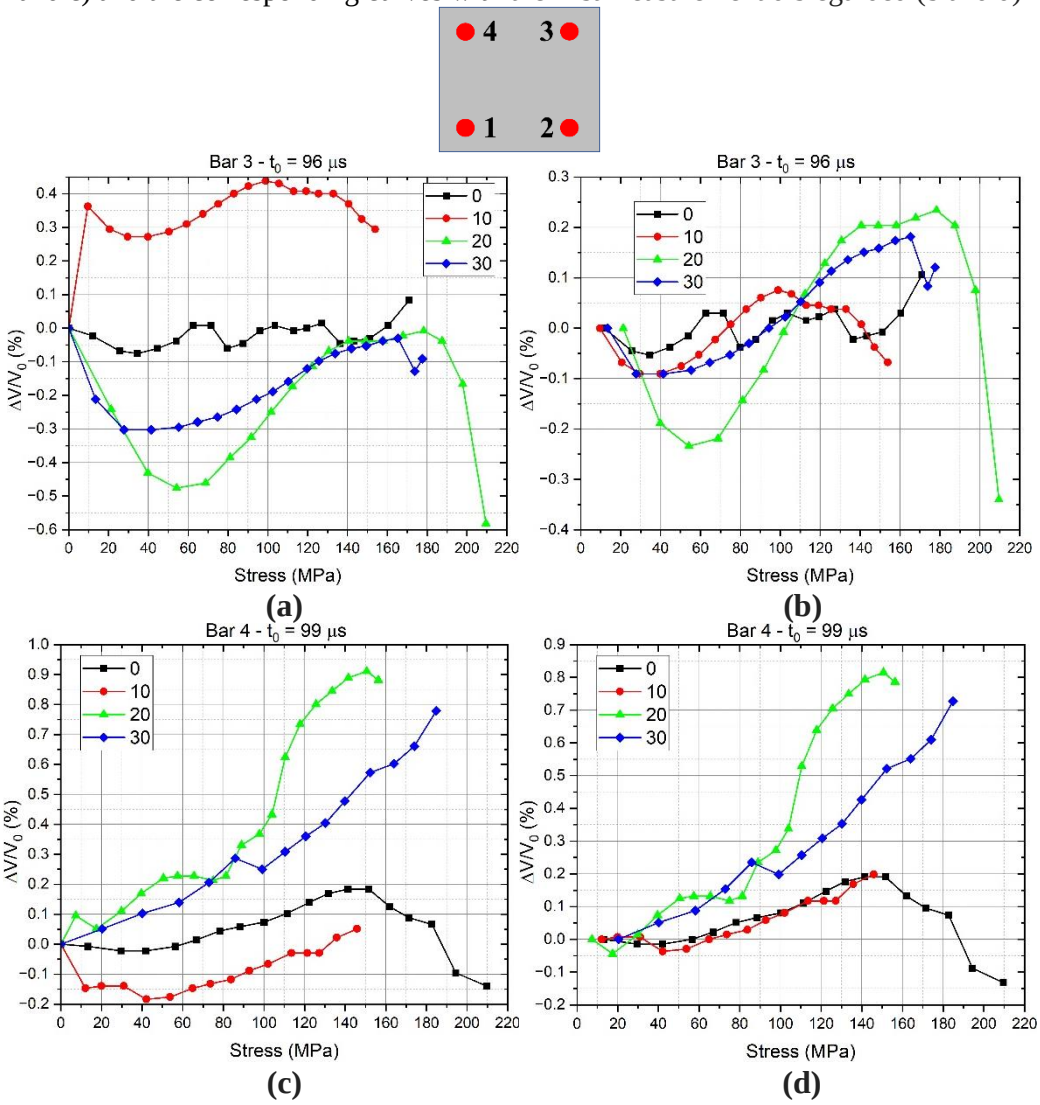

Source: Own elaboration

In Bar 3, there is a great slope between the first measurement and the second. It might be a consequence of a slight accommodation of the transducers, which causes a change in the wave travel distance. It happens mainly in the case of 10 cycles, and unlike the other curves, it presents a positive initial variation.

Considering the second measurement as reference, all curves present similar behaviors, with a negative and nonlinear initial variation, followed by an almost linear and positive trend and finally a nonlinear decay. Moreover, the only different behavior

occurs with cycle 0, where there is just the initial part like the others, and almost there is no acoustoelastic effect. Despite that, there is a great variability between the curves.

Finally, there is not a clear tendency of the curves with preloading cycles. Nevertheless, the higher the cycle, the greater the positive relative velocity variation, what may demonstrate the influence of preloading.

In Bar 4, cycles 0 and 10 almost present the same slope, while cycles 20 and 30 differ a lot from those. These last cycles also present less nonlinearity on the first part, while the cycle 30 curve is the most linear. Moreover, the maximum relative variation in cycle 30 is around 0.8%, and in cycle 20, 0.9%, while in Bar 3, they are 0.3% and 0.5%, respectively, which represents a significant variability. Thus, in both cases, the highest variations occur with 20 cycles of preloading.

Figure 7.21 shows the results for Bar 1, where the fastest longitudinal mode could be considered.

Figure 7.21 – Compression – 20 mm – P14 – Influence of preload in Bar 1

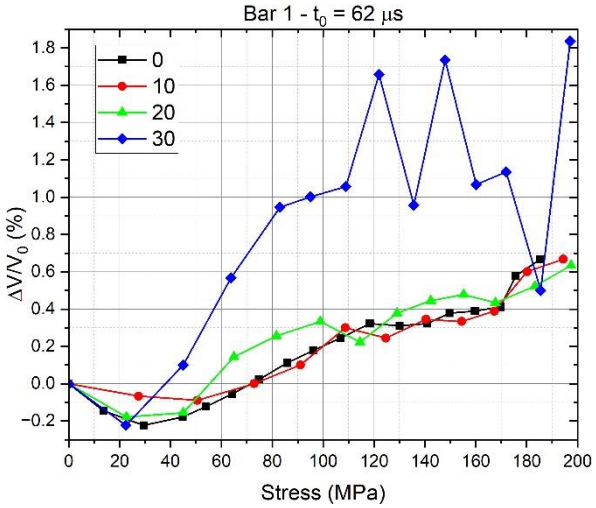

Source: Own elaboration

The acoustoelastic curves of the cycles 0, 10 and 20 are almost coincident and present a maximum positive variation around 0.7%. In contrast, cycle 30 differs significantly from the others, with a much bigger initial slope and a great variability from 100 MPa. This is due to the very small values of the cross-correlation, from 80% to 40%, and the abnormal behavior of the intercorrelation function. Figure 7.22 shows the

intercorrelation function of Cycle 0 and 30. While in Cycle 0 the functions are very regular, in Cycle 30, they are very irregular.

Figure 7.22 – Compression – 20 mm – P14 – Intercorrelation function in Bar 1

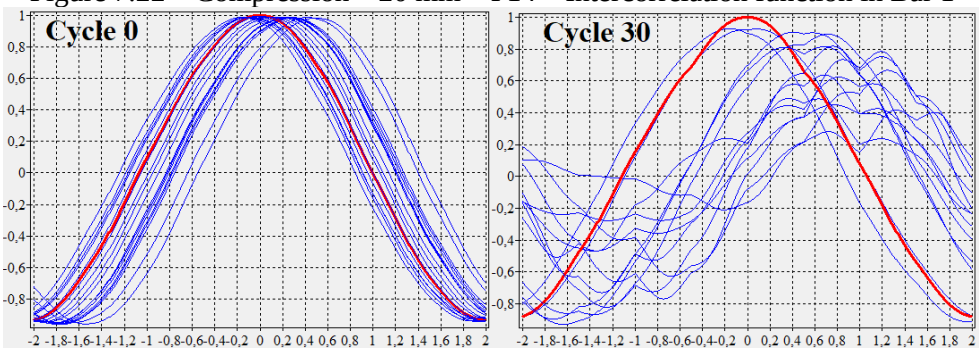

Source: Own elaboration

Disregarding cycle 30 in Bar 1 and considering cycle 30 of Bar 4, which is the only case apart from Bar 1 where it is possible to analyze the time window with $t_0 = 62\ \mu s$, Figure 7.23 is obtained.

Figure 7.23 – Compression – 20 mm – P14 – Acoustoelastic curves of Bar 1 and Bar 4

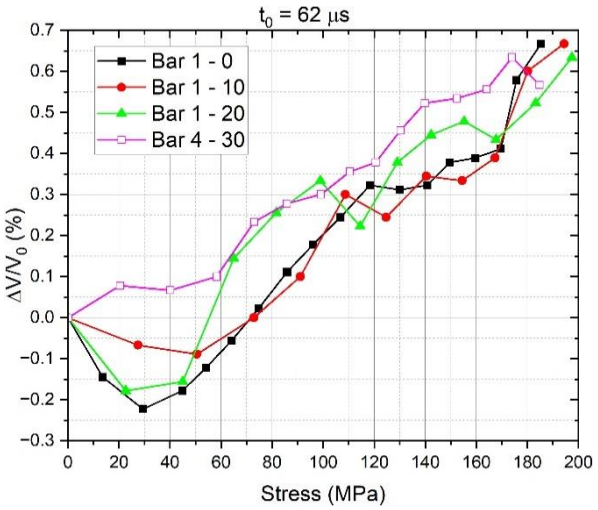

Source: Own elaboration

All curves present similar behavior, with the same maximum positive variation, around 0.65%. Moreover, the curve of Bar 4 does not have the initial nonlinear portion and is more linear than the others, mostly because it corresponds to cycle 30.

Thus, it is important to apply preloads in the element before the experiment, as well as concluded by Bompan (2021).

For prism P15, Figure 7.24 shows the curves of Bar 3, where the contact surface is constituted by a concrete layer, and Bar 4, where its surface is exposed. Prism P15 was submitted to 20 preloading cycles and the results are compared with cycle 0. It was not possible to analyze the time window corresponding to the longitudinal mode, thus $t_0 = 80\ \mu s$ is considered.

Figure 7.24 – Compression – 20 mm – P15 – Curves of Bar 3 and Bar 4

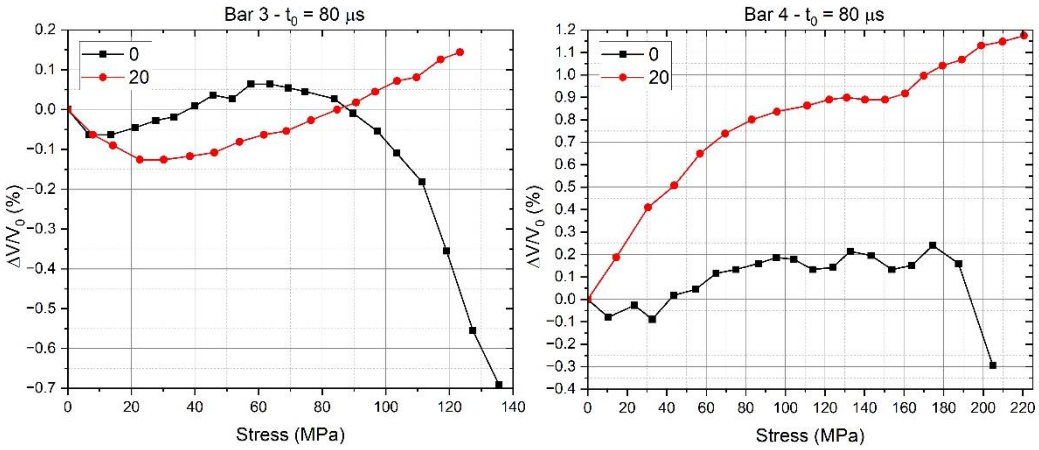

Source: Own elaboration

In both cases, the preloading makes the curves more linear and reduces variability. Only in Bar 4, the cycles eliminated the initial nonlinear portion. Additionally, the largest relative velocity variation is observed for Bar 4, where there is the cement layer, reaching around 0.9% in 120 MPa, while in Bar 3, exposed, it is 0.15%.

Finally, the curves of Bar 1 and Bar 2 are presented in Figure 7.25. Both curves have very little variation, making it difficult to conclude that this is due to acoustoelasticity.

Figure 7.25 – Compression – 20 mm – P15 – Curves of Bar 1 and Bar 2

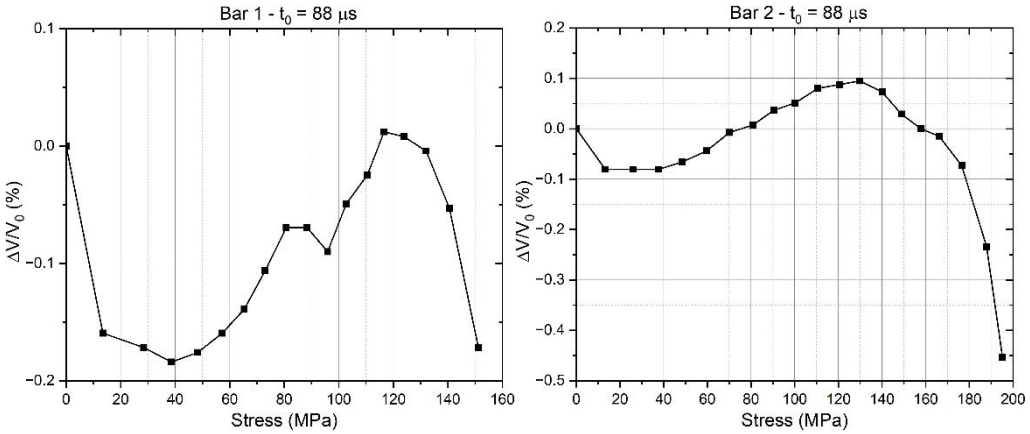

Source: Own elaboration

7.3.2 Experiments with diameters from 8 to 16 mm

Figure 7.26 shows the acoustoelastic curves of 8 mm rebar.

Figure 7.26 – Compression – 8 mm – Results of prisms P1 to P3

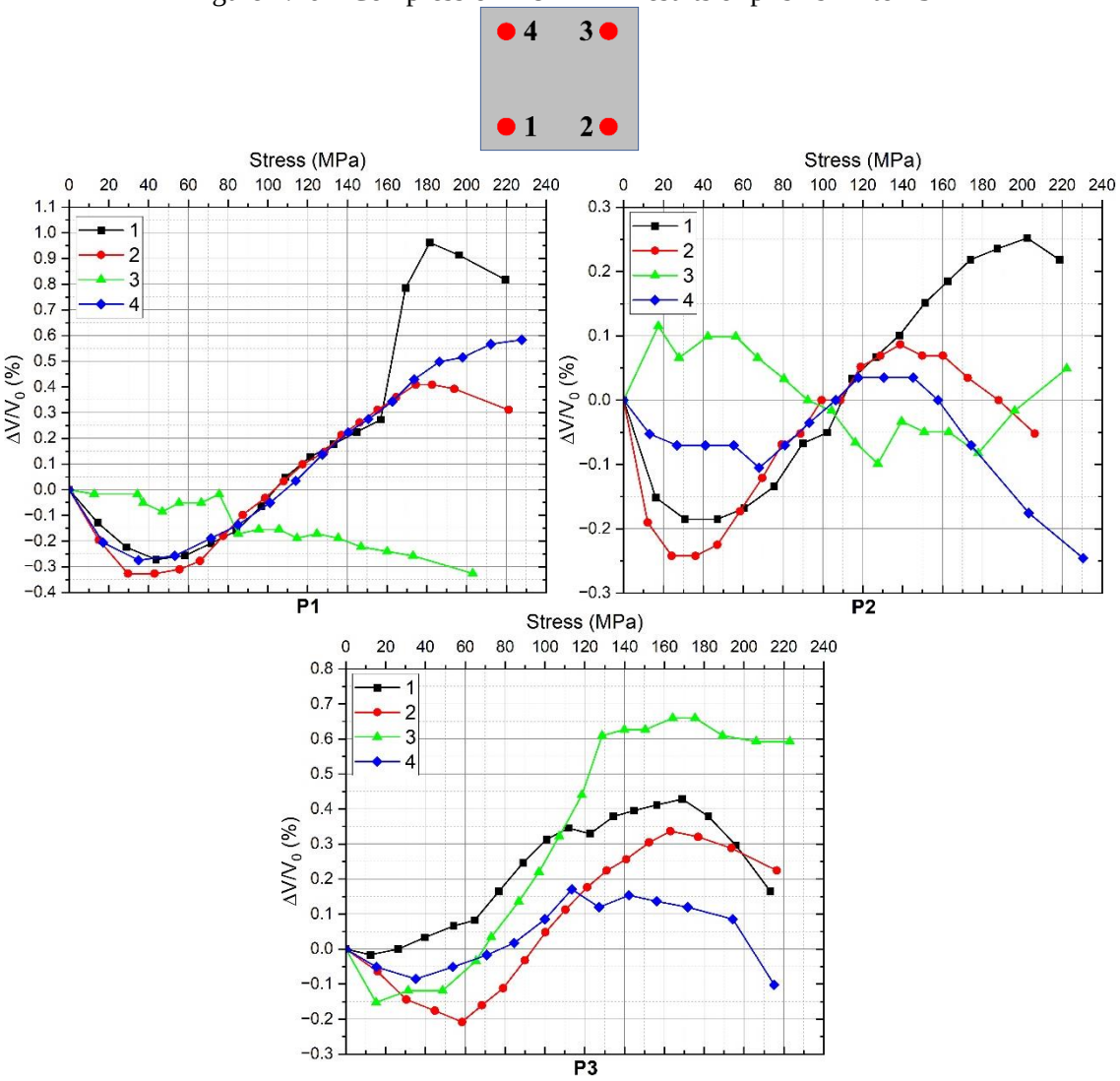

Source: Own elaboration

The most convergent results are related to P1. Except for Bar 3, all curves present an initial negative variation up to around 40 MPa, reaching -0.3%, after which there is an almost linear part with positive variation, presenting similarity until around 160 MPa. The only curve that continues the same slope until the end is Bar 4's, reaching 0.6% at 230 MPa. Considering the positive portion of this curve, it is obtained K = 4.45 x 10^{-2} GPa^{-1} and the total positive variation, from $\sigma = 35$ MPa to $\sigma = 228$ MPa, is 0.9%.

In P2, by coincidence, Bar 3 also presents a different behavior from the others, as in P1. In the other curves, there is the same behavior as in P1, an initial negative variation, reaching between -0.1% and -0.25%, and then a positive one, whose maximum variation is 0.25%, much smaller than in P1. However, the only portion of convergence occurs between 70 MPa and 120 MPa.

A similar behavior is observed in P3, with a maximum relative variation between 0.2% and 0.65%. Unlike P2, there is no agreement between curves, but they present similar slope in the range 70 – 120 MPa.

At the end portion of the curves above, their slope becomes negative again. This phenomenon is also observed in P1, but it is more pronounced in P2 and P3. Figure 7.27 shows, on the left side, the acoustoelastic curves of P2, the same as above, and, on the right side, the corresponding stress variation between load steps. Due to the anomalous behavior of Bar 3's curve, it is not considered here.

Figure 7.27 – Compression – 8 mm – Stress steps in P2

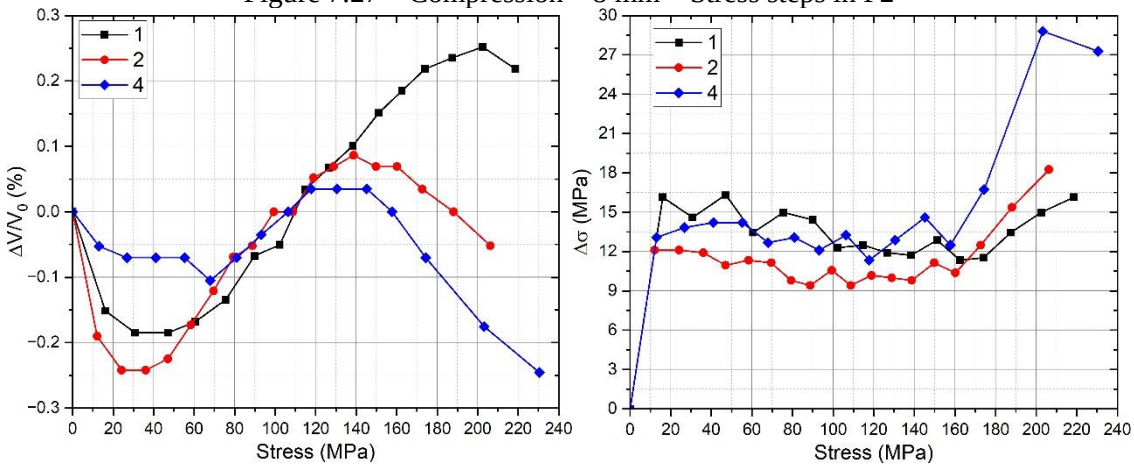

Source: Own elaboration

The stress steps present the highest values at the beginning, at low stress, presenting a slight decrease up to 160 MPa. This may justify the non-linear initial part, whereas the cracks due to preload accommodate, the rebar tends to absorb more stress. This explanation is strengthened by the fact that the experiment is controlled by load steps on the prisms instead of rebar stress steps. Moreover, as the stress steps in the case of Bar 4 are more constant than the others, its initial non-linearity in the acoustoelastic curve is smaller.

From 160 MPa, the stress steps increase significantly. This may happen due to the occurrence of new and more important cracks, which leads to a decrease at the end of the acoustoelastic curves. The smallest decrease in Bar 1 is due to the smallest stress step variation, from $\Delta\sigma = 12$ MPa to $\Delta\sigma = 16$ MPa. Conversely, in the cases of Bar 2 and 4, varying from 10 MPa to 18 MPa and from 12 MPa to 28 MPa, respectively, a great decrease is observed in the acoustoelastic curves, with similar slopes. This decrease

begins around 130 MPa, before the variation in the stress step curves, around 160 MPa. It indicates that the cracks opening is captured in early stages by the acoustoelastic effect.

Based on Figure 7.26, a Typical behavior of the acoustoelastic curve of longitudinal modes under compression is exhibited in Figure 7.28. It shows the curve of Bar 2 of P1.

Figure 7.28 – Typical acoustoelastic curve in compression

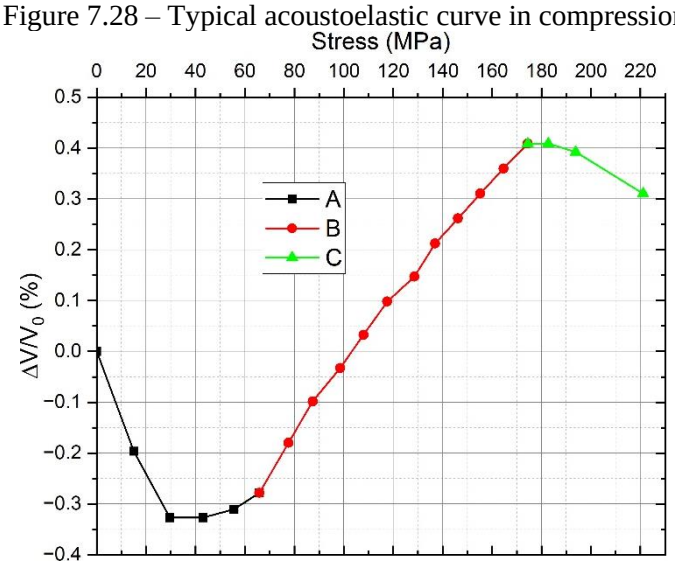

Source: Own elaboration

The curve can be divided into 3 regions:

A. The initial non-linearity due to the opening of the existing cracks, which appeared during preload. This portion consists of higher stress steps and ranges from 0 MPa to around 50 MPa.
B. The linear part, with almost constant and small stress steps. It ranges from around 50 MPa to approximately 160 MPa.
C. The last portion corresponds to the opening of new and bigger cracks. It is characterized by a negative relative velocity variation, or a plateau, higher steps, and starts around 160 MPa.

The change in the slopes of the acoustoelastic curves, at the beginning and end, shows that the longitudinal modes of guided waves are very sensitive to cracking and consequently to the boundary conditions of the guide; rebars in this case.

The acoustoelastic curves of 10 mm are presented in Figure 7.29.

Figure 7.29 – Compression – 10 mm – Acoustoelastic curves

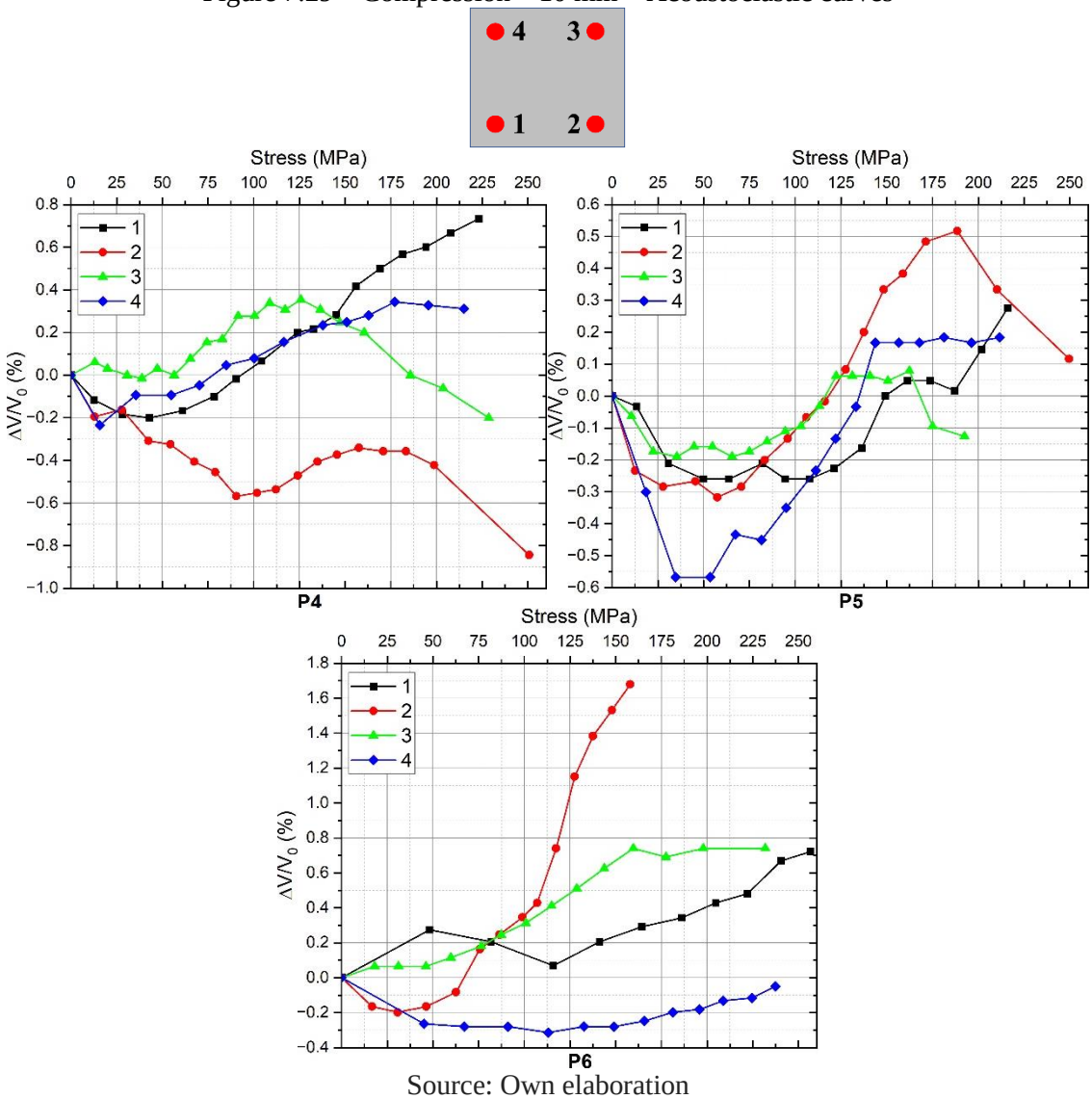

Source: Own elaboration

In P4, with exception of Bar 2, whose curve has an abnormal behavior, the other curves have similar slopes between 50 MPa and 125 MPa. In this range, $K = 5 \times 10^{-2}$ GPa^{-1} for Bar 1, 5.1×10^{-2} GPa^{-1} for Bar 3 and 3.9×10^{-2} GPa^{-1} for Bar 4. Besides, the maximum positive variation occurs with Bar 1, 0.7%, while for Bar 3 and 4, it is around 0.4%.

In P5, the curves of Bar 1 and 3 shows a great variability, while those of Bar 2 and 4 present similar slopes between 50 MPa and 130 MPa, whose $K = 5.7 \times 10^{-2}$ GPa^{-1} and 6.7×10^{-2} GPa^{-1}, respectively. In addition, the maximum positive variation occurs in the case of Bar 2, 0.5%, while in the case of Bar 4, it is 0.2%. Nonetheless, if the entire positive slope is considered, the total positive variation of both cases is similar, around 0.8%.

The results with P6 presented the biggest variability. Nevertheless, the curves of Bar 1 and 3 have a total positive variation of 0.7%, which is consistent with P5.

Furthermore, the results of Bar 3 are the best approach of the typical acoustoelastic curve presented in Figure 7.28. The unusual behavior of the curves of Bar 1 and 4 may be the result of great initial cracks, which lead to very big stress steps, almost 50 MPa. In Bar 1, these steps go up to approximately $\sigma = 120$ MPa, and in Bar 4, up to $\sigma = 50$ MPa.

Finally, Bar 2 of P6 presents the greatest positive slope among the results with 10 mm rebar, reaching 2% of total positive variation, much bigger than the others. Figure 7.30 shows the wave profiles of each load step, in the analyzed time window.

Figure 7.30 – Compression – 10 mm – Wave profiles of P6/Bar 2

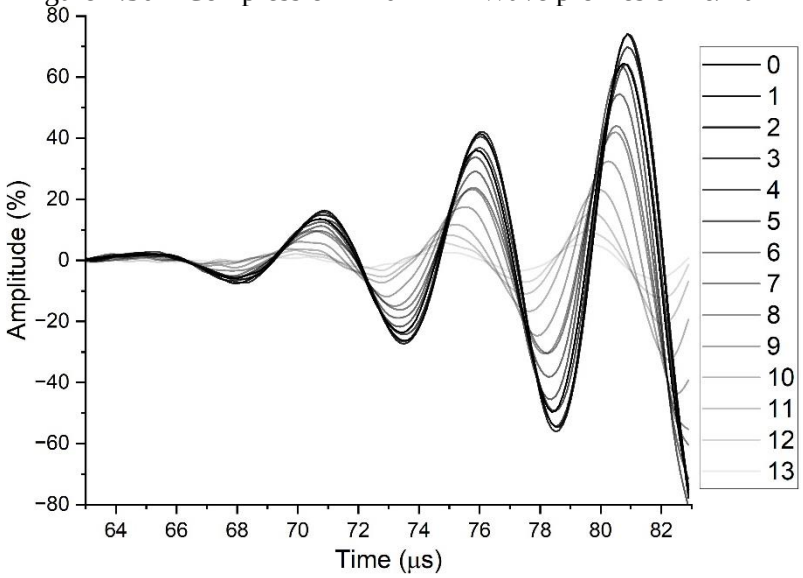

Source: Own elaboration

The higher the stress on the bar, the smaller the amplitude of the profile. The decrease in the profile indicates that as the load increases, more wave energy leaks to the concrete, transforming guided waves into bulk waves. These bulk waves will be captured later by the transducer, outside the time window of Figure 7.30, and do not contribute to the analyzed profile.

The energy leakage increases as the load increases. This is due to a greater increase in the bonding between rebar and concrete compared to the increase in cracking around the rebar during the experiment, which results in higher stress at the interface between materials. Moreover, as the test ended up at 160 MPa, Part C of the curve does not exist.

The amplitude decrease is also observed when one peak on the wave profile is compared with stress. For this, the third peak of each measurement of P6/Bar 2 is considered, within the range 74 – 78 μs. Figure 7.31 illustrates the chosen time window.

Figure 7.31 - Compression - 10 mm - Analyzed peaks of P6/Bar 2

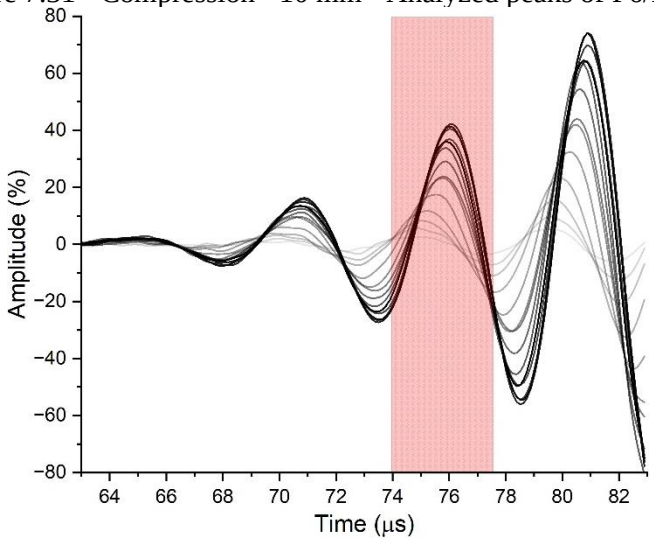

Source: Own elaboration

Figure 7.32 exhibits the relationship between stress and amplitude on the left side. On the right side, the relative amplitude is related to the corresponding relative velocity variation with the trendline in red.

Figure 7.32 – Compression – 10 mm – P6/Bar 2 amplitude analysis with stress (a) and relative velocity variation (b)

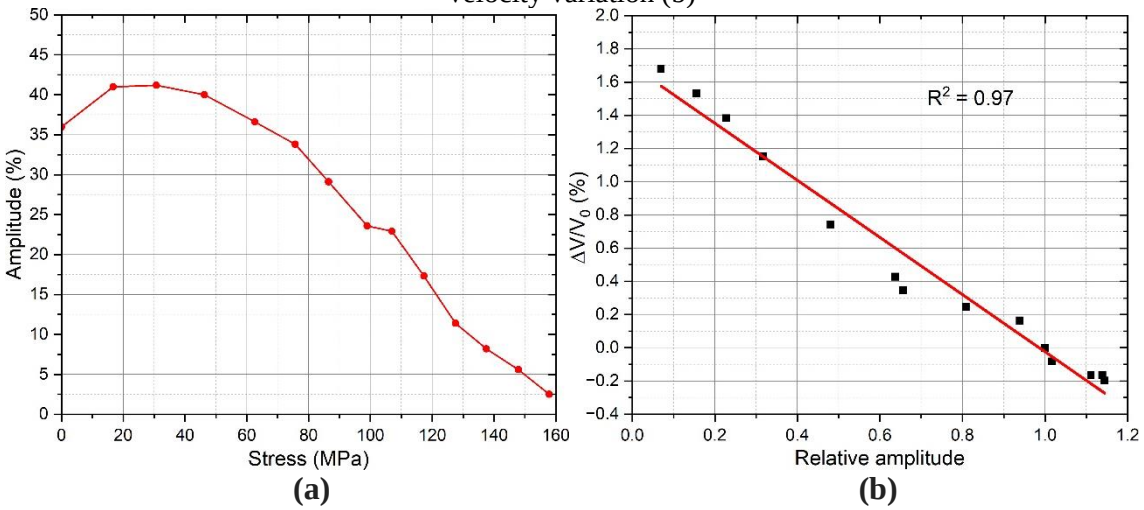

Source: Own elaboration

The leakage phenomenon is confirmed in Figure 7.32(a), whose amplitude decreases 40 percentage points in $\Delta\sigma = 160$ MPa. Moreover, the relative amplitude presents a linear variation with the relative velocity variation, presenting a slope of -1.72%. It means that 10% of decrease in the amplitude leads to 2% of relative velocity variation.

Finally, these analyses are also done for the other rebars of P6, as shown in Figure 7.33. For the tredline, the results of Bar 3 were neglected due to the abnormal behavior compared to the others.

Figure 7.33 – Compression – 10 mm – Acoustoelastic curves of P6 (a), its corresponding amplitude analysis with stress (b) and relative velocity variation (c) and trendline related to velocity variation (d)

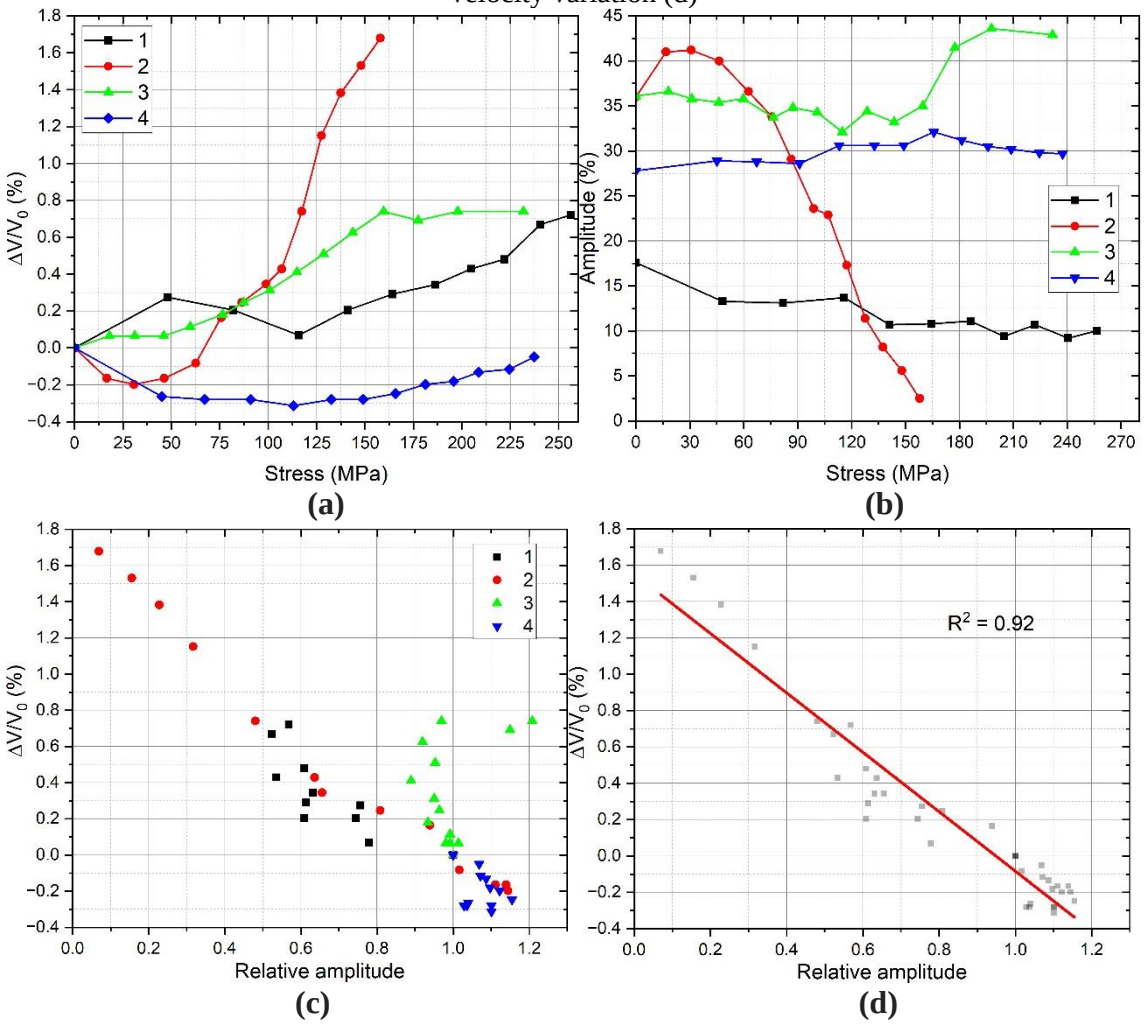

Source: Own elaboration

Different from Bar 2, the amplitude of the other rebars does not exhibit a clear tendency with stress and present minimal variation. Moreover, the amplitude variation

has no direct relation with the corresponding acoustoelastic curve, except with Bar 2, whose curves are mirrored. Nonetheless, when the relative velocity variation is compared to the corresponding relative amplitude (see Figure 7.33cd), an inversely proportional and linear relationship is observed, with a slope of -1.64%.

The acoustoelastic curves of 12.5 mm rebars are shown in Figure 7.34. In 83% of the cases, it was not possible to detect the wavefront arrival of guided wave, and the analyzed window begins at 70 μs. As seen in Item 6.3, the first bulk wave reflections influence the results. Only in Bar 1 of P8, it was possible to capture wave arrival around 60 μs, while in Bar 2 of P8, the window starts at 76 μs.

Figure 7.34 – Compression – 12.5 mm – Acoustoelastic curves

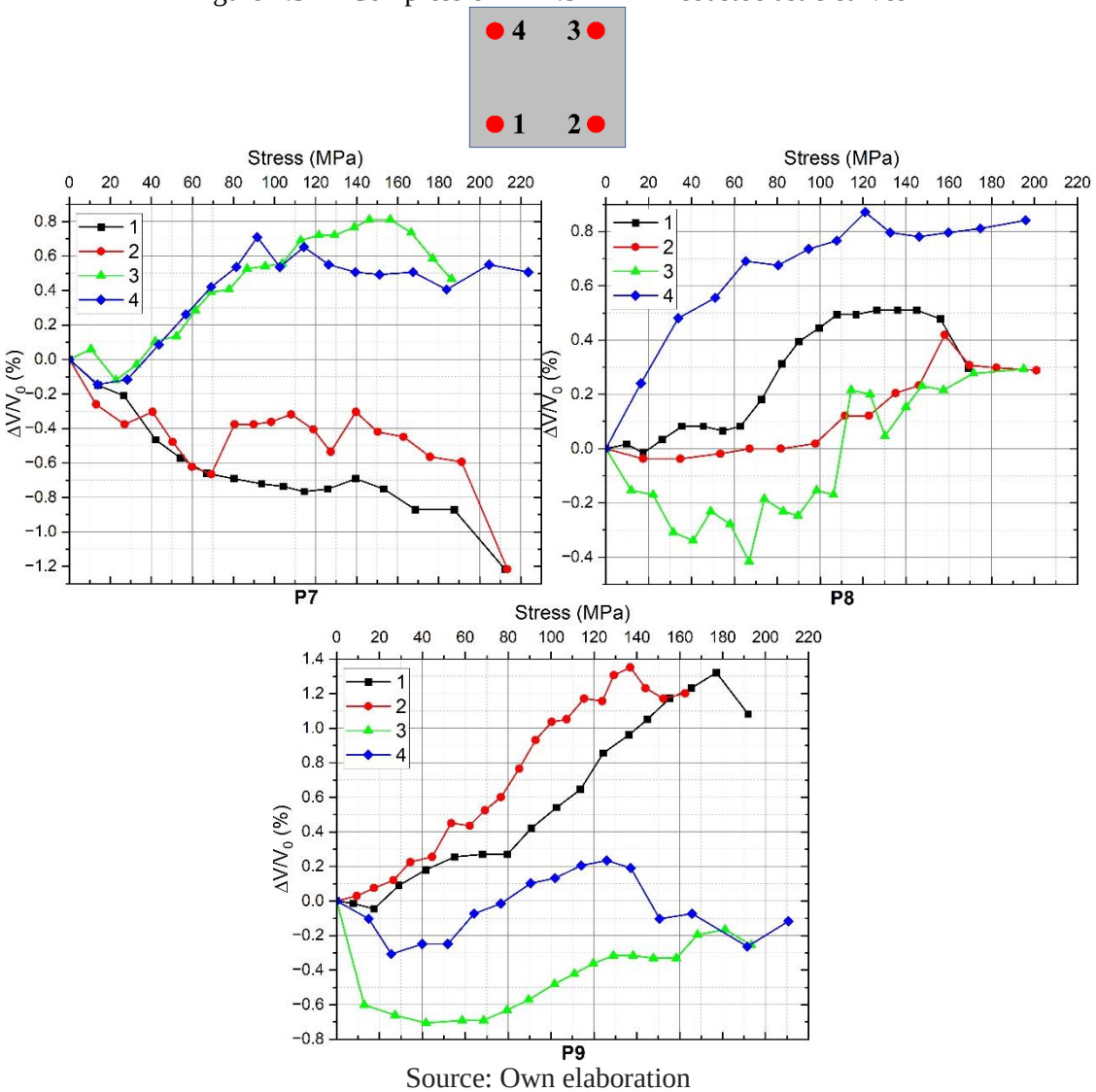

Source: Own elaboration

In P7, Bar 3 presents the most consistent result with the typical curve, with a total variation of 0.9%, while Bar 4 is early influenced by the changes in boundary conditions. In contrast, as with rebars under tension, Bar 1 and 2 have a negative variation tendency, reaching -1.2%.

Figure 7.35 shows the wave profiles of Bar 1/P7 for each load step, in the analyzed time window.

Figure 7.35 – Compression – 12.5 mm – Wave profiles of P7/Bar 1 by load steps

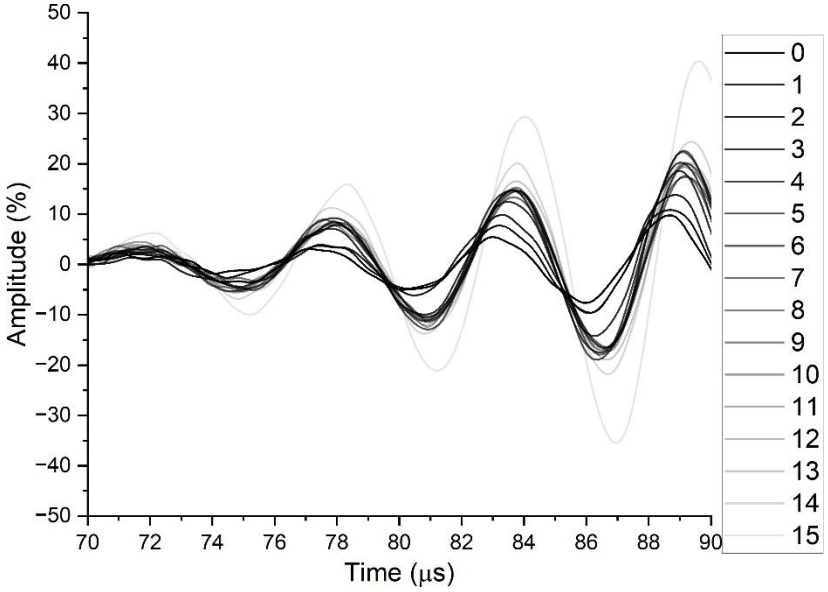

Source: Own elaboration

The profiles amplitudes increase with stress, which is the opposite phenomenon of Bar 2 of P6, with rebar of 10 mm, shown in Figure 7.30. In the case of P7, the cracking has more influence than the bonding, because as cracking increases, there is less leakage of guided waves into concrete, which makes the captured energy higher. The results with 10 mm and 12.5 mm show that the higher bonding makes the acoustoelastic curve vary positively, while cracking, negatively.

In P8, Bar 4 presents a good approach to Bar 3 and 4 of P7 in terms of total variation. Different behavior is shown in the other cases, where there is a long nonlinear portion.

Finally, in P9, Bar 1 and 2 present high positive variation, 1.3%, with a despicable non-linear initial behavior. While the curves of Bar 3 and 4 almost do not have any tendency.

Figure 7.36 presents the results of 16 mm.

Figure 7.36 – Compression – 16 mm – Acoustoelastic curves

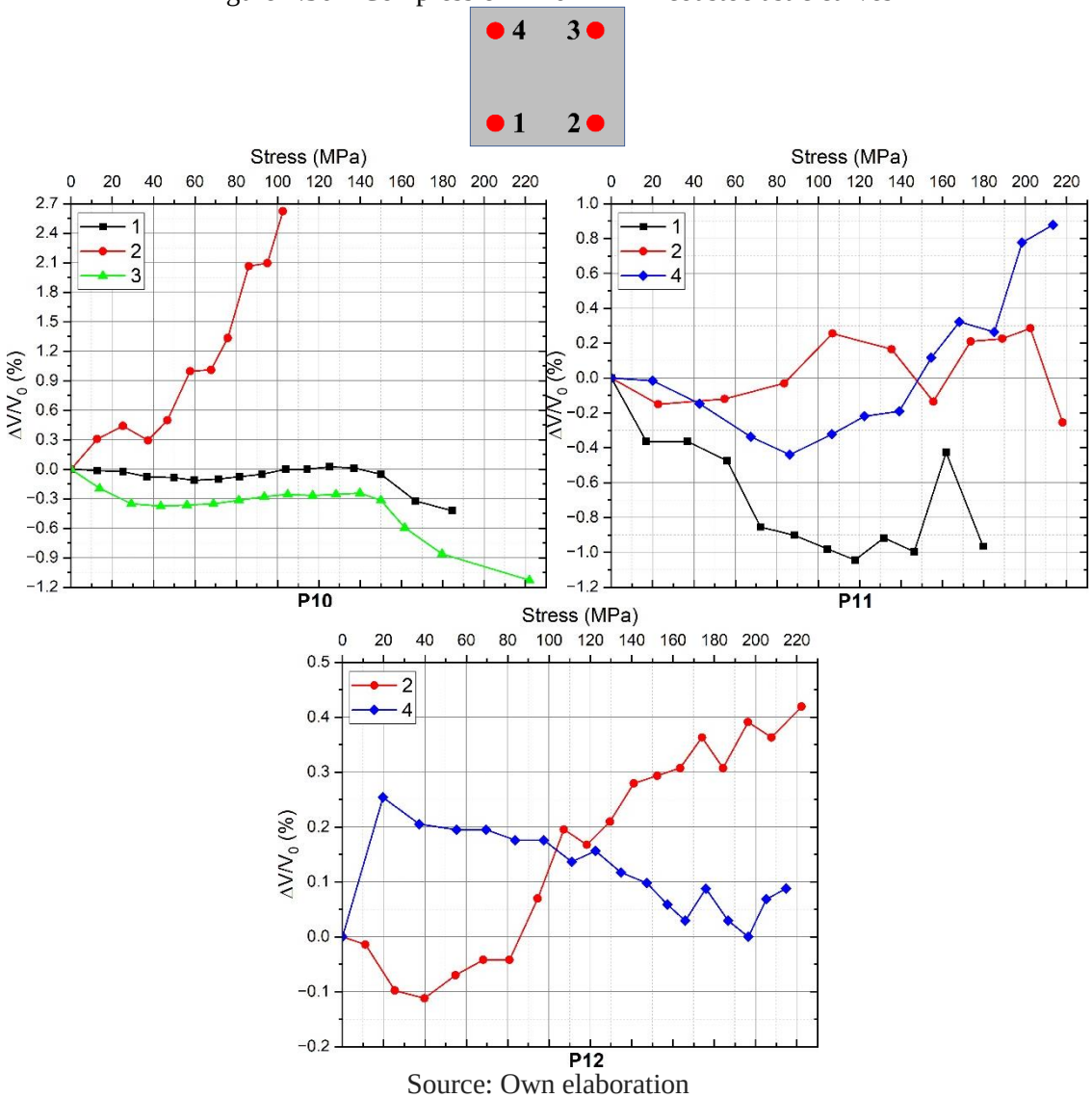

Source: Own elaboration

In no case, it was possible to detect the guided wave arrival around 60 μs. The first waves were captured within a range from 72 μs to 89 μs, whose window ended up at 92 μs and 109 μs, respectively. As seen in item 6.3, there are too many reflections on this window, which makes the analysis of guided waves impossible.

In the range above, the intercorrelation function yielded low values. Moreover, as there is significant influence from bulk wave reflections on the wave profile and the cracking level is directly proportional to the rebar diameter, the cracking influence is

greater with a 16 mm diameter rebar, and less energy arrives at the rebar. Thus, the higher the stress, the lower the signal amplitude.

Therefore, no conclusion about guided waves can be made with rebars of 16 mm diameter.

7.3.3 Tendency of acoustoelastic curves in compression

In a real structure, there is practically no additional crack opening under service loads, with a cracking pattern that remains approximately constant, disregarding chemical deterioration. Therefore, there is an almost constant level of cracking after a certain period of use and the acoustoelastic curve of a rebar can be considered linear within the service stress range. Furthermore, this curve may be considered as an average of the positive curves obtained from the prisms, since they have different cracking degrees, either above or below that of the real structure.

A tendency is observed among the curves in the prisms with 8 and 10 mm rebars, as shown in Figure 7.37. This tendency only occurs with these diameters because it was possible to capture the guided wave arrival time at $t_0 = 60\,\mu s$ in all corresponding prisms. In this figure, there are the acoustoelastic curves on the left and the respective trendline on the right. For the trendline, the final negative slope and the almost vertical part of P1/Bar 1 are disregarded.

Figure 7.37 - Representative acoustoelastic curve in compression

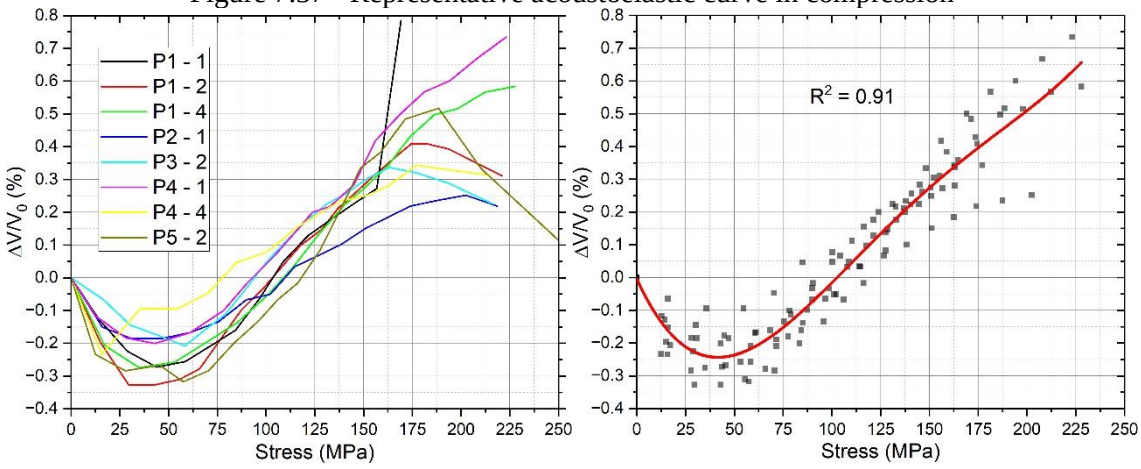

Source: Own elaboration

The curves have a similar behavior to the typical one shown in Figure 7.28, with an initial non-linear portion up to around 50 MPa, then an almost linear part until around 160 MPa, from which there is a negative slope due to cracking.

The trendline is obtained through a polynomial curve of order 4 and R^2 = 0.91. It has an initial non-linear part with a minimum variation of -0.25% and then a linear positive variation with a maximum value of 0.65%. Thus, in the range of 50 – 225 MPa, $\Delta\sigma$ = 175 MPa, the total relative velocity variation is 0.9%, which corresponds to an acoustoelastic coefficient of K = 5.1 x 10^{-2} GPa^{-1}.

7.4 PRISMS UNDER BENDING

In this section, the results in prisms under bending are discussed. One pilot test was conducted in specimens with rebars of 20 mm, then the main experiments with diameters of 8, 10, 12.5 and 16 mm were carried out.

7.4.1 Pilot test in specimens with 20 mm

After the compression tests, the same prims were subjected to bending tests, except for P13, which failed during the compression tests.

Figure 7.38 presents the results with P14. Before testing, the prism was submitted to 10, 20, and 30 preloading cycles, with ultimate load limited by the visible cracks opening. In the figure, t_0 is a mean value among the profiles, whose values vary less than 5% from the average indicated. An exception to this is cycle 30 of Bar 1 and cycle 20 of Bar 3.

Figure 7.38 – Bending – 20 mm – P14 – Acoustoelastic curves

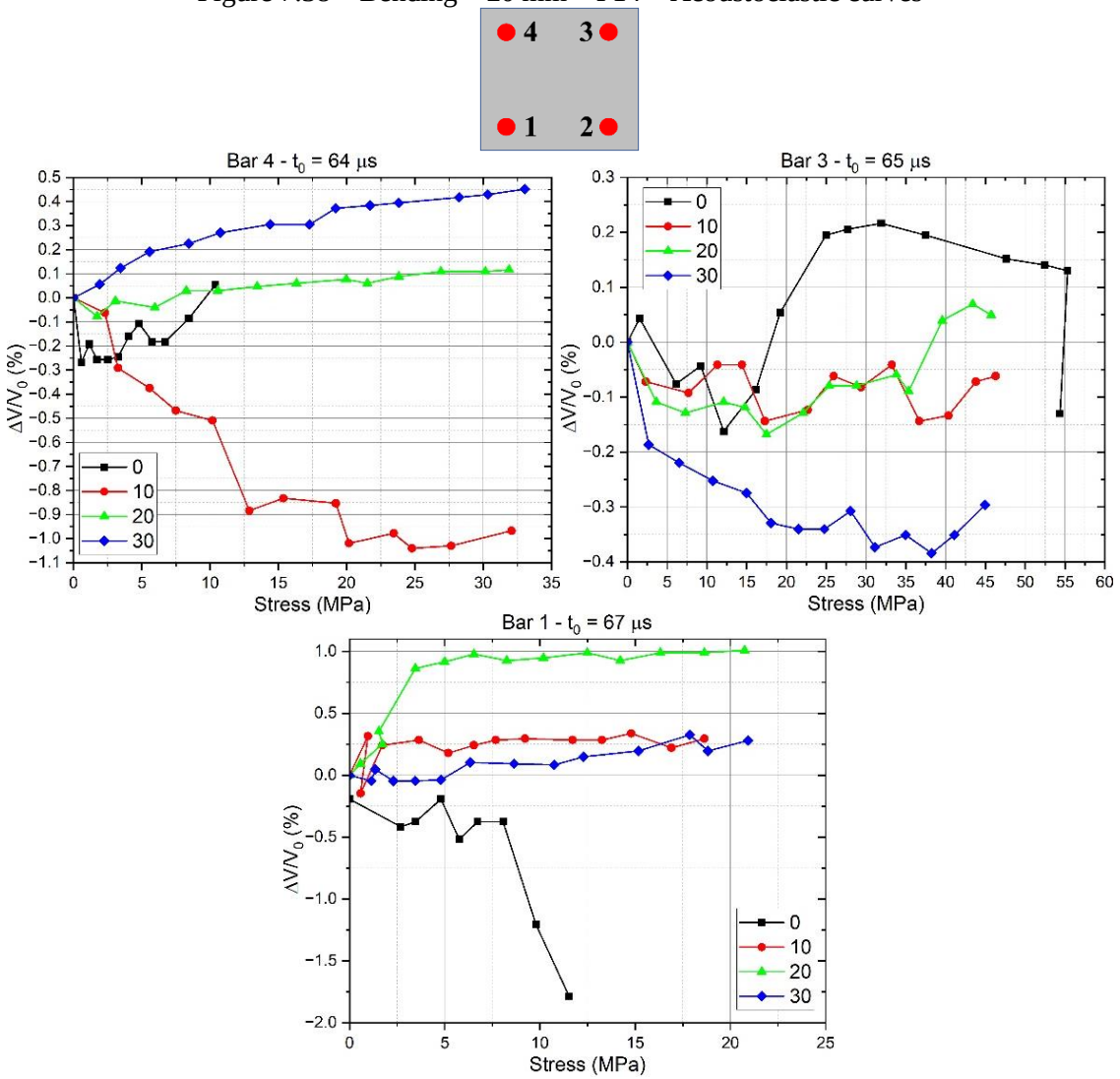

Source: Own elaboration

Based on Figure 7.9, for the isolated 20 mm bars, a linear and negative velocity variation was expected; however, this did not occur. There is no tendency in the curves, either between cycles or between bars. In some cases, the variation is positive, reaching a maximum of 1%, while in others, negative, with a minimum of -1.8%.

The low applied stress may have contributed for the absence of a tendency, which is less than 11% of the yield stress. Thus, it is necessary to evaluate the acoustoelastic effect for higher ultimate stress. The load applied was limited because of the low quantity of stirrups and the insufficient anchoring of longitudinal rebars, which led to early cracking.

The results of P15 are shown in Figure 7.39. This prism was submitted to 30 cycles of preloading.

Figure 7.39 – Bending – 20 mm – P15 – Acoustoelastic curves

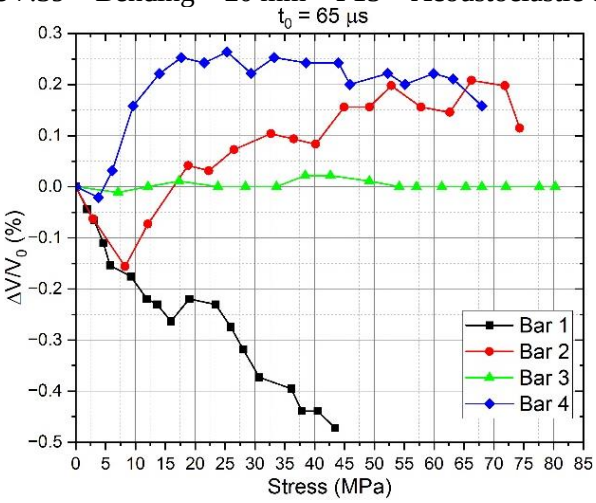

Source: Own elaboration

As verified above, there is no tendency in the curves; Bar 1 presents negative variation, while Bar 2 and 4, positive, and Bar 3 practically does not vary.

A negative variation tendency is observed when analyzing a time window along the wave profile of Bar 3, as shown in Figure 7.40 for times $t_0 = 63, 77, 124\ \mu s$.

Figure 7.40 – Bending – 20 mm – P15 – Results of different time windows in Bar 3

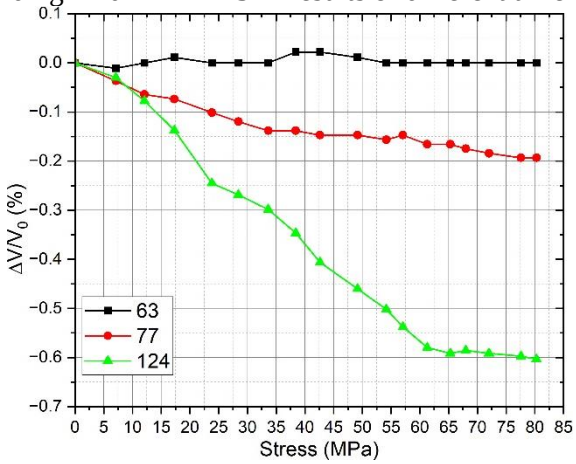

Source: Own elaboration

Figure 7.41 shows the corresponding time windows of the above curves.

Figure 7.41 – Bending – 20 mm – P15 – Time windows on the profile of Bar 3

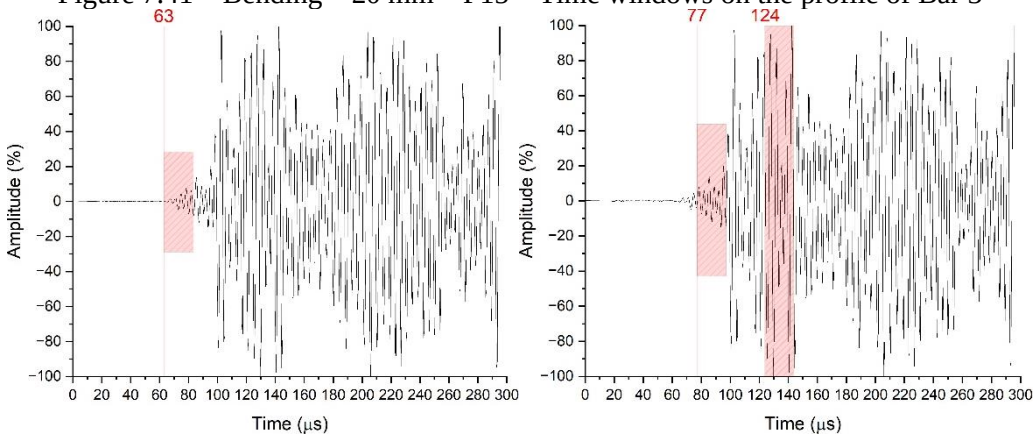

Source: Own elaboration

The time window $t_0 = 63\ \mu s$ corresponds to a wave velocity of 4476 m/s, which is compatible with the longitudinal mode of guided waves. While $t_0 = 77\ \mu s$ results in a velocity of 3662 m/s, which is approximately the shear bulk wave velocity and also corresponds to the arrival of the first longitudinal bulk wave reflection (see Section 6.4). Finally, $t_0 = 124\ \mu s$, which is around the first guided wave reflection arrival, corresponds to 2274 m/s. Therefore, these time windows indicate a superposition of different waves and reflections, making it impossible to determine the main wave within them.

Figure 7.42 shows the wave profile of P15/Bar 3, with rebar surface exposed, and P15/Bar 2, with the contact surface constituted by a cement layer. For Bar 3, a voltage of 350 V and a signal gain of 50x were used, and for Bar 2, 500 V and 500x.

Figure 7.42 – Bending – 20 mm – P15 – Wave profiles of Bar 3 (a) and 2 (b)

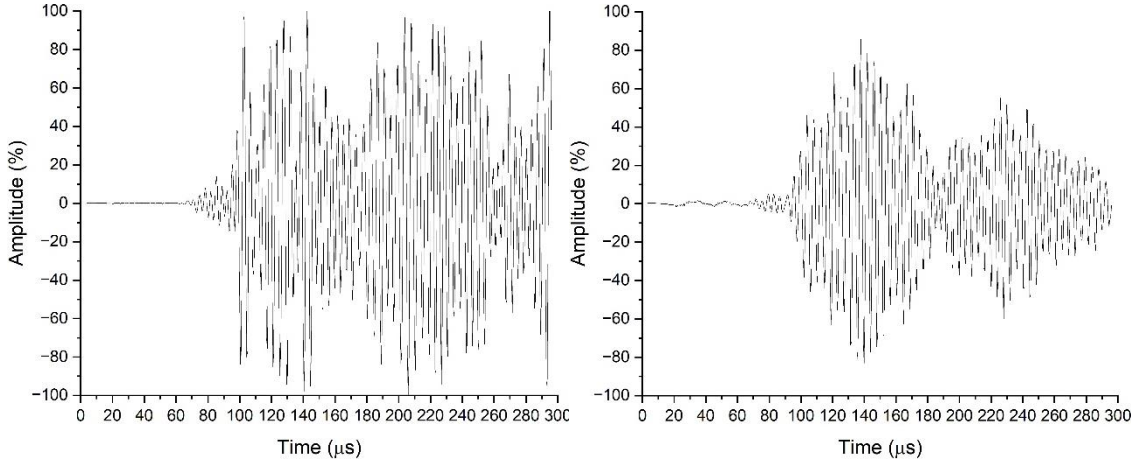

Source: Own elaboration

As was observed in compression, it is much easier to obtain the wave profile when the surface rebar is exposed. Even using a signal gain 10 times higher and a voltage almost 50% bigger, the energy in Bar 2 is lower than in Bar 3. Additionally, because of the high signal gain in Bar 2, there is a lot of signal noise at the beginning of the profile, which is mixed with the wavefront arrival.

7.4.2 Experiments with diameters from 8 to 16 mm

The results of the prisms with 8 mm are presented in Figure 7.43.

Figure 7.43 – Bending – 8 mm – Acoustoelastic curves

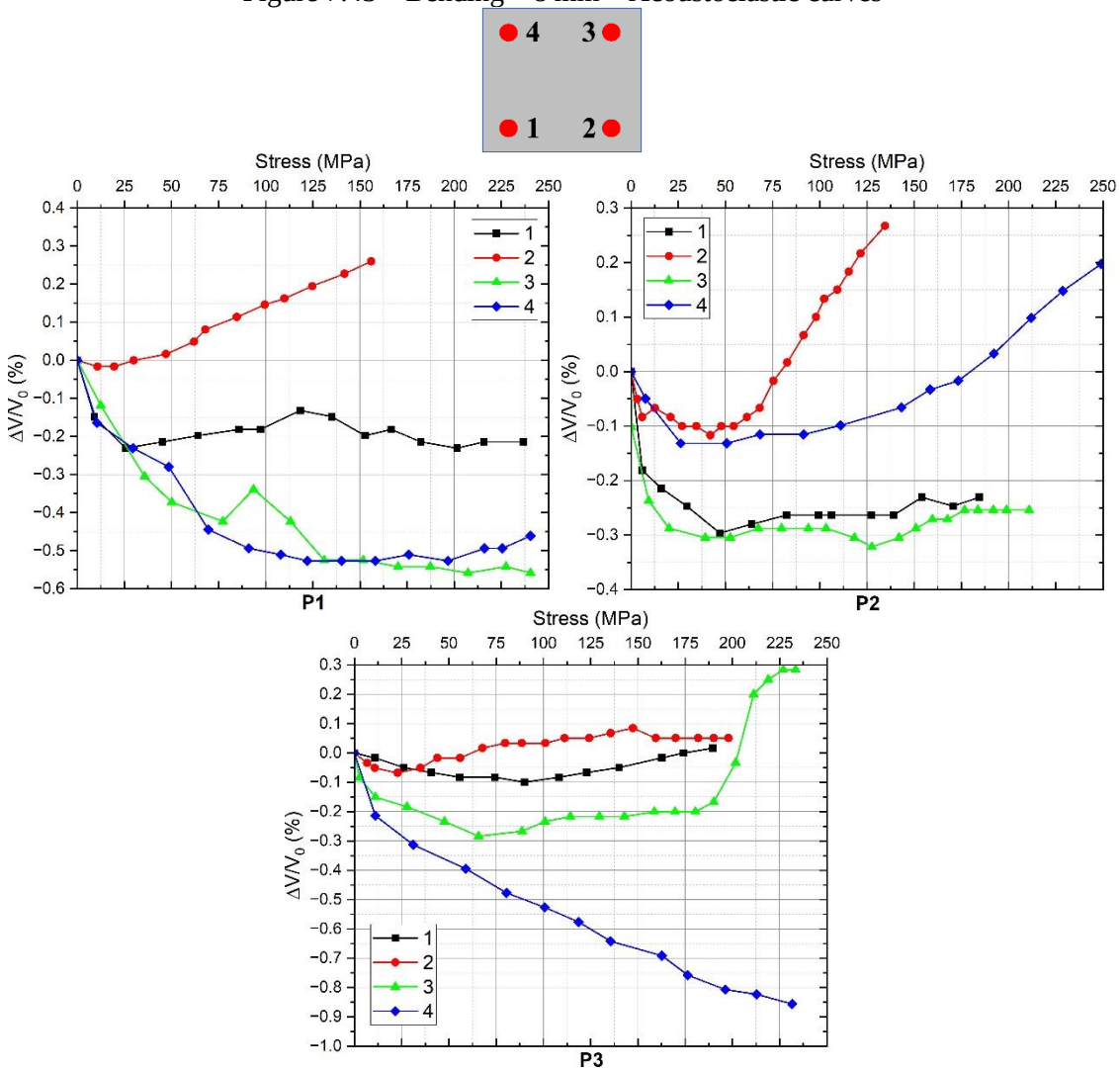

Source: Own elaboration

Some curves present positive variation, while others show negative variations. Most of them consist of long parts with negligible variation, as seen in P1/Bar 1, P2/Bar

3 and P3/Bar 1. This behavior differs from what was expected: a pattern similar to that of isolated rebars under tension, shown in Item 7.2, with a linear negative variation.

The highest variations occur in the curves with negative variation, reaching around -0.9%, in the case of P3/Bar 4, whereas the curves with positive variation reach less than 0.3%, such as P2/Bar 2.

Figure 7.44 shows the acoustoelastic curves of 10 mm rebar.

Figure 7.44 – Bending – 10 mm – Acoustoelastic curves

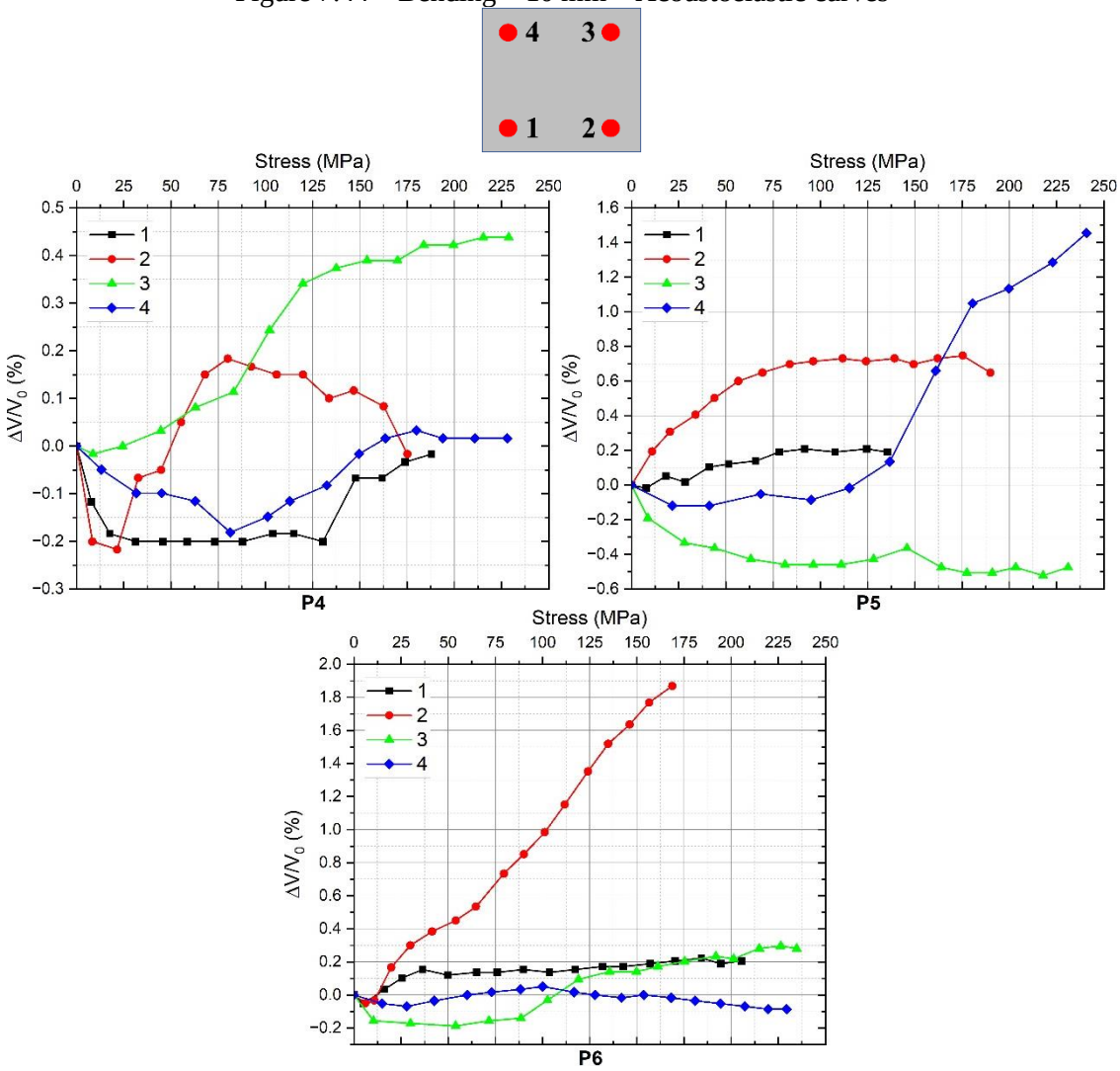

Source: Own elaboration

As in the previous case with 8 mm rebars, there is no tendency between results. However, here, the highest variations are positive, such as in P5/Bar 4, 1.4%, and in P6/Bar 2, 1.9%.

Considering the cases with the highest negative and positive variation, P3/Bar 4 (8 mm) and P6/Bar 2 (10 mm), respectively, Figure 7.45 is obtained, showing the wave profiles of each load step.

Figure 7.45 – Bending – Wave profiles of 8mm/P3/Bar 4 (a) with the corresponding magnified signal (b) and wave profiles of 10mm/P6/Bar 2 (c)

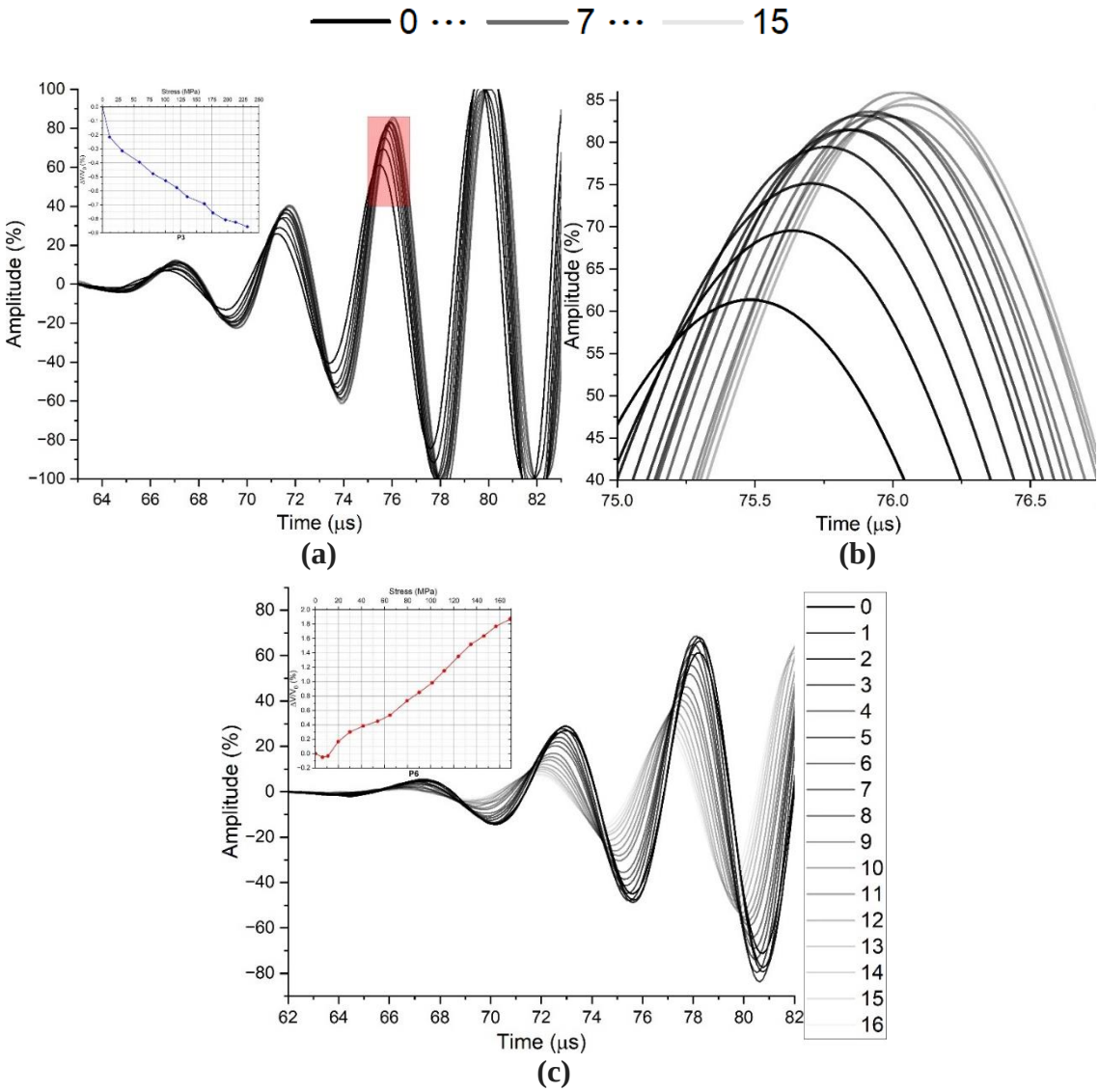

Source: Own elaboration

As seen in compression, the change in signal amplitude influences the acoustoelastic response. In P3/Bar 4 (8 mm), the increase in amplitude, due to cracking, results in a negative variation in the acoustoelastic curve, while in P6/Bar 2 (10 mm), the reduction in amplitude results in a positive variation due to bonding.

Finally, the curves of prisms with 12.5 mm rebars are presented in Figure 7.46.

Figure 7.46 – Bending – 12.5 mm – Acoustoelastic curves

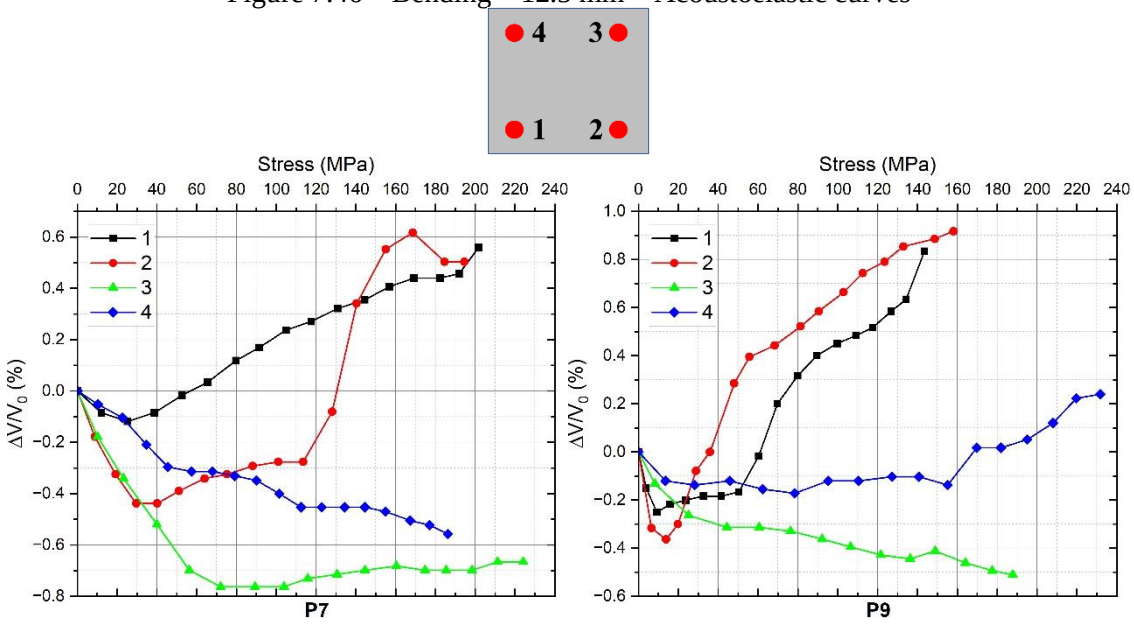

Source: Own elaboration

Following the same conclusions above, no tendency is observed in the case of 12.5 mm, presenting a maximum variation of 0.9% and a minimum of -0.8%. And different from the corresponding results in compression, in most cases, it was possible to detect waves from 60 μs and consequently to capture the guided wave wavefront arrival.

7.4.3 Tendency of acoustoelastic curves in bending

Unlike the compressive cases, where only 11% of the curves presented the main variation negative, in bending, the proportion of positive and negative variation is similar. Furthermore, a tendency is observed among the negative curves, as shown in Figure 7.47, where the acoustoelastic curves are on the left and the respective trendline is on the right.

Figure 7.47 – Bending – Representative acoustoelastic curve in bending

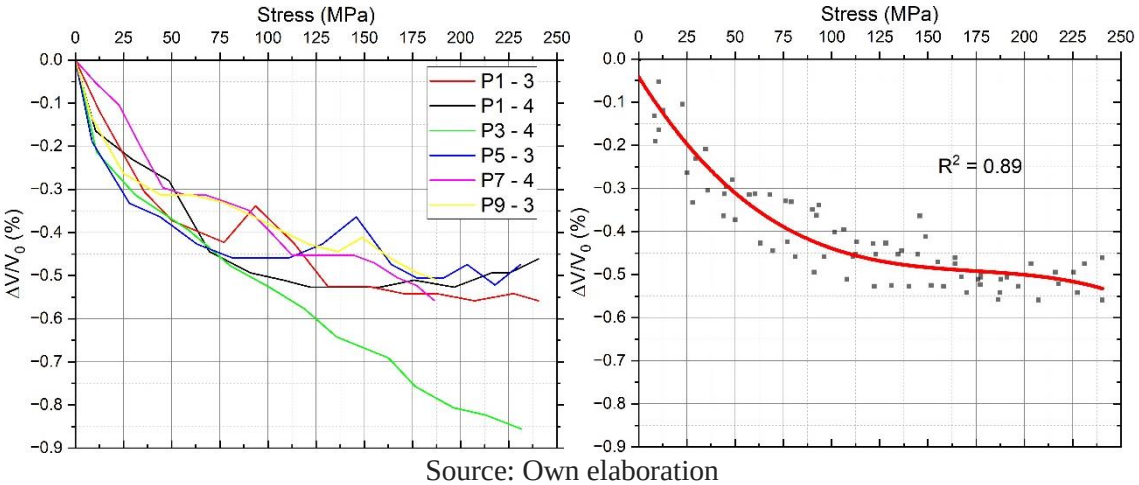

Source: Own elaboration

The acoustoelastic curve of P3/Bar 4 presents a similar behavior to the others up to 100 MPa, after which it continues linear until the end. Because of that, it is disregarded for the trendline, which is polynomial of order 3 and has R^2 = 0.89. This curve is entirely non-linear, and its maximum relative velocity variation is around -0.55%.

If these results are compared to those with isolated bars under tension, considering as reference the measurement corresponding to 50 MPa, Figure 7.48 is obtained. For this, despite the similarity between the results in isolated bars (IB) in Test 1 and 2, and to enhance figure clarity, only the first set is used.

Figure 7.48 - Comparison between isolated rebars and prims under bending

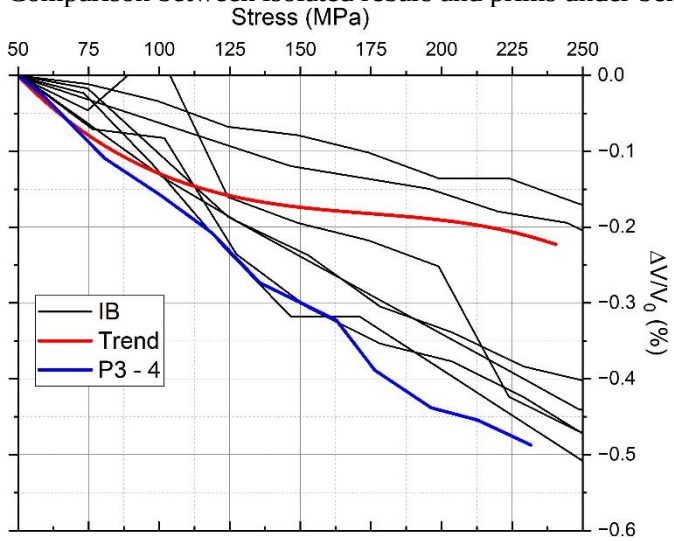

Source: Own elaboration

The increasing cracking around Bar 4 of P3 makes its curve resemble most IB's, with minimum variation around -0.5% with $\Delta\sigma \approx 200$ MPa. While the trendline has the same behavior up to 100 MPa, beyond this point, it presents a non-linearity due to the influence of the surrounding concrete and tends towards the curves of IB with the lowest variation, reaching -0.2% in $\Delta\sigma \approx 200$ MPa.

8 CONCLUSION

In the present study, acoustoelasticity was evaluated using guided waves in both isolated rebars and the rebars embedded in reinforced concrete prisms measuring 15 × 15 × 50 cm³. Ultrasound with a central frequency of 250 kHz was applied during tension tests on isolated bars and compression and bending tests on prisms. The analyzed diameters were 8, 10, 12.5, 16, and 20 mm.

For the analyses, only the longitudinal mode was used because it is the fastest wave at the analyzed frequency range. In isolated bars, only the first modes were captured: L(0,1), longitudinal, F(1,1), flexural, and T(0,1), torsional. Additionally, the higher the product of frequency and diameter, the more wave modes appear within the same frequency range. In this case, the maximum velocity is related to the first longitudinal mode, L(0,1). In the prisms, with embedded rebars, although the fastest mode is the longitudinal one, the fastest order varied with the rebar diameter.

As the diameter increases, the guided wave velocity tends to decrease; however, the wave frequency decreases, which leads to an increase in velocity. Thus, the velocity remains approximately constant across different diameters. Despite this, in prisms, the velocity tends to slightly decrease as the bar diameter increases. This is because larger diameters make it more challenging for the receiving transducer to detect the fastest guided wave. Consequently, the first detected wave arrives later on the wave profile. This effect is observed in prisms with diameters starting from 12.5 mm.

Moreover, the smaller the diameter, the lower the variance of the guided wave velocity, which results in measurements for 8 mm showing the smallest variability, while those for 16 mm exhibit the highest. This might be explained by the random nature of the cracking phenomenon, which is more prevalent with 16 mm bars.

As reference values for velocity, 4729 m/s is applicable to isolated rebars, and 4500 m/s applies to embedded bars with a 3 cm concrete cover. These values are valid for all diameters.

In the analysis of different time windows on wave profiles, the worst results for analyzing acoustoelasticity were related to time window on Coda wave, mainly due to the

low similarity between signals, which may indicate different waves. While the best results were obtained with window size of 20 μs and window initial time of 60 μs, where the main contribution is attributed to longitudinal guided waves.

In the case of isolated rebars under tension, there were some outliers in the acoustoelastic curves caused by an abnormal displacement of wave profile on the time axis, mainly the second measurements. These points are possibly a result of an initial accommodation of the transducers due to the start-up of the experiment system. Additionally, this might be influenced by the slippery contact surface and the difficulty in fixing the transducers on the bar. For this reason, it is important to disregard these outliers and consider the measurements with $\sigma = 50$ MPa as the reference for the acoustoelastic analysis.

In isolated bars under tension, the relative velocity variation is negative, and there is a linear behavior in most of them. Therefore, the acoustoelastic coefficient is K = -1.2 x 10^{-2} GPa^{-1} for diameters of 8 and 12.5 mm, and K = -2.1x 10^{-2} GPa^{-1} for diameters of 10 and 16 mm.

In prisms under compression, the elements were submitted to 0, 10, 20 and 30 cycles of preloading, wherein the maximum load was the same as the test's. There is no clear tendency in the curves with preloading cycles. Nevertheless, the higher the cycle, the greater the positive relative velocity variation, which may demonstrate the influence of preloading. Thus, applying 20 cycles of preloading or more is recommended to make the curves more linear and reduce variability.

A typical acoustoelastic curve of longitudinal modes in rebars under compression can be divided into 3 regions:

A. An initial non-linearity due to the opening of the existing cracks, which appeared during preload. This portion consists of higher stress steps and ranges from 0 MPa to around 50 MPa.
B. A linear and positive part, with almost constant and small stress steps. It ranges from around 50 MPa to approximately 160 MPa.
C. The last portion corresponds to the opening of new and bigger cracks. It is characterized by a negative relative velocity variation, or a plateau, higher stress steps, and starts around 160 MPa.

The change in the slopes of the acoustoelastic curves, at the beginning and end, shows that the longitudinal modes of guided waves are very sensitive to cracking and, consequently, to the boundary conditions of the guide; rebars in this case.

In some cases, both in compression and bending, there is a gradual change in the amplitude of the signal, either a decrease or an increase, which can significantly increase the slope of the acoustoelastic curve.

On one hand, the higher the stress on the bar, the smaller the amplitude of the profile, which increases the curve's slope positively. The decrease in the amplitude indicates that as the load increases, more wave energy leaks to the concrete, transforming guided waves into bulk waves. These bulk waves will be captured later by the transducer, outside the analyzed time window, and do not contribute to the analyzed profile. This may be due to the greater influence of bonding of the rebar compared to cracking during the experiment, which results in higher stress at the interface between materials

On the other hand, the higher the stress on the bar, the bigger the amplitude of the profile, which increases the curve's slope negatively. In this case, the cracking may have more influence than the bonding, because as cracking increases, there is less leakage of guided waves into concrete, which results in higher captured energy.

In this context, bonding makes the acoustoelastic curve to vary positively, while cracking, negatively.

There is an inversely proportional and linear relationship between the relative velocity variation and the corresponding relative amplitude, considering the third peak of the signal on the analyzed time window in this study.

There is great variability among the curves in compression; however, a tendency is observed in the prisms with 8 and 10 mm rebars. The trendline is obtained through a polynomial curve of order 4 and R^2 = 0.91. It has an initial non-linear part with a minimum variation of -0.25%, followed by a linear positive variation with a maximum value of 0.65%. Thus, in the range of 50 – 225 MPa, $\Delta\sigma$ = 175 MPa, the total relative velocity variation is 0.9%, which corresponds to an acoustoelastic coefficient of K = 5.1 x 10^{-2} GPa^{-1}.

In prisms under bending, unlike the compressive cases, where only 11% of the curves presented the main variation negative, the proportion of positive and negative variation is similar. Furthermore, a tendency is observed among the negative curves, whose trendline is polynomial of order 3 and has R^2 = 0.89. In addition, it is entirely non-linear, and its maximum relative velocity variation is around -0.55%.

If the trendline in bending is compared to the results with isolated bars under tension, considering as reference the measurement corresponding to 50 MPa, it is found that the trendline has the same behavior up to 100 MPa, beyond this point, it presents a non-linearity due to the influence of the surrounding concrete and tends towards the lowest variation curves of isolated bars, reaching -0.2% in $\Delta\sigma \approx$ 200 MPa.

Finally, the initial hypothesis that it would be possible to isolate the acoustoelastic effect of the embedded rebars by applying the transducers directly on the rebar surface was not confirmed. It was not possible to eliminate the influence of the surrounding concrete, as the guided waves are highly sensitive to the boundary conditions.

Despite the trends observed in embedded rebars under compression and tension, there was significant variability in the results due to the influence of the concrete. As a result, it was not possible to define reference acoustoelastic curves for use in real structures.

REFERENCES

AHMAD, F. A simple formula for the longitudinal modes in a cylinder. **The Journal of the Acoustical Society of America**, v. 115, n. 2, p. 475-477, Jan. 2004.

ANDREUCCI, R. **Ensaio por ultrassom**. São Paulo: ABENDI, 2018. Disponível em: https://www.abendi.org.br/abendi/Upload/file/biblioteca/apostila_us_2018.pdf. Acesso em: 18 out. 24.

ASEEM, A.; NG, C. T. Collinear nonlinear guided wave mixing for debonding detection in reinforced concrete beam using longitudinal and torsional wave modes. **Construction and Building Materials**, v. 401, p. 1-15, 2023.

ASEEM, A.; NG, C. T. Debonding detection in rebar-reinforced concrete structures using second harmonic generation of longitudinal guided wave. **Ndt & E International**, v. 122, p. 1-12, 2021.

ASSOCIAÇÃO BRASILEIRA DE NORMAS TÉCNICAS. **NBR 16697:** cimento Portland: requisitos. Rio de Janeiro: ABNT, 2018.

ASSOCIAÇÃO BRASILEIRA DE NORMAS TÉCNICAS. **NBR 16889:** concreto: determinação da consistência pelo abatimento do tronco de cone. Rio de Janeiro: ABNT, 2020.

ASSOCIAÇÃO BRASILEIRA DE NORMAS TÉCNICAS. **NBR 7211:** agregados para concreto: requisitos. Rio de Janeiro: ABNT, 2022.

ASSOCIAÇÃO BRASILEIRA DE NORMAS TÉCNICAS. **NBR 12655:** concreto de cimento Portland: preparo, controle, recebimento e aceitação: procedimento. Rio de Janeiro: ABNT, 2022.

ASSOCIAÇÃO BRASILEIRA DE NORMAS TÉCNICAS. **NBR 6118:** projeto de estruturas de concreto: procedimento. Rio de Janeiro: ABNT, 2024.

ASSOCIAÇÃO BRASILEIRA DE NORMAS TÉCNICAS. **NBR 7480: Aço destinado às armaduras para estruturas de concreto armado - Requisitos**. Rio de Janeiro, 2024.

BARR, A. D.; RIGBY, S. E.; CLAYTON, M. Correction of higher mode Pochhammer–Chree dispersion in experimental blast loading measurements. **International Journal of Impact Engineering**, v. 139, p. 1-8, May 2020.

BASTOS, P. S. **Flexão normal simples:** vigas. Bauru: Universidade Estadual Paulista, 2023. Disponível em: https://wwwp.feb.unesp.br/pbastos/concreto1/FlexaoSimples.pdf. Acesso em: 12 jul. 24. Lecture notes.

BOCCHINI, P.; MARZANI, A.; VIOLA, E. Graphical user interface for guided acoustic waves. **Journal of Computing in Civil Engineering**, v. 25, n. 3, p. 202-210, 2011.

BOMPAN, K. F. **Avaliação do efeito acustoelástico em elementos de concreto usando a propagação de ondas ultrassônicas pelos métodos de transmissão direta e indireta**. 2021. Tese (Doutorado em Engenharia Civil (Engenharia de Estruturas)) – Escola de Engenharia de São Carlos, Universidade de São Paulo, São Carlos, 2021.

BRIZARD, D.; JACQUELIN, E.; RONEL, S. Polynomial mode approximation for longitudinal wave dispersion in circular rods. **Journal of Sound and Vibration**, v. 439, pp. 388-397, 2019.

BRIZARD, D.; JACQUELIN, E. Polynomial mode approximations for longitudinal wave dispersion in solid and hollow circular cylinders. **Journal of Sound and Vibration**, v. 523, p. 1-20, Apr. 2022.

CHEN, F.; WILCOX, P. D. The effect of load on guided wave propagation. **Ultrasonics**, v. 47, n. 1-4, p. 111–122, Dec. 2007.

CHEN, H.-L.; WISSAWAPAISAL, K. Application of Wigner-Ville transform to evaluate tensile forces in seven-wire prestressing strands. **Journal of Engineering Mechanics**, v. 128, n. 11, p. 1206–1214, Nov. 2002.

CHEN, H. *et al*. Interfacial imperfection detection for steel-concrete composite structures using NDT techniques: a state-of-the-art review. **Engineering Structures**, v. 245, p. 1-29, 2021.

CHREE, C. The equations of an isotropic elastic solid in polar and cylindrical co-ordinates their solution and application. **Transactions of the Cambridge Philosophical Society**, v. 14, p. 250, 1889.

CUI, S.; LIU, H.; MAGHOUL, P. Pile length estimation based on guided wave theory and dispersion analysis for reuse of foundations. **International Journal of Solids and Structures**, v. 283, p. 112486–112486, Nov. 2023.

DELSANTO, P. P. *et al*. Acoustoelastic effects of residual stress on the propagation of Lamb and Rayleigh waves. **AIP Conference Proceedings**, v. 497, n. 1, p. 449-454, 1999.

DODSON, J. C.; INMAN, D. J. Investigating the thermally induced acoustoelastic effect in isotropic media with Lamb waves. **The Journal of the Acoustical Society of America**, v. 136, n. 5, p. 2532–2543, Nov. 2014.

DUAN, W. *et al*. Spectral subtraction and enhancement for torsional waves propagating in coated pipes. **NDT & E International**, v. 100, p. 55–63, Dec. 2018.

EDWARDS, C. *et al*. Laser generated Rayleigh and lamb waves. **AIP Conference Proceedings**, v. 615, n. 1, p. 284-291, 2002.

ELMAIMOUNI, L. *et al*. A polynomial approach to the analysis of guided waves in anisotropic cylinders of infinite length. **Wave Motion**, v. 42, n. 2, p. 177–189, Aug. 2005.

EVERY, A. G.; SHATALOV, M. Y.; YENWONG-FAI, A. S. Progress in the analysis of non-axisymmetric wave propagation in a homogeneous solid circular cylinder of a piezoelectric transversely isotropic material. **Physics Procedia**, v. 3, n. 1, p. 473–479, Jan. 2010.

FARHIDZADEH, A.; SALAMONE, S. Reference-free corrosion damage diagnosis in steel strands using guided ultrasonic waves. **Ultrasonics**, v. 57, p. 198-208, 2015.

FERNANDES NETO, J. A. D. **Avaliação ultrassônica de elementos de alvenaria estrutural com blocos cerâmicos na ausência e presença de tensões uniaxiais de compressão**. 2023. Tese (Doutorado em Engenharia Civil (Engenharia de Estruturas)) – Escola de Engenharia de São Carlos, Universidade de São Paulo, São Carlos, 2023.

GADZHIBEKOV, T. A.; ILYASHENKO, A. V. Theoretical aspects of the application of Pochhammer-Chree waves to the problems of determining the dynamic Poisson's ratio. **Mechanics of Solids**, v. 56, p. 702-714, 2021.

GANDHI, N. *et al*. Acoustoelastic lamb wave propagation in a homogeneous, isotropic aluminum plate. **AIP conference proceedings**, v. 1335, n. 1, p. 161-168, Jan. 2011.

GANDHI, N.; MICHAELS, J. E.; LEE, S. J. Acoustoelastic Lamb wave propagation in biaxially stressed plates. **The Journal of the Acoustical Society of America**, v. 132, n. 3, p. 1284-1293, 2012.

GARCIA, E. *et al*. Novel method for the detection of onset of delamination in reinforced concrete bridge decks. **Journal of Performance of Constructed Facilities**, v. 31, n. 6, p. 04017102-1-04017102-14, Dec. 2017.

GONDIM, R. M. L.; HAACH, V. G. Monitoring of ultrasonic velocity in concrete specimens during compressive loading-unloading cycles. **Construction and Building Materials**, v. 302, p. 1-7, Oct. 2021.

GORGIN, R.; LUO, Y.; WU, Z. Environmental and operational conditions effects on Lamb wave based structural health monitoring systems: a review. **Ultrasonics**, v. 105, p. 1-15, 2020.

GRAVENKAMP, H.; BIRK, C.; SONG, C. The computation of dispersion relations for axisymmetric waveguides using the scaled boundary finite element method. **Ultrasonics**, v. 54, n. 5, p. 1373-1385, 2014.

GRÊT, A.; SNIEDER, R.; SCALES, J. Time-lapse monitoring of rock properties with coda wave interferometry. **Journal of Geophysical Research:** Solid Earth, v. 111, n. B3, p. 1-11, Mar. 2006.

GUNAWAN, A.; HIROSE, S. Boundary element analysis of guided waves in a bar with an arbitrary cross-section. **Engineering Analysis with Boundary Elements**, v. 29, n. 10, p. 913-924, 2005.

GUO, X.; ZHANG, D.; ZHANG, J. Detection of fatigue-induced micro-cracks in a pipe by using time-reversed nonlinear guided waves: A three-dimensional model study. **Ultrasonics**, v. 52, n. 7, p. 912–919, Sep. 2012.

HIRAO, M.; FUKUOKA, H.; HORI, K. Acoustoelastic effect of rayleigh surface wave in isotropic material. **Journal of Applied Mechanics**, v. 48, n. 1, p. 119–124, Mar. 1981.

HONARVAR, F.; ENJILELA, E.; SINCLAIR, A. N. An alternative method for plotting dispersion curves. **Ultrasonics**, v. 49, n. 1, p. 15–18, Jan. 2009.

HONG-YE, L.; SHEN, L. YAN, L.; CUN-FU, H.; LI-HONG, Z. Wave structure analysis of acoustoelastic Lamb waves in fiber reinforced composite lamina. **Engineering Mechanics**, v. 37, n. 8, p. 221-229, 2020.

HÖHNE, C.; PRAGER, J.; GRAVENKAMP, H. Computation of dispersion relations for axially symmetric guided waves in cylindrical structures by means of a spectral decomposition method. **Ultrasonics**, v. 63, p. 54–64, Dec. 2015.

HUGHES, D. S.; KELLY, J. L. Second-order elastic deformation of solids. Physical Review, v. 92, p. 1145-1149, 1953.

HUGHES, J. M. *et al*. Comparative evaluation of in situ stress monitoring with Rayleigh waves. **Structural Health Monitoring**, v. 18, n. 1, p. 205–215, Sep. 2018.

HUSSAIN, T.; AHMAD, F.; OZAIR, M. Zero group velocity longitudinal modes in an isotropic cylinder. **Acta Mechanica Sinica**, v. 34, n. 3, p. 475-481, 2017.

HUSSON, D. A perturbation theory for the acoustoelastic effect of surface waves. **Journal of Applied Physics**, v. 57, n. 5, p. 1562–1568, Mar. 1985.

JIANG, H. *et al.* Detecting stress changes and damage in full-size concrete t-beam and slab with ultrasonic coda waves. **Journal of Structural Engineering**, v.147, n. 9, Sept. 2021.

JONES, W. S. **Ground vibration from underground railways:** how simplifying assumptions limit prediction accuracy. 2010. Dissertation (Doctor of Philosophy) – Churchill College, Cambridge University, Cambridge, 2010.

JUNG, Y.-C. *et al*. Damage detection in concrete using Lamb waves. **Proceedings of SPIE**, v. 3995, p. 448-458, Jun. 2000.

KARI, L. Axially symmetric modes in finite cylinders-the wave guide solution. **Wave Motion**, v. 36, n. 2, p. 169–184, Aug 2002.
KATO, M. *et al*. Estimation of the stress distribution in metals using nonlinear acoustoelasticity. The Journal of the Acoustical Society of America, v. 98, n. 3, p. 1496–1504, Sept. 1995.

KE, Y.-T. *et al*. Quantitative assessment of bonding between steel plate and reinforced concrete structure using dispersive characteristics of lamb waves. **NDT & E International**, v. 102, p. 311–321, Mar. 2019.

KLEY, M. *et al*. Development of dispersion curves for two-layered cylinders using laser ultrasonics. **The Journal of the Acoustical Society of America**, v. 106, n. 2, p. 582-588, 1999.

KRAUTKRAMER, J.; KRAUTKRAMER, H. **Ultrasonic testing of materials.** 4th. ed. Berlim: Springer, 1990.

KUBRUSLY, A. C.; BRAGA, A. M. B.; WEID, J. P. Derivation of acoustoelastic Lamb wave dispersion curves in anisotropic plates at the initial and natural frames of reference. **The Journal of the Acoustical Society of America**, v. 140, n. 4, p. 2412-2417, 2016.

KUNDU, T. *et al*. C-scan and L-scan generated images of the concrete/GFRP composite interface. **NDT & E International**, v. 32, n. 2, p. 61–69, Mar. 1999.

LAMB, H. On waves in an elastic plate. **Proceedings of the Royal Society of London. Series A:** Mathematical, Physical and Engineering Sciences, v. 93, n. 648, p. 114–128, mar. 1917.

LAURENT, J. *et al*. Laser induced zero-group velocity resonances in transversely isotropic cylinder. **The Journal of the Acoustical Society of America**, v. 137, n. 6, p. 3325-3334, 2015.

LI, J. *et al*. Guided waves for debonding identification in CFRP-reinforced concrete beams. **Construction and Building Materials**, v. 131, p. 388–399, Jan. 2017.

LI, J.; SHI, W. Acoustoelastic effect analysis of Lamb wave based on finite element simulation. *In*: SYMPOSIUM ON PIEZOELECTRICITY, ACOUSTIC WAVES, AND DEVICE APPLICATIONS, 16., 2022, Nanjing. **Proceedings** […]. Piscataway: IEEE, 2022. p. 435-439.

LI, Z. *et al*. Corrosion mechanism of reinforced bars inside concrete and relevant monitoring or detection apparatus: a review. **Construction and Building Materials**, v. 279, p. 1-14, 2021.

LIAO, Z.; QIAO, P. Guided wave-based cross-scene interfacial debonding detection in reinforced concrete structures. **Measurement**, v. 223, p. 1-20, Dec. 2023.

LILLAMAND, I. *et al*. Acoustoelastic effect in concrete material under uni-axial compressive loading. **Ndt & E International**, v. 43, n. 8, p. 655-660, Nov. 2010.

LIU, H. *et al*. Wave structure analysis of acoustoelastic Lamb waves in fiber reinforced composite lamina. **Engineering Mechanics**, v. 37, n. 8, p. 221-229, 2020.

LIU, S. X.; TANG, L. G.; XU, X. M. Transient elastodynamic response of finite and infinite solid cylinders. **Applied Acoustics**, v. 73, n. 8, p. 798–802, Aug. 2012.

LOWE, M.; PAVLAKOVIC, B. **Disperse:** a system for generating dispersion curve: user's manual, version 2.0.20a. London: [*s. n.*], 2013.

LOWE, M. J. S. Matrix techniques for modeling ultrasonic waves in multilayered media. **IEEE Transactions on Ultrasonics Ferroelectrics and Frequency Control**, v. 42, n. 4, p. 525–542, Jul. 1995.

LU, Y. *et al*. Guided waves for damage detection in rebar-reinforced concrete beams. **Construction and Building Materials**, v. 47, p. 370–378, Oct. 2013.

MAHBAZ, S.; CASCANTE, G.; DUSSEAULT, M. B. De-bonding assessment of rebars using an ultrasonic method with laser vibrometer tests and numerical simulations. **NDT & E International**, v. 120, p. 1-12, Jun. 2021.

MAJHI, S. *et al*. Corrosion monitoring in steel bars using Laser ultrasonic guided waves and advanced signal processing. **Mechanical Systems and Signal Processing**, v. 149, p. 1-19, Fev. 2021.

MALHOTRA, V. M.; CARINO, N. J. **Handbook on nondestructive testing of concrete**. 2nd ed. Boca Raton: CRC Press, 2004.

MARKS, R. *et al*. Lamb wave interaction with adhesively bonded stiffeners and disbonds using 3D vibrometry. **Applied Sciences**, v. 6, n. 1, p. 1-20, Jan. 2016.

MATUSZYK, P. J. Modeling of guided circumferential SH and Lamb-type waves in open waveguides with semi-analytical finite element and perfectly matched layer method. **Journal of Sound and Vibration**, v. 386, p. 295–310, Jan. 2017.

MAZZOTTI, M. *et al*. A coupled SAFE-2.5 D BEM approach for the dispersion analysis of damped leaky guided waves in embedded waveguides of arbitrary cross-section. **Ultrasonics**, v. 53, n. 7, p. 1227-1241, 2013.

MAZÚCH, T. Powerful FE approaches for Pochhammer's dispersion modelling. **International Journal for Numerical Methods in Engineering**, v. 57, n. 4, p. 555-576, Mar. 2003.

MEITZLER, A. H. Mode coupling occurring in the propagation of elastic pulses in wires. **The Journal of the Acoustical Society of America**, v. 33, n. 4, p. 435-445, 1961.

MEHTA, P.K.; MONTEIRO, P.J.M. **Concreto:** microestrutura, propriedades e materiais. 3.ed. São Paulo: IBRACON, 2008.

MOHABUTH, M.; KOTOUSOV, A.; NG, C.-T. Large acoustoelastic effect for Lamb waves propagating in an incompressible elastic plate. **The Journal of the Acoustical Society of America**, v. 145, n. 3, p. 1221-1229, 2019.

MURNAGHAN, F. D. Finite deformation of an elastic solid. Nova York: John Wiley and Sons, 1951.

MUSTAPHA, S. *et al*. Damage detection in rebar-reinforced concrete beams based on time reversal of guided waves. **Structural Health Monitoring**, v. 13, n. 4, p. 347–358, Feb. 2014.

NA, W.-B.; KUNDU, T.; EHSANI, M. R. Ultrasonic guided waves for steel bar concrete interface testing. **Materials evaluation**, v. 60, n. 3, p. 437-444, 2002.

NA, W.-B.; KUNDU, T.; EHSANI, M. R. Lamb waves for detecting delamination between steel bars and concrete. **Computer-Aided Civil and Infrastructure Engineering**, v. 18, n. 1, p. 58–63, Jan. 2003.

NG, C. T. *et al*. Investigation of nonlinear torsional guided wave mixing in pipes buried in soil. **Engineering Structures**, v. 273, p. 1-9, 2022.

NG, C.-T. *et al*. Stress evaluation of tubular structures using torsional guided wave mixing. **Smart Structures and Systems:** An International Journal, v. 30, n. 6, p. 639-648, 2022.

OHTSU, M. Elastic wave methods for NDE in concrete based on generalized theory of acoustic emission. **Construction and Building Materials**, v. 122, p. 845–854, Sept. 30 2016.

ONOE, M. **Tables of modified quotients of Bessel functions**. New York: Columbia University Press, 1958.

ORTEGA, L.P.C et al. Introdução à avaliação de tensões por ultrassom. Rio de Janeiro: Virtual Científica, 2011.

PAO, Y.-H.; MINDLIN, R. D. Dispersion of flexural waves in an elastic, circular cylinder. **Journal of Applied Mechanics**, v. 27, n. 3, p. 513–520, Sept. 1960.

PAVLAKOVIC, B.; LOWE, M. A general purpose approach to calculating the longitudinal and flexural modes of multi-layered, embedded, transversely isotropic cylinders. *In*: THOMPSON, D. O.; CHIMENTI, D. E. (eds.). **Review of progress in quantitative nondestructive evaluation**. Boston: Springer, 1999. p. 239-246. v. 18A–18B.

PAVLAKOVIC, B. *et al*. Disperse: a general purpose program for creating dispersion curves. *In*: THOMPSON, D. O.; CHIMENTI, D. E. (eds.). **Review of progress in quantitative nondestructive evaluation**. Boston: Springer, 1997. v. 16A.

PEI, N.; BOND, L. J. Acoustoelastic Lamb wave analysis in thin plates. *In*: IEEE FAR EAST NDT NEW TECHNOLOGY & APPLICATION FORUM, 2015, Zhuhai. **Proceedings** […]. Piscataway: IEEE, 2015. p. 149-153.

PEI, N.; BOND, L. J. Experimental study of the acoustoelastic Lamb wave in thin plates. **AIP Conference Proceedings**, v. 1706, n. 1, p. 070009-1- 070009-9, Feb. 2016a.

PEI, N.; BOND, L. J. Higher order acoustoelastic Lamb wave propagation in stressed plates. **The Journal of the Acoustical Society of America**, v. 140, n. 5, p. 3834-3843, 2016b.

PEI, N.; BOND, L. J. Comparison of acoustoelastic Lamb wave propagation in stressed plates for different measurement orientations. **The Journal of the Acoustical Society of America**, v. 142, n. 4, p. EL327-EL331, 2017a.

PEI, N.; BOND, L. J. Sensitivity of higher order acoustoelastic Lamb wave in stressed plates. **AIP Conference Proceedings**, v. 36, p. 020024-1–020024-9, Jan. 2017b.

PHILIBERT, M. *et al*. Lamb waves-based technologies for structural health monitoring of composite structures for aircraft applications. **European Journal of Materials**, v. 2, n. 1, p. 436-474, 2022.

PLANÈS, T.; LAROSE, E. A review of ultrasonic coda wave interferometry in concrete. **Cement and Concrete Research.** v. 53, p. 248-255, 2013.

POCHHAMMER, L. Ueber die Fortpflanzungsgeschwindigkeiten kleiner Schwingungen in einem unbegrenzten isotropen Kreiscylinder. **Journal Für Die Reine Und Angewandte Mathematik (Crelles Journal)**, v. 1876, n. 81, p. 324-336, 1876.

PUCKETT, A. D.; PETERSON, M. L. Individual longitudinal pochhammer-chree modes in observed experimental signals. **Acoustics Research Letters Online**, v. 6, n. 4, p. 268–273, Oct. 2005.

RAJESHWARA, C. S.; BANERJEE, S.; LU, Y. Identification of zero effect state in corroded RCC structures using guided waves and embedded Piezoelectric Wafer Transducers (PWT). **Procedia Engineering**, v. 188, p. 209–216, 2017.

RAYLEIGH, L. On waves propagated along the plane surface of an elastic solid. **Proceedings of the London Mathematical Society**, v. 1, n. 1, p. 4–11, Nov. 1885.

RESENDE, R.M.L.G. Avaliação dos efeitos da danificação e da acustoelasticidade sobre a velocidade de pulso ultrassônico em elementos de concreto. 2018. Dissertação (Mestrado em Engenharia Civil (Engenharia de Estruturas)) – Escola de Engenharia de São Carlos, Universidade de São Paulo, São Carlos, 2018.

RIZZO, P.; LANZA, F. Monitoring steel strands via ultrasonic measurements. **Proceedings of SPIE**, v. 4696, p. 52-73, Jun. 2002.

RODRÍGUEZ-ROBLERO, M. J. *et al*. Application of correlation analysis techniques to surface wave testing for the evaluation of reinforced concrete structural elements. **NDT & E International**, v. 102, p. 68-76, 2019.

SADLER, J.; MAEV, R. G. Experimental and theoretical basis of Lamb waves and their applications in material sciences. **Canadian Journal of Physics**, v. 85, n. 7, p. 707–731, Jul. 1 2007.

SARAVANAN, T. J. RETRACTED ARTICLE: Investigation of guided wave dispersion characteristics for fundamental modes in an axisymmetric cylindrical

waveguide using rooting strategy approach. **Mechanics of Advanced Materials and Structures**, v. 29, n. 4, p. 495–505, Jun. 2020.

SCALEA, F. L.; RIZZO, P.; SEIBLE, F. Stress measurement and defect detection in steel strands by guided stress waves. **Journal of Materials in Civil Engineering**, v. 15, n. 3, p. 219–227, Jun. 2003.

SCOTT, D. B. Internal inspection of reinforced concrete for nuclear structures using shear wave tomography. **Energy Conversion and Management**, v. 74, p. 582-586, 2013.

SECO, F. *et al*. PCDISP: a tool for the simulation of wave propagation in cylindrical waveguides. *In*: INTERNATIONAL CONGRESS ON SOUND AND VIBRATION, 9., Orlando, 2002. **Proceedings** […]. [*S. l.: s. n.*], 2002.

SECO, F. *et al*. **PCDISP:** a tool for the simulation of wave propagation in cylindrical waveguides. Madrid: Instituto de Automática Industrial, 2011. Disponível em: https://www.researchgate.net/publication/228529485_PCDISP_a_tool_for_the_simulation_of_wave_propagation_in_cylindrical_waveguides. Acesso em: 09 mar. 24.

SECO, F.; JIMÉNEZ, A. R. Modelling the generation and propagation of ultrasonic signals in cylindrical waveguides. **Ultrasonic Waves**, v. 28, p. 1-30, 2012.

SHARMA, A. *et al*. Elastic wave based evaluation of CFRP protected RC structures subjected to corrosion. **Construction and Building Materials**, v. 287, p. 1-12, 2021.

SHARMA, S.; MUKHERJEE, A. Ultrasonic guided waves for monitoring the setting process of concretes with varying workabilities. **Construction and Building Materials**, v. 72, p. 358-366, 2014.

SHATALOV, M. Y.; EVERY, A. G.; YENWONG-FAI, A. S. Analysis of non-axisymmetric wave propagation in a homogeneous piezoelectric solid circular cylinder of transversely isotropic material. **International Journal of Solids and Structures**, v. 46, n. 3-4, p. 837–850, Feb. 2009.

SHI, W. *et al*. A baseline-free stress monitoring strategy based on acoustoelastic Lamb waves using PWAS array. **Structural Health Monitoring**, v. 22, n. 3, p. 1745-1759, 2023.

SNIEDER, R. *et al*. Coda wave interferometry for estimating nonlinear behavior in seismic velocity. **Science**, v. 295, n. 5563, p. 2253-2255, 2002.

SUN, H.; ZHU, J. Nondestructive evaluation of steel-concrete composite structure using high-frequency ultrasonic guided wave. **Ultrasonics**, v. 103, p. 106096, 2020.
TREYSSÈDE, F. Numerical investigation of elastic modes of propagation in helical waveguides. **The Journal of the Acoustical Society of America**, v. 121, n. 6, p. 3398-3408, 2007.

TUA, P. S.; QUEK, S. T.; WANG, Q. Detection of cracks in cylindrical pipes and plates using piezo-actuated Lamb waves. **Smart Materials and Structures**, v. 14, n. 6, p. 1325–1342, Oct. 2005.

VASCONCELOS, T. D. L. **Estudo da acustoelasticidade em armaduras de elementos de concreto armado**. 2022. Qualificação ao Doutorado (Doutorado em Engenharia Civil (Estruturas)) – Escola de Engenharia de São Carlos, Universidade de São Paulo, São Carlos, 2022.

VASCONCELOS, T. D. L.; HAACH, V. G. Exploring parameters of influence in ultrasound testing of reinforced concrete structures. *In*: CONGRESSO BRASILEIRO DO CONCRETO, 65., 2024, Maceió. **Anais** […]. São Paulo: IBRACON, 2024. Work 65CBC0363.

VIKTOROV, I. A. **Rayleigh and Lamb waves:** physical theory and applications. New York: Plenum Press, 1967.

VILLAIN, G. *et al*. Durability diagnosis of a concrete structure in a tidal zone by combining NDT methods: laboratory tests and case study. **Construction and Building Materials**, v. 37, p. 893–903, Dec. 2012.

VILLARES, D.; AYALA, H.; KUBRUSLY, A. C. Improved stress estimation with machine learning and ultrasonic guided waves. **Experimental Mechanics**, v. 62, n. 2, p. 237–251, Oct. 2021.

WANG, C. *et al*. Propagation properties of guided wave in the anchorage structure of rock bolts. **Journal of Applied Geophysics**, v. 69, n. 3-4, p. 131–139, Dec. 2009.

WIDEHAMMAR, S.; GRADIN, P. A.; LUNDBERG, B. Approximate determination of dispersion relations and displacement fields associated with elastic waves in bars: method based on matrix formulation of hamiltons principle. **Journal of Sound and Vibration**, v. 246, n. 5, p. 853-876, 2001.

WOJTCZAK, E.; RUCKA, M. Monitoring the curing process of epoxy adhesive using ultrasound and Lamb wave dispersion curves. **Mechanical Systems and Signal Processing**, v. 151, p. 1-13, 2021.

WOJTCZAK, E.; RUCKA, M. Damage imaging algorithm for non-destructive inspection of CFRP/steel adhesive joints based on ultrasonic guided wave propagation. **Composite Structures**, v. 297, p. 1-16, Oct. 2022.

WORDEN, K. Rayleigh and Lamb waves: basic principles. **Strain**, v. 37, n. 4, p. 167–172, Nov. 2001.

XIE, F., ZHUANG, C., JIANG, H., FAN, P., REN, Y. Damage assessment of real-size T-beam from deficient prestressed concrete bridge using ultrasonic coda waves. *In*: IEEE FAR EAST NDT NEW TECHNOLOGY & APPLICATION FORUM, 2016, Nanchang. **Proceedings** […]. Piscataway: IEEE, 2016. p. 22-25.

XU, B. *et al*. Multi-physical field guided wave simulation for circular concrete-filled steel tubes coupled with piezoelectric patches considering debonding defects. **International Journal of Solids and Structures**, v. 122, p. 25-32, 2017.

YAMAKAWA, J.; MURAKAMI, H. Longitudinal and flexural wave propagation in reinforced concrete columns. **International Journal of Solids and Structures**, v. 34, n. 33-34, p. 4357–4376, Nov. 1997.

YANG, Y. *et al*. Finite element prediction of acoustoelastic effect associated with Lamb wave propagation in pre-stressed plates. **Smart Materials and Structures**, v. 28, n. 9, p. 1-11, Jul. 2019.

YANG, Y.; POLAK, M. A.; CASCANTE, G. Nondestructive evaluation of the depth of surface-breaking cracks in concrete pipes. **Tunnelling and Underground Space Technology**, v. 25, n. 6, p. 736–744, Dec. 2010.

ZEMANEK JR, J. An experimental and theoretical investigation of elastic wave propagation in a cylinder. **The Journal of the Acoustical Society of America**, v. 51, n. 1B, p. 265-283, 1972.

ZHANG, L. *et al*. The study of non-detection zones in conventional long-distance ultrasonic guided wave inspection on square steel bars. **Applied Sciences**, v. 8, n. 1, p. 129, Jan. 2018.

ZHU, W.-F. *et al*. Time-domain topological energy imaging method of concrete cavity defect by lamb wave. **Shock and Vibration**, v. 2019, p. 1–13, Dec. 2019.

ZHU, Q. *et al*. A loading assisted diffuse wave inspection of delamination in a unidirectional composite. **Applied Acoustics**, v. 177, p. 107868-107868, Jun. 2021.

ZIMA, B. Guided wave propagation in detection of partial circumferential debonding in concrete structures. **Sensors**, v. 19, n. 9, p. 1-21, May 2019.

ZIMA, B.; KĘDRA, R. Reference-free determination of debonding length in reinforced concrete beams using guided wave propagation. **Construction and Building Materials**, v. 207, p. 291-303, 2019.

ZIMA, B.; KĘDRA, R. Baseline-free debonding detection in reinforced concrete structures by elastic wave propagation. **Measurement**, v. 172, p. 1-15, 2021.

ZIMA, B.; RUCKA, M. Non-destructive inspection of ground anchors using guided wave propagation. **International Journal of Rock Mechanics and Mining Sciences**, v. 94, p. 90-102, 2017a.

ZIMA, B.; RUCKA, M. Guided wave propagation for assessment of adhesive bonding between steel and concrete. **Procedia Engineering**, v. 199, p. 2300-2305, 2017b.

ZIMA, B.; RUCKA, M. Guided ultrasonic waves for detection of debonding in bars partially embedded in grout. **Construction and Building Materials**, v. 168, p. 124-142, 2018.

ZHONG, B.; ZHU, J.; MORCOUS, G. Measuring acoustoelastic coefficients for stress evaluation in concrete. **Construction and Building Materials**, v. 309, p. 1-8, Nov. 2021.

APPENDIX A - Wave velocities in prisms

			Compression	**Bending**
Diameter (mm)	**Prism**	**Strain gauge**	**Wave velocity (m/s)**	
8	P1	1	4338	4476
		2	4406	4406
		3	4700	4661
		4	4780	4548
	P2	1	4548	4623
		2	4661	4548
		3	4512	4476
		4	4623	4476
	P3	1	4548	4548
		2	4338	4585
		3	4623	4585
		4	4548	4476
10	P4	1	4623	4585
		2	4406	4512
		3	4273	4548
		4	4273	4512
	P5	1	4476	4862
		2	4406	4476
		3	4273	4273
		4	4548	4661
	P6	1	4780	4780
		2	4548	4548
		3	4476	4305
		4	4548	4548
12.5	P7	1	4780	4623
		2	3890	4476
		3	4147	4372
		4	4087	4780
	P8	1	4585	4441

		2	4548	4273
		3	4209	4441
		4	4087	4406
	P9	1	4029	---
		2	4058	---
		3	4147	---
		4	3917	---
			Compression	**Bending**
Diameter (mm)	**Prism**	**Strain gauge**	**Wave velocity (m/s)**	
16	P10	1	3241	---
		2	3972	---
		3	3615	---
		4	---	---
	P11	1	4548	---
		2	4406	---
		3	---	---
		4	4029	---
	P12	1	---	---
		2	3760	---
		3	---	---
		4	4209	---

APPENDIX B - Sieve test results

Fine sand			
1st test			
Sieve opening diameter (µm)	**Retained (g)**	**Retained (%)**	**Accumulated (%)**
4750	0	0	0
2360	0.26	0.05	0.05
1180	0.68	0.13	0.19
600	1.90	0.38	0.56
300	58.45	11.56	12.12
150	330.30	65.34	77.46
Base	113.95	22.54	100
Total	505.54	100	
2nd test			
4750	0.00	0.00	0.00
2360	0.05	0.01	0.01
1180	0.78	0.16	0.17
600	1.92	0.38	0.55
300	61.63	12.28	12.83
150	328.17	65.41	78.25
Base	109.14	21.75	100
Total	501.69	100	
Average values			
4750	0.00	0.00	0.00
2360	0.16	0.03	0.03
1180	0.73	0.14	0.18
600	1.91	0.38	0.55
300	60.04	11.92	12.48
150	329.24	65.37	77.85
Base	111.55	22.15	100
Total	503.62	100	

Medium-size sand			
1st test			
Sieve opening diameter (µm)	**Retained (g)**	**Retained (%)**	**Accumulated (%)**
4750	0.00	0.00	0.00
2360	0.73	0.15	0.15
1180	1.26	0.25	0.40
600	22.62	4.52	4.92
300	266.36	53.28	58.21
150	177.80	35.57	93.77
Base	31.12	6.23	100
Total	499.89	100	
2nd test			
4750	0.00	0.00	0.00
2360	0.50	0.10	0.10
1180	1.22	0.24	0.34
600	24.18	4.83	5.17
300	253.42	50.59	55.76
150	189.08	37.75	93.50
Base	32.54	6.50	100
Total	500.94	100	
Average values			
4750	0.00	0.00	0.00
2360	0.62	0.12	0.12
1180	1.24	0.25	0.37
600	23.40	4.68	5.05
300	259.89	51.94	56.98
150	183.44	36.66	93.64
Base	31.83	6.36	100
Total	500.42	100	

Coarse aggregate			
1st test			
Sieve opening diameter (mm)	**Retained (g)**	**Retained (%)**	**Accumulated (%)**
19.00	0	0	0
12.50	79.08	3.93	3.93
9.50	1,174.42	58.40	62.33
6.30	746.50	37.12	99.45
4.75	10.96	0.55	100
Base	0	0	0
Total	2,010.96	100	
2nd test			
19.00	0	0	0
12.50	101.46	5.05	5.05
9.50	1,170.61	58.30	63.35
6.30	721.50	35.93	99.29
4.75	14.28	0.71	100
Base	0	0	0
Total	2,007.85	100	
Average values			
19.00	0	0	0
12.50	90.27	4.49	4.49
9.50	1,172.52	58.35	62.84
6.30	734.00	36.53	99.37
4.75	12.62	0.63	100
Base	0	0	0
Total	2,009.41	100	

APPENDIX C – Papers by research

PERIÓDICOS CAPES		**FIELDS OF FILLING**		
Research	**Date of search**	**"*Qualquer campo contém*"**	**"*Título contém*"**	**Papers**
1	9/18/23	Lamb wave; Reinforced concrete		Chen *et al.* (2021)
2	9/18/23	Lamb wave; dispersion curve; steel bar		Zima (2019) and Zhu *et al.* (2019)
3	10/3/23	reinforced concrete	acoustoelastic	Lillamand *et al.* (2010)
4	10/6/23	Lamb OR Rayleigh OR Guided; acoustoelastic		Dodson and Inman (2014), Gandhi, Michaels and Lee (2012), Kubrusly, Braga and Weid (2016), Pei and Bond (2016b), Pei and Bond (2017a), Mohabuth and Kotousov (2019) and Shi *et al.* (2023)
5	10/6/23	Lamb; reinforced concrete; acoustoelastic		0
6	10/16/23	Lamb; dispersion curve; cylinder		Zemanek (1972), Kley *et al.* (1999), Gunawan *and* Hirose (2005), Gravenkamp, Birk *and* Song (2014), Laurent *et al.* (2015), Hussain, Ahmad and Ozair (2017), Gadzhibekov *and* Ilyashenko (2021)

7	10/26/23	pochhammer; dispersion; cylinder		Yamakawa and Murakami (1997), Mazúch (2003), Ahmad (2004), Puckett and Peterson (2005), Treyssède (2007) and Brizard and Jacquelin (2022)
8	12/14/23	disperse; software; concrete; guided wave		0
WEB OF SCIENCE		**“All fields”**	**“Title”**	**Papers**
1	10/5/23	lamb wave steel bar and ultrasonic or ultrasonic		Jung *et al.* (2000), Na, Kundu and Ehsani (2002), Mustapha *et al.* (2014), Li *et al.* (2017), Garcia (2017), Zhang *et al.* (2018) and Majhi *et al.* (2021)
2	10/6/23		Lamb AND acoustoelastic	Delsanto *et al.* (1999), Gandhi *et al.* (2011), Pei and Bond (2015), Pei and Bond (2016a), Pei and Bond (2017b) and Li and Shi (2022)
3	10/6/23	Reinfored concrete AND Lamb	acoustoelastic	0
4	10/17/23	Reinfored concrete AND Lamb	acoustoelastic	0
5	11/6/23	Pochhamer AND dispersion curve	rod	Saravanan (2020)
6	12/14/23	disperse AND concrete AND guided wave AND software		0
SCIENCE DIRECT		**“Find articles with these terms”**	**“Title, abstract or author-specified keywords”**	**Papers**

1	10/5/22	lamb and wave and steel and bar and ultrasonic	reinforced and concrete	Kundu *et al.* (1999), Villain *et al.* (2012), Lu *et al.* (2013), Scott (2013), Ohtsu (2016), Rajeshwara, Banerjee and Lu (2017), Rodríguez-Roblero *et al.* (2019), Ke *et al.* (2019), Zima and Kędra (2019), Li *et al.* (2021) and Mahbaz, Cascante and Dusseault (2021)
2	10/5/22	lamb and wave and steel and bar and ultrasonic and concrete	steel guided wave	Guo, Zhang and Zhang (2012), Mazzotti *et al.* (2013), Zima and Rucka (2017b), Xu *et al.* (2017), Zima and Rucka (2018), Wojtczak and Rucka (2021) and Wojtczak and Rucka (2022)
3	10/5/22	reinforced concrete	acoustoelastic OR acoustoelasticity	Zhu *et al.* (2021)
4	10/6/23	reinforced concrete AND lamb AND acoustoelastic		Gorgin, Luo and Wu (2020)
5	11/6/23	pochhammer AND dispersion curve AND rod		Brizard, Jacquelin and Ronel (2019)
6	11/13/23	pochhammer AND dispersion curve AND cylinder		Kari (2002), Elmaimouni *et al.* (2005), Honarvar, Enjilela and Sinclair (2009), Shatalov, Every and Yenwong-Fai (2009), Wang *et al.* (2009), Every, Shatalov and Yenwong-Fai (2010), Seco *et al.* (2011), Liu, Tang and Xu
		pochhammer AND dispersion curve AND cylinder	pochhammer AND dispersion curve AND cylinder	
		pochhammer AND dispersion curve AND cylinder	pochhammer AND cylinder AND Guided wave	

		pochhammer AND cylinder AND dispersion curve AND guided wave		(2012), Höhne, Prager and Gravenkamp (2015), Farhidzadeh and Salamone (2015), Zima and Rucka (2017a), Barr, Rigby and Clayton (2020), Liao and Qiao (2023) and Cui, Liu and Maghoul (2023)
7	12/14/23	disperse AND software AND reinforced concrete AND guided wave AND dispersion curve		Sharma and Mukherjee (2014), Sun and Zhu (2020), Aseem and Ng (2021), Sharma *et al.* (2021) and Aseem and Ng (2023)
SCOPUS		**"All fields"**	**"Article title, Abstract, Keywords"**	**Papers**
1	10/3/23	reinforced concrete	acoustoelastic	Chen and Wissawapaisal (2002), Rizzo and Lanza (2002), Scalea, Rizzo and Seible (2003), Hughes *et al.* (2018), Yang *et al.* (2019), Gondim and Haach (2021), Villares, Ayala and Kubrusly (2021) and Ng *et al.* (2022)
2	10/6/23		Lamb AND Acoustoelastic	Hong-Ye *et al.* (2020)
3	10/6/23		Lamb and reinforced concrete and acoustoelastic	0
			Lamb and reinforced concrete and acoustoelasticity	
4	11/16/23		Lamb and reinforced	0

			concrete and acoustoelastic	
			Lamb and reinforced concrete and acoustoelasticity	

APPENDIX D – Formulas of P_i

$$P_6 = (A_{1323}^2 - A_{1313}A_{2323})A_{3333} \tag{0.1}$$

$$\begin{aligned} P_4 = {} & A_{1233}^2 A_{1313} + A_{1313}A_{1323}^2 - 2A_{1133}A_{1323}A_{1332} \\ & - 2A_{1323}A_{1331}A_{1332} + A_{1313}A_{1332}^2 \\ & + 2A_{1233}(-A_{1323}(A_{1133} + A_{1331}) + A_{1313}A_{1332}) \\ & + A_{1133}^2 A_{2323} - A_{1313}^2 A_{2323} + 2A_{1133}A_{1331}A_{2323} \\ & + A_{1331}^2 A_{2323} \\ & - (A_{1212}A_{1313} - 2A_{1112}A_{1323} + A_{1111}A_{2323})A_{3333} \\ & + c^2\rho(-A_{1323}^2 + A_{1313}A_{2323} + (A_{1313} + A_{2323})A_{3333}) \end{aligned} \tag{0.2}$$

$$\begin{aligned} P_2 = {} & A_{1133}^2 A_{1212} + A_{1111}A_{1233}^2 - A_{1212}A_{1313}^2 + 2A_{1112}A_{1313}A_{1323} \\ & - 2A_{1112}A_{1233}A_{1331} + A_{1212}A_{1331}^2 + 2A_{1111}A_{1233}A_{1332} \\ & - 2A_{1112}A_{1331}A_{1332} + A_{1111}A_{1332}^2 \\ & - 2A_{1133}\big(-A_{1212}A_{1331} + A_{1112}(A_{1233} + A_{1332})\big) \\ & - A_{1111}A_{1313}A_{2323} + (A_{1112}^2 - A_{1111}A_{1212})A_{3333} \\ & - c^4\rho^2(A_{1313} + A_{2323} + A_{3333}) \\ & + c^2\rho\big(-2A_{1112}A_{1323} - (A_{1133} + A_{1331})^2 \\ & - (A_{1233} + A_{1332})^2 + A_{1313}(A_{1212} + A_{1313} + A_{2323}) \\ & + A_{1212}A_{3333} + A_{1111}(A_{2323} + A_{3333})\big) \end{aligned} \tag{0.3}$$

$$P_0 = \big(-A_{1112}^2 + (c^2\rho - A_{1111})(c^2\rho - A_{1212})\big)(c^2\rho - A_{1313}) \tag{0.4}$$


PPG
SET


EESC • USP